Exciton confinement in strain-engineered InAs quantum dots in metamorphic $In_xGa_{1-x}As$

Lancaster University

Thesis submitted in accordance with the requirements of
the Lancaster University for the degree of
Doctor in Philosophy (PhD)

by

Shaukat Ali Khattak

December 2015

UNIVERSITY OF LANCASTER

ABSTRACT

FACULTY OF SCIENCE

Department of Physics

Exciton confinement in strain-engineered InAs quantum dots

in metamorphic $In_xGa_{1-x}As$

In this work, magneto-photoluminescence at low temperature, 4.2 K, is used to probe the exciton confinement in strain-engineered $InAs/In_xGa_{1-x}As/GaAs$ metamorphic quantum dots (QDs), emitting at telecom wavelengths (1.3 μm - 1.6 μm). The emission wavelength can be tuned by changing two independent parameters, i.e., indium content, x, in $In_xGa_{1-x}As$ upper and lower confining layers and thickness of lower confining layer (LCL), d. Varying x changes the band offset and QD-CL mismatch (strain inside the QD), while varying d changes only QD-CL mismatch. We investigate the dependence of confinement on the QD-CL mismatch and band offset. Zero-magnetic-field spectra showed that wavelength (PL energy) increases (decreases) with increasing x, for a constant d, and with increasing d, for a constant x, which was attributed to be due to relaxation of strain inside the QD that is, in turn, a function of x and d. No correlation between wavelength and intensity was observed. Magneto-photoluminescence results revealed that for a subset of samples, the exciton effective mass increases linearly, more or less, with increasing QD-CL mismatch (QD strain), while its Bohr radius has no correlation with mismatch. The diamagnetic shift coefficient increases 12-fold with decreasing mismatch from $\sim$ 7.5 % to 4.5 %, which is attributed to low effective mass, which in turn, is due to low QD strain. For high mismatach ($>$ 5.8 %), the Bohr radius is not determined, implying that it is less than 10 nm, smaller than the dot radius. For indium composition $x = 0.28$ and 0.31, and for $d > 1000 \mathring{A}$, the wave-function spills over out of the dot. For $x = 0.35$, the Bohr radii are, counter intuitively, found to be smaller than for samples with larger band offset ($x = 0.31$). Initially, it was explained as a spilling of the wave-function over

vertically resulting in strong lateral confinement of exciton, but this explanation is not supported by our model calculations. Another explanation is, therefore, presented by carrying out temperature dependence and magnetic field dependence, at various temperatures, of PL energy: there are different dots, at $x = 0.35$, with different size where thermal escape of carriers from smaller dots to bigger ones occurs with increasing temperature, and the PL energy, in magnetic field, is contributed more by smaller dots than the bigger ones.

Acknowledgements

Conferences

- "Physics of exciton wave function in strain-engineered metamorphic InAs/In$_x$Ga$_{1-x}$As/GaAs quantum dots for telecommunications wavelengths (1.3 - 1.6 μm)"

  S. A. Khattak, M. Hayne, L. Seravalli, G. Trevisi and P. Frigeri

  8th International Conference on Quantum Dots (QD 2014) , Pisa, Italy (May 11-16, 2014)

- "Exciton confinement in strain-engineered metamorphic InAs/In$_x$Ga$_{1-x}$As/GaAs quantum dots for telecommunications wavelengths (1.3 - 1.6 μm)"

  Shaukat Ali Khattak, Manus Hayne, Luca Seravalli, Giovanna Trevisi and Paola Frigeri

  QD Day, Sheffield, UK (2014)

- "Why is a wave function like a balloon?"

  Shaukat Ali Khattak

  Christmas conference, Lancaster University, UK (Dec 2013)

- "Confinement of Excitons in Strain-engineered InAs/In$_x$Ga$_{1-x}$As/GaAs Metamorphic Quantum Dots"

  Shaukat A. Khattak, Manus Hayne, Luca Seravalli, GiovannaTrevisi and Paola Frigeri

  UK Semiconductors, Sheffield (July 03 04, 2013)

- "Confinement of Excitons in Strain-engineered InAs/In$_x$Ga$_{1-x}$As/GaAs Metamorphic Quantum Dots"

  Shaukat Ali Khattak, Manus Hayne, Luca Seravalli, Giovanna Trevisi and Paola Frigeri

  NOWNANO Summer Conference , Cheshire, UK (June 17-20, 2013)

- "Exciton confinement in strain-engineered metamorphic InAs/In$_x$Ga$_{1-x}$As/GaAs quantum dots for telecommunications wavelengths

(1.3 - 1.6 μm)"

Shaukat Ali Khattak, Manus Hayne, Luca Seravalli, Giovanna Trevisi and Paola Frigeri

Presentation at Rutherford Appleton Laboratory (RAL), Didcot, UK (18/06/2013)

- "Exciton Confinement in Strain-engineered InAs/In$_x$Ga$_{1-x}$As/GaAs Metamorphic Quantum Dots for Telecom Wavelength Emission"
  Shaukat Ali Khattak, Manus Hayne, Luca Seravalli, Giovanna Trevisi and Paola Frigeri
  QD Day Meeting, Nottingham, UK (May, 2013)

- "Properties of Excitons in Strain-engineered InAs/In$_x$Ga$_{1-x}$As/GaAs Metamorphic Quantum Dots"
  S. A. Khattak, M. Hayne, L. Seravalli, G.Trevisi and P. Frigeri
  European School On Nanosciences and Nanotechnologies, Grenoble, France (August, 2012)

- "Properties of Excitons in Strain-engineered InAs/In$_x$Ga$_{1-x}$As/GaAs Metamorphic Quantum Dots for Long Wavelength (1.3 to 1.55 μm) Emission"
  Shaukat Ali Khattak, Manus Hayne,, Luca Seravalli,, Giovanna Trevisi, and Paola Frigeri
  UK Semiconductors, Sheffield (July, 2012)

Contents

List of Figures

List of Tables

Chapter 1

Introduction

1.1 Motivation

Discreteness of energy levels and the consequent three dimensional (3D) carrier confinement, has made self-assembled quantum dots (QDs) the subject of intense investigation over the past decades, with applications in a variety of technologies [1, 2]. They have promising performance in many innovative photonic applications such as infrared photodetectors [3], low-threshold lasers [2, 4], optical amplifiers [5], memory devices [6] and single photon devices [7].

QDs have the edge over conventional quantum well heterostructures that offer only one dimensional (1D) confinement and exhibit strain limits. This superiority includes temperature independence of threshold current densities [8], broadened gain spectrum of laser [9], reduced threshold current [10] and reduced chirp [11].

They are spontaneously formed using the Stranski-Krastanow (SK) technique during epitaxial growth processes, like molecular beam epitaxy (MBE) or metalorganic vapour phase epitaxy. The SK technique has many advantages that include large confinement energies and energy level separations, high radiative efficiency, high areal

densities and good uniformity, and their inclusion in a semiconductor matrix, permitting the efficient injection and extraction of carriers [12].

Charge carriers, electrons and holes (which, when bound together forming excitons), are localized by potential barriers through quantum confinement in the dot structure, restricting the three translational degrees of freedom to zero [1]. When the dots are small enough such that their energy level spacing exceeds kT (where k is Boltzmann's constant and T is temperature), which occurs when the dot size approaches the Bohr radius of the bulk exciton or the electron de-Broglie wavelength, quantum confinement becomes signifcant [13]. This results in discrete atomic-like energy levels where the carriers in the quantum dot can exist only in certain quantized energy states, just as in atoms, whereas in bulk semiconductor system, the density of states is continuous. They are, therefore, also called artificial atoms, at times [14]. Quantum confinement tailors the electronic properties of the electron and hole in a confined space [15]. The confining potential and electrostatic interactions between the carriers are responsible for the energy structure of carrier complexes confined to QDs.

Due to scientific curiosity and optoelectronic applications, quantum confinement of carriers is the subject of intense investigation. Experimentally, a range of systems have been studied to probe the confinement, like stacked self-assembled InP QDs [16], self-assembled GaSb/GaAs QDs [17, 18] and GaAs/AlGaAs QDs [19] etc. Theoretically, the effective-mass approximation has been used to obtain basic information about the effects of confinement, where both electron and hole have been described with isotropic effective masses [20].
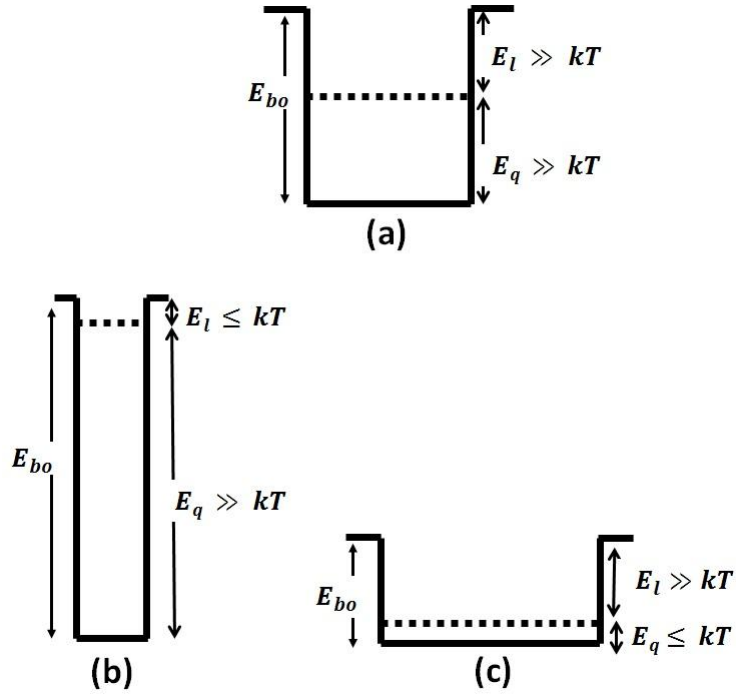
FIGURE 1.1: Schematic diagram showing (a) strong and (b), (c) weak confinement in a quantum dot. For strong confinement both localization energy, E_l, and quantization energy, E_q, are higher than kT, whereas for weak confinement either E_l or E_q are similar to or smaller than kT. E_{bo} represents band offset, the energy difference between the conduction bands of QD and surrounding material.

In the literature, the terms 'strong confinement' and 'weak confinement' are often used, but it is not always clear what these actually mean. For example, a very small QD will not provide strong confinement if there is substantial leakage of the wave-function into the barrier. Here we define strong confinement to be when both the localization energy (the energy required for carriers to escape from the dot), E_l, and quantization energy, E_q, of carriers are much larger than kT (Fig. 1.1(a)), and weak confinement to be where either E_l or E_q are similar to or smaller than kT, as shown in Fig. 1.1(b) and Fig. 1.1(c) respectively. Strong and weak confinement may be defined, alternatively, as: the strong confinement to be when the exciton Bohr radius is of the order of the dot radius (Fig. 1.1(a)), while weak confinement will be when either the exciton radius is so much bigger than of the dot that its wave-function

spills out of the dot (Fig. 1.1(b)) or it is so much smaller than the dot's one that its confinement is not affected by the dot (Fig. 1.1(c).

In order to obtain long wavelength emission, important for telecommunications (1260 to 1675 nm), InAs nanostructures have been intensively studied over the last decade [21]. To extend the wavelength emission up to 1.5 -1.6 μm, the $In_xGa_{1-x}As$ metamorphic structure (Fig. 1.2) has been proved promising, where InAs QDs are embedded in an $In_xGa_{1-x}As$ upper confining layer (UCL) and an $In_xGa_{1-x}As$ lower confining layer (LCL) grown on GaAs substrates [22].
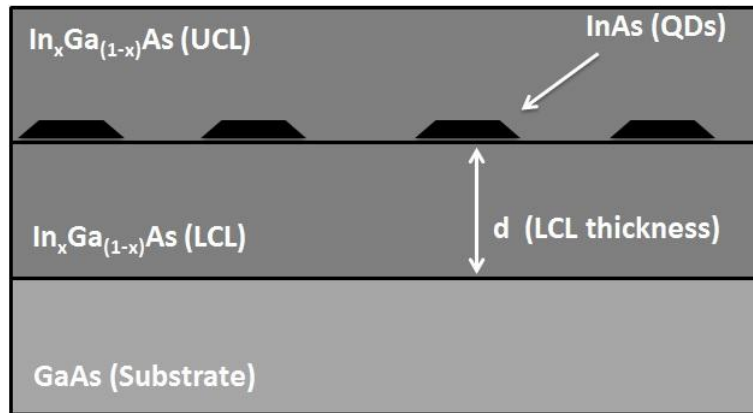
FIGURE 1.2: Schematic diagram of the samples, where InAs QDs are embedded in $In_xGa_{1-x}As$ confining layers (CLs).

In such studies, and the work presented in this thesis, the UCL has a constant thickness of 20 nm while the thickness of the LCL, d, and indium composition, x, in both confining layers (CLs) are variables used to tune the emission. Any change in indium composition in the CLs, will change the band offset and the QD-CLs mismatch (strain inside the QD), f, while variation of d changes only f. It is clear that getting to 1.5 μm or longer by increasing the In composition in the metamoprhic (explained in chapter-4) CLs , and hence reducing band offset, reduces the confinement. Therefore, it is important to investigate the exciton confinement in such structures.

In this work we present magneto-photoluminescence (the behaviour of photoluminescence in magnetic fields, detailed in sections 2.3 and 3.2.5) studies of a series

of InAs QD samples in metamorphic $InAs/In_xGa_{1-x}As/GaAs$ confining layers as a model system for probing exciton (a bound state of electron and a hole) confinement in self-assembled quantum dots. We use magneto-PL to extract information about the effect of changing x and d on the exciton diamagnetic shift coefficient (defined in chapter-2), Γ, reduced mass, μ, and Bohr radius, a_B.

1.2 Synopsis of thesis

In Chapter 2, a summary of the background physics is discussed: it includes the basic concepts of energy bands and band gaps, semiconductors, semiconductor nanostructures, density of states, epitaxy techniques and different growth modes, photoluminescence of quantum dots, excitons in magnetic field, Fock-Darwin and excitonic models.

Chapter 3 is a literature review, where the developments in the field are described. An overview of InAs QDs, studied in different structures, like InAs/GaAs, InAs/InGaAs/GaAs, InAs/InP, InAs/Si for telecom wavelengths, is presented. A short description of systems other than InAs, like InP quantum-wires (QWs), GaSb QDs and quantum rings (QRs), dilute nitride quantum wells (QWs), is given. Various ways to study the electronic structure of quantum dots are discussed such as study of morphological parameters and single dot spectroscopy, deep-level transient spectroscopy (DLTS), wave-function imaging (direct cross-sectional scanning tunneling microscopy (X-STM) and small K-space while using magnetic field resonant tunneling) and magneto-PL.

Chapter 4 is about growth mechanism of nanostructures: epitaxy, different techniques of the growth, i.e., molecular beam epitaxy (MBE) and atomic layer molecular beam epitaxy (ALMBE); different growth modes: Frank-Van der Merwe (FM), Volmer-Weber (VW) and Stranski-Krastanov (SK) are discussed.

In Chapter 5, the experimental procedure and analysis is explained. This includes growth of samples, laboratory set-up, cryostat, optics and methodology of data analysis.

Chapter 6 contains the results obtained in zero-magnetic field. This includes the spectra showing the dependence of wavelength (and PL energy) on indium content in confining layers, x, and thickness of lower confining layer, d, and the relation of PL intensity and line-width with x and d.

Chapter 7 is about the results obtained by magneto-photoluminescence and consist of a detailed investigation of exciton confinement. The discussion is grouped in three sections by the properties of exciton: diamagnetic shift coefficient, Bohr radius and reduced mass. Bohr radius and reduced mass are discussed together briefly for a subset of samples in one section. In the next section, diamagnetic shift coefficient is explained extensively assisted by drawing a so-called bubble plot. Afterwards, the Bohr radius is discussed further separately using a bubble plot. Modelling results are presented which turn out to be contradictory with experimental ones. The contradiction is resolved by looking into the temperature dependence and magnetic field dependence, at various temperatures, of the PL energy.

Finally Chapter 8 concludes the thesis with a summary of the major achievements of this work, and possible suggestions for further work are presented.

Chapter 2

Background Theory

2.1 Energy bands, band gaps and semiconductors

The discrete energy levels of electrons in isolated atoms appear as energy bands in solids due to the overlapping of electrons wave-functions in the neighbouring atoms, and due to the uncertainty in location of an electron at a specified atom. The overlapping starts when isolated atoms are brought together, thereafter forces of attraction and repulsion balance each other at the proper interatomic spacing for the crystal. In semiconductor, at zero temperature, the highest fully occupied band is the valence band, whilst the next highest energy band, which is unoccupied, is the conduction band. The difference in energy between the lowest point of the conduction band (conduction band edge) and the highest point of the valence band (valence band edge) is called the band gap (Fig. 2.1).

Semiconductors are usually described by their electrical resistivity at room temperature, ranging from 10^{-2} to 10^{9} ohm-cm [23]. The resistivity decreases with increasing temperature when thermal excitation of electrons from valence to conduction band occurs. Electrons can also be optically excited from the valence band to the conduction band, then can contribute to the current transport process. A pure and perfect

semiconductor crystal will be insulating at absolute zero, if an insulator is arbitrarily defined as having resistivity above 10^{14} ohm-cm.
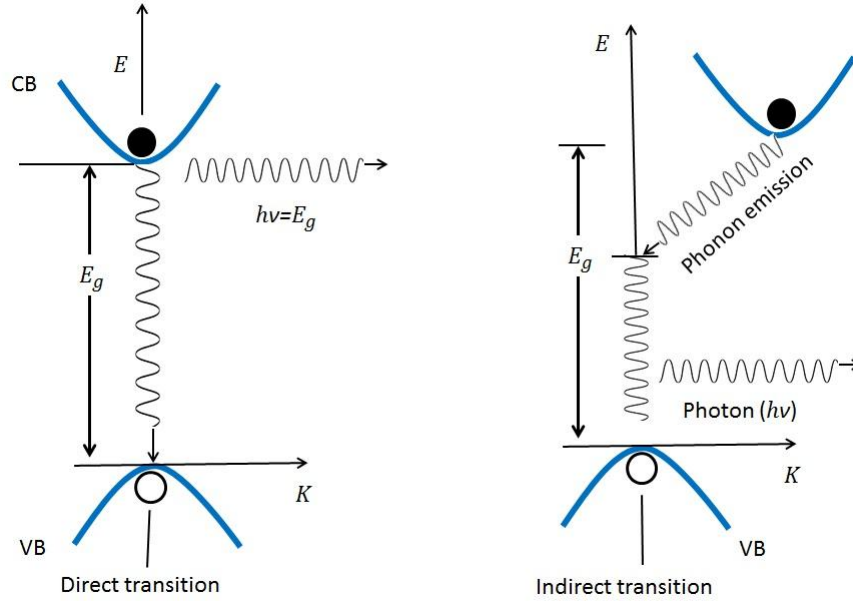
FIGURE 2.1: Direct and indirect transition of electrons from the conduction band to the valence band: (a) direct - with accompanying photon emission, (b) indirect via defect level. The band gap is E_g.

Semiconductors can be categorized into two types, in terms of their band structures: direct band-gap semiconductors and indirect band-gap semiconductors. In direct band gap semiconductors, the minimum of the conduction band and the maximum of the valence band occur at the same value of wave-vector k (momentum) and an electron makes the smallest energy transition from the conduction band to the valence band without any change in k. On the other hand, in indirect band-gap semiconductors, the minimum of the conduction band and the maximum of the valence band occur for different values of k, thus, the smallest energy transition for an electron requires a change in momentum. The probability of recombination (electron falling from the conduction band to an empty state in the valence band), is thus much higher for direct band gap semiconductors than for indirect band gap semiconductors. During this transition in the direct band-gap semiconductors, energy equal to

E_g is released in the form of light, which can be used for optoelectronic applications, e.g., LEDs and lasers. Relaxation of the electron from the conduction to the valence band in indirect band gap semiconductors occurs through some defect states within the band gap or emission of a phonon, the excess energy, i.e. that not taken away by the photon, is released in the form of heat given to the lattice (Fig. 2.1).

2.2 Semiconductor nanostructures

2.2.1 Density of states

In the bulk, three dimensional (3D), the density of states, $\rho\,(E)$, of free electrons is continuous and depends on the square-root of energy, E [24],

$$\rho_{3D}(E) = dN/dE = \frac{V}{2\pi^2}(\frac{2m_e^*}{\hbar^2})^{3/2}\sqrt{E} \ , \qquad (2.1)$$

where N is the number of states, V is the sample volume, m_e^* is the effective mass of electron and E_g is the semiconductor energy gap. The energy of an electron in a bulk crystal with parabolic bands is given by the isotropic relationship,

$$E_{3D} = \frac{\hbar^2}{2m_e^*}(k_x^2 + k_y^2 + k_z^2) \ , \qquad (2.2)$$

where $\hbar$ is the reduced Planck constant and k_x, k_y and k_z are the wave numbers in the cartesian coordinate system. By restricting the charge carrier's motion in one dimension to length l_z in the z direction, having thickness comparable to the de-Broglie wavelength of the carrier (a few 10's of nanometres or less), a two dimensional (2D) system is achieved. The free motion of the carrier is possible only along two dimensions, for which the density of states is given by

$$\rho_{2D}(E) = \frac{m_e^*}{\pi\hbar^2} \ . \qquad (2.3)$$

It is worth noting that the density of states for 2D is independent of the energy. However, ρ is a function of the number of levels and is thus a sum of the contributions from the discrete levels appearing as a result of the quantization

$$\rho_{2D}(E) = \sum_n \frac{m_e^*}{\pi \hbar^2} H(E - E_{cn}) \ , \tag{2.4}$$

where $H(E - E_{cn})$ is the Heaviside step function and E_{cn} denotes the conduction band minima of the discrete levels. The energy of the carrier in such a quantum well (QW) is now given by

$$E_{2D} = \frac{\hbar^2}{2m_e^*}(k_x^2 + k_y^2) + E_{n,z} \ , \tag{2.5}$$

where $E_{n,z}$ is the energy of the quantum confined state in the z direction, n given by ,

$$E_{n,z} = \frac{\hbar^2}{2m_e^*}\left(\frac{n\pi}{l_z}\right)^2 \ . \tag{2.6}$$

Moving towards restricting the motion in another dimension, say to l_y in the y direction, a one dimensional system is achieved i.e. free motion of the carrier is along only one direction (x). The density of states in such a quantum wire is given by

$$\rho_{1D}(E) = \frac{1}{\pi} \sum_m \sqrt{\frac{2m_e^*}{\hbar^2}} \frac{1}{\sqrt{E - E_m}} \ , \tag{2.7}$$

and energy of carrier is given by,

$$E_{1D} = \frac{\hbar^2 k_x^2}{2m_e^*} + E_{m,y} + E_{n,z} \ , \tag{2.8}$$

where $E_{m,y}$ is the energy of confined states m for the y-direction. Finally, the motion of the carrier can be limited in all three directions resulting in the formation of a quantum dot (QD) with for which density of states is given by

$$\rho_{0D}(E) = 2 \sum_{n,m,l} \delta(E - E_{n,m,l}) \tag{2.9}$$

and energy spectrum is given by

$$E_{0D} = E_{l,x} + E_{m,y} + E_{n,z} \ , \tag{2.10}$$

where $E_{l,x}$ is the energy of the l state for the x-direction.
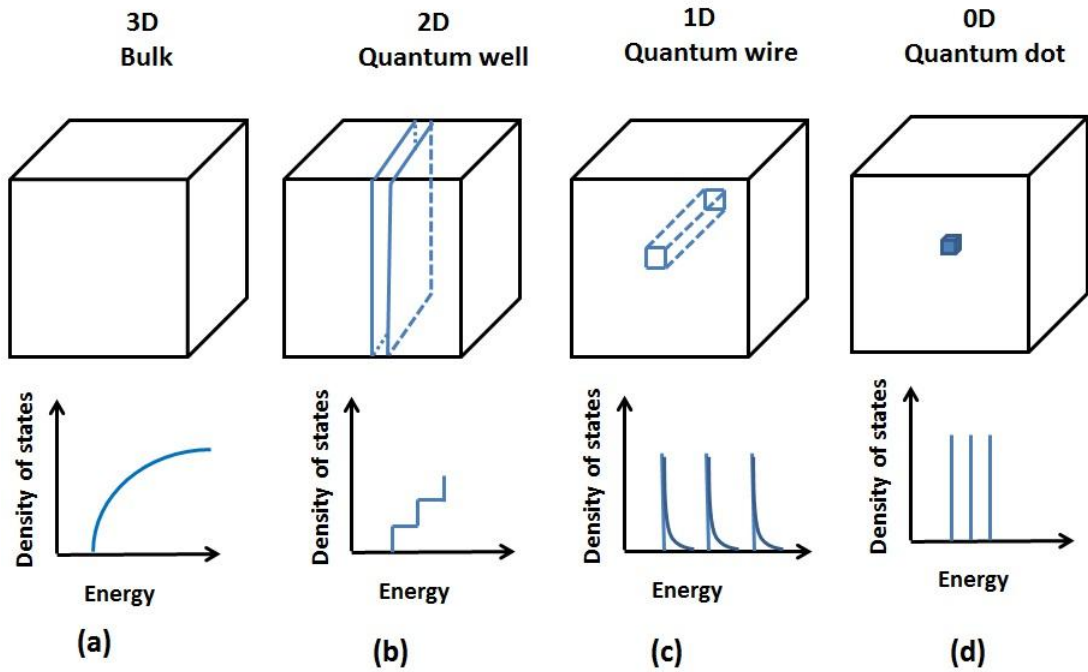
FIGURE 2.2: Semiconductor structure with different dimensionalities (upper). Semiconductor structure with corresponding electronic density of states (lower). It can be noticed that only in the 3D case, the density of states is continuous. This is a result of quantization due to confinement in one or more directions.

Thus, by discretisation of the energy, the density of states develops from a square root dependence on energy for 3D semiconductors (bulk), to distinct plateaus (QW), crest behaviour with a high energy tail (quantum wire) and ultimately an assemblage of delta functions, where the energies are functions of the physical extent of the quantum dot (Fig. 2.2). Due to these discrete energy levels, quantum dots are often known as artificial atoms [25]. They are zero-dimensional semiconductor nano-crystals, a few nanometres in size. It may be perceived that "zero-dimensional" doesn't imply that

the dots are dimensionless at all, but rather confined in all three dimensions. Quantum dots are very useful because their properties can be synthetically manipulated and are promising candidates for many devices, for instance lasers.

2.2.2 Effective mass model

Effective mass model approach was first introduced by Efros [26] and modified by Brus [15], and is most widely used to predict the confinement of carriers based on the 'Particle in Box Model'. In such a model a particle is assumed to be in a potential well with an infinite potential barrier at the particle boundary. However, in the effective mass model, the potential barrier has been approximated to be finite. In addition, the Coulomb interaction between electron and hole has been neglected. The relationship between the energy (E) and wave vector (k) for the particle moving freely to any position in the box is given by,

$$E = \frac{\hbar^2 k^2}{2m^*} \quad, \tag{2.11}$$

where $\hbar$ is the reduced Planck constant and m^* is the effective mass. In the model, this relationship is considered for an electron or a hole in a semiconductor, therefore the energy band is parabolic near the band-edge. The shift of the lowest energy state with respect to the band-gap energy (ΔE_q) due to confinement of the exciton in a quantum dot with a diameter, R, can be expressed as follows,

$$\Delta E_q = \frac{\hbar^2 \pi^2}{2R^2}\left(\frac{1}{m_e^*} + \frac{1}{m_h^*}\right) - \frac{1.78e^2}{\varepsilon R} - 0.248 E_{RY}^* \quad, \tag{2.12}$$

where m_e^* and m_h^* are the effective masses of an electron and a hole respectively, $\left(\frac{1}{m_e^*} + \frac{1}{m_h^*}\right) = \frac{1}{\mu}$, where μ is the reduced mass of an electron-hole pair, e is the charge of electron, ε is dielectric constant and E_{RY}^* is Rydberg energy. The first term of the equation shows a relation between the radius of the quantum dot (R) and 'particle-in-a-box' quantum localization energy or confinement energy, whereas the second term

represents the Coulombic interaction energy with a R^{-1} dependence. The Rydberg energy term is size independent and is usually negligible, except for semiconductors with small dielectric constant [27]. Based on equation (2.12), the first excitonic transition i.e., energy difference between lowest confined electron and hole states, increases as the quantum dot diameter, R, decreases (quantum localization term shifts to higher energy as it is $\propto$ to $\frac{1}{R^2}$) while the Coulombic term, (being $\propto$ to $\frac{1}{R}$) with minus sign, shifts the electronic states to lower value. However, the model breaks down in the small quantum dot regime [27, 28] because the $E - k$ relationship can no longer be approximated as parabolic.

2.2.3 Photoluminescence of quantum dots

Photoluminescence is one of the most useful tools for probing optical transitions in semiconductors. It is mainly a mechanism of excitation to a high energy state by an incident photon of energy hf, followed by de-excitation to a lower energy state that radiates a photon of energy hf' (Fig. 2.3). When light of energy equal to or greater than band gap energy of the material is incident, an electron is excited from the valence band to the conduction band, leaving a positively charged vacancy in the valence band, which is termed as a hole. The electron and hole then relax to their corresponding equilibrium locations through non-radiative transitions e.g., via phonon emission, which conserve energy and momentum. After this, the electron and hole reside at the minimum of the conduction band and at the maximum of the valence band, respectively.

Because of their Coulomb interaction, an electrically neutral and a quasi-bound particle, the exciton, having energy slightly less than that of unbound electron and hole, can also come into being, which can move freely and independently through the material. The exciton energy levels are analogous to those of a hydrogen atom and are

formed below the bottom of the conduction band, but with a dispersion that is different from that of the conduction band. The exciton energy levels can be written as the sum of the electron and hole energies, E_e and E_h respectively, minus the binding energy [29]:

$$E = E_e + E_h - \frac{\mu R_y}{\epsilon^2 m_0} \cdot \frac{1}{n^2} \quad , \tag{2.13}$$

where $R_y = 13.6\ eV$ is the Rydberg energy, ϵ is the dielectric constant of the semiconductor material in which the exciton is located, μ is the exciton reduced effective mass relative to the electron rest mass m_0 and n is an integer representing the quantum number of the energy level.
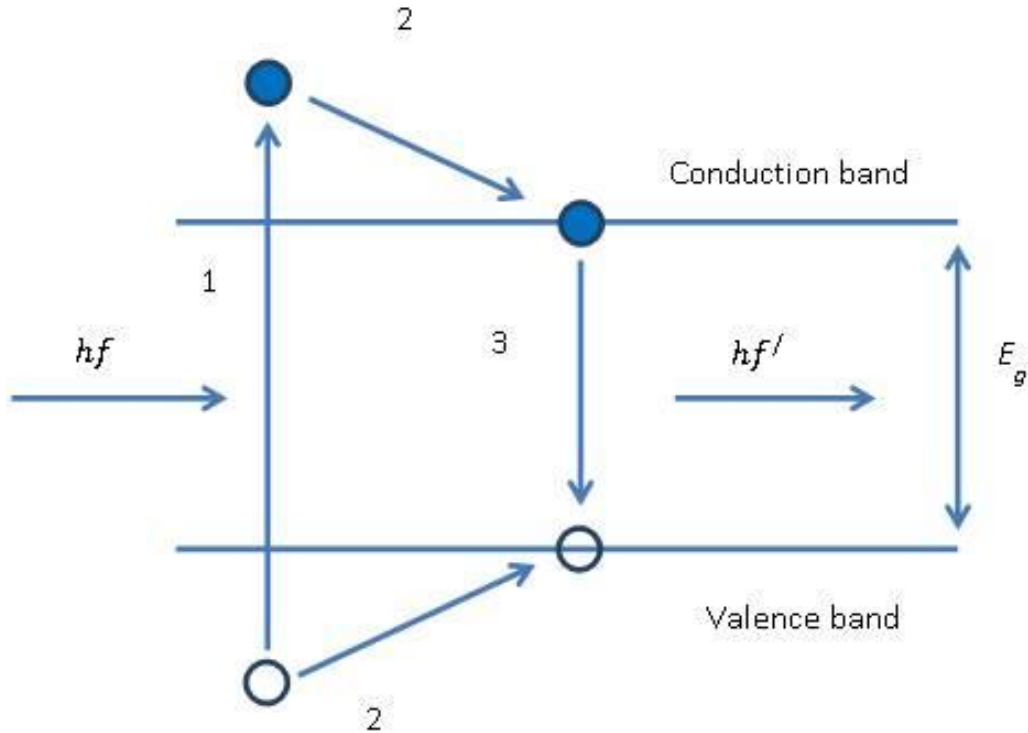
FIGURE 2.3: The PL process occurs in three steps. (1) An electron is excited to the conduction band by an incident photon having energy hf equal or greater than the band gap energy E_g, leaving a hole in the valence band. (2) Through non-radiative transitions, both electron and hole relax to their corresponding positions of minimal energy. (3) The de-excitation process completes by their recombination resulting in radiation of a photon of energy $hf' = E_g$.

A non-radiative decoupling of the exciton may take place, allowing the electron and hole to move independently through the lattice. More interestingly, the electron can recombine with the hole, emitting light of energy hf' that is dependent on the band structure, the band-gap energy, the exciton binding energy, the applied fields and confined energy levels, etc. A relation for temperature, T, dependence of band gap energy, $E_g(T)$, thus photoluminescence, has been proposed by Varshni [30],

$$E_g(T) = E_g(0) - \frac{\alpha T^2}{T + \beta} \ , \tag{2.14}$$

where α and β are constants. The equation satisfactorily represents the experimental data for diamond, Si, Ge, 6H-SiC, GaAs, InP and InAs [30]. The emitted light may be detected, revealing information about the optical properties of the investigated material.

2.3 Quantum dot excitons in a magnetic field

There are two models([31]), Fock-Darwin and excitonic, in order to understand the photoluminescence in magnetic field (magneto-PL) and behaviour of exciton in a magnetic field.

2.3.1 Fock-Darwin model

In the Fock-Darwin model, the energy levels of an electron are described in a 2D harmonic potential of energy $\hbar\omega_0$ in a perpendicularly applied magnetic field with radial quantum number (Landau level index) n and orbital angular momentum quantum number $l(l = 0, \pm 1, \pm 2, \pm 3)$

$$E_{(n,l)} = E_0 + (2n + |l| + 1)\hbar\sqrt{\omega_0^2 + \frac{\omega_c^2}{4}} - \frac{1}{2}l\hbar\omega_c \ , \tag{2.15}$$

where E_0 is the vertical confinement energy, i.e., the confinement energy in the direction of the applied magnetic field and ω_c is the cyclotron frequency. A typical Fock-Darwin spectrum calculated using $\hbar\omega_0 = 3 \ meV$ and $m_e = 0.067 \ m_0$ is shown in (Fig. 2.4). It may be noted that in analogy to the shell of the atoms, the radial quantum number n defines a series of occupancy energy levels and are therefore often labelled as s, p, d etc. [32, 33]. It can be seen in the figure that at low fields the magnetic energy is small compared to the quantisation energy so the former acts as a small perturbation to give a diamagnetic shift. At high fields it is the other way round: the magnetic energy dominates the quantization energy and thus the energy shift becomes linear, a behaviour of Landau levels. The first notable approximation of the Fock-Darwin description is that it doesn't take into account the Coulomb interaction between the charge carriers (electron and hole), i.e., it describes a single particle system. This not only neglects the Coulomb interaction between electron and hole but also any electron−electron interactions in the case of multiple occupancy. If it is nevertheless applied to exciton it is implicitly assumed that the wave-functions of the electron and hole have an indistinguishable form in equivalent levels n [34]. Thus $\hbar\omega_0$ becomes the sum of the electron and hole confinement energies, the cyclotron energy is found by using the reduced exciton mass rather than the electron effective mass [35]. The second approximation of the model is the symmetric confining potential, which causes the degenerate excited states.
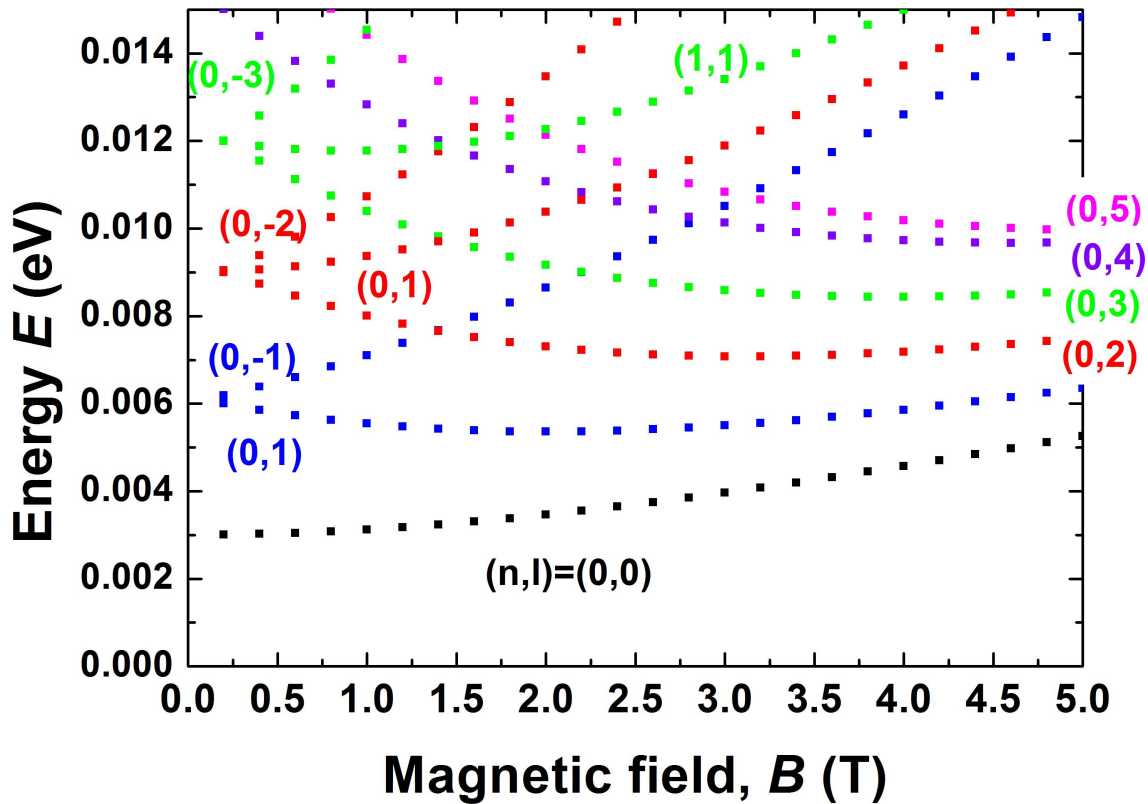
FIGURE 2.4: Fock-Darwin spectrum, calculated according to equation 2.15, using $\hbar\omega_0 = 3\,meV$ and effective mass $m_e = 0.067\,m_0$, for the principal quantum number (Landau-level index) $n = 0, 1$.

Practically, an asymmetry in the shape of the dots can split this symmetry, for instance, asymmetry by extension in one crystallographic direction in the plane of the sample [36] by piezoelectric effects [37] or the asymmetry in crystallographic surfaces at opposite sides of the dots [38]. Accounting for such effects needs considerably more refined models that cannot be described analytically and quite often require particularized information about the shape of the dots to be applied accurately. However, the Fock-Darwin model gives a good first-order approximation description of QD states in magnetic field, even when the dots are multiply-occupied [39].

Low-field and high-field regimes

For a QD in low magnetic field, i.e. when the magnetic length, $l_B = \sqrt{\frac{\hbar}{eB}}$ is much greater than the size of the confined exciton wave-function (2 x Bohr radius) in the

plane perpendicular to the applied field and the cyclotron energy is small, an applied magnetic field provides a small perturbation, giving a parabolic field dependence of the energy (diamagnetic shift) if the Zeeman terms are ignored [40–42] i.e.,

$$\Delta E = \frac{e^2 a_B^2}{8\mu} B^2 \ ,$$

(2.16)

where $\frac{e^2 a_B^2}{8\mu} = \Gamma$ is the diamagnetic shift coefficient, μ is the reduced mass of exciton and a_B is the exciton Bohr radius. On the other hand, in the high-field regime when the magnetic length, l_B becomes much smaller than exciton Bohr radius and where the cyclotron energy is large, the spatial confinement in the plane perpendicular to the applied field is dominated by the magnetic confinement, and can be neglected, effectively resulting in a 2D system with a field applied perpendicular to the plane. Therefore, the energy shift is given by that of the lowest Landau level:

$$\Delta E = \frac{1}{2}\hbar\omega_c \ ,$$

(2.17)

and is expected to be linear in B. It may be noted that the field dependence of the exciton binding energy is neglected here. For 3D, this is weak, going as $logB^2$ as B tends to infinity, while for two dimensions, it goes as $\sqrt{B}$ [43]. In between the two regimes, i.e., low field and high field, there exists an intermediate field regime where the magnetic field is neither weak nor strong and is analytically most difficult to deal with. Neverthless, the trend between the two limits must be continuous and analytic (there is no phase transition), and for filling the gap some interpolation can be used. A Pade interpolation scheme between these two regimes, in two dimensions, was introduced by MacDonald and Ritchie [43]. Janssens et al proposed another interpolation, where the field dependence of the exciton energy in a quantum disk was numerically calculated [44]. They found good agreement of their numerical results with the empirical function :

$$\Delta E = \frac{\beta B^2}{1 + \alpha B} \ .$$

(2.18)

Where α and β are parameters. It is worth mentioning that the functional form of this expression is similar to one that is widely used to describe the temperature dependence of the energy gap in semiconductors [45]. Equation (2.18) reduces to equation equation (2.16) for small fields ($\alpha\beta << 1$), from which it can be seen that $\beta = \frac{(e^2 a_B^2)}{(8\mu)}$, while at high field ($\alpha\beta >> 1$), equation (2.17) is reproduced, therefore $\frac{\beta}{\alpha} = \frac{e\hbar}{2\mu}$. Nevertheless, this equation has no physical foundations, and no advantage in terms of functional use compared to the Fock-Darwin model and the excitonic model [31] that is discussed below. Furthermore, it can be proved that, in the pertinent limits, the Fock-Darwin expression also reduces to equations equations (2.16) and (2.17). If only a single electron$-$hole pair confined in the dot ($n = l = 0$) is considered, equation (2.15) becomes

$$E = E_0 + \hbar\omega_0(1 + \frac{\omega_c^2}{4\omega_0^2})^{\frac{1}{2}} \quad . \tag{2.19}$$

To expand the square root term, the binomial series can be applied. In low magnetic fields ($\omega_0 >> \omega_c$), the higher power terms of the expansions can be neglected and only the first two terms are considered, so

$$E = E_0 + \hbar\omega_0(1 + \frac{\omega_c^2}{8\omega_0^2}) \quad , \tag{2.20}$$

which can be written as

$$\Delta E = \frac{(\hbar\omega_c)^2}{8\hbar\omega_0} \quad . \tag{2.21}$$

This is proportional to B^2 via the cyclotron energy. Equation (2.16) can be rewritten by putting $E_B = \frac{\hbar^2}{2\mu a_B^2}$ (the binding energy of an isotropic 3D exciton) and $B = \frac{\omega_c \mu}{e}$, thus

$$\Delta E = \frac{\hbar\omega_c^2}{8(2E_B)} \quad . \tag{2.22}$$

This implies that $\hbar\omega_0 = 2E_B$. In high magnetic field ($\omega_c >> \omega_0$), it can be simply noted that both equations (2.19) and (2.17) give an identical energy shift. The

physical equivalence of the Fock-Darwin approach and the excitonic approach (discussed below) is manifested by these significant results. The interpretation of this is that, in an exciton, the electron and hole are confined in a harmonic potential that is produced by their Coulomb interaction. Similarly, the exciton binding energy is increased by the enforced wave-function overlap of the electron and hole in a dot.

2.3.2 Excitonic model

The excitonic model [31] and Fock-Darwin model are different from each other in terms of the Coulomb interaction between the charge carriers of the exciton that has been taken into account and neglected, respectively. In the excitonic model, no intermediate field regime between the low-field and the high-field limits has been considered, rather the one transforms to the other without any discontinuity in $E(B)$ or its derivative [46] . Hence

$$E = E_0 + \frac{e^2 a_B^2 B^2}{8\mu} \qquad for \ B \leq B_c \ , \qquad (2.23)$$

$$E = E_0 + E_1 + \frac{\hbar e B}{2\mu} \qquad for \ B \geq B_c \ , \qquad (2.24)$$

where E_1 is a continuity constant and B_c is the critical field at which the low field regime shifts to the high field regime. Imposing the continuity condition in the derivative at $B = B_c$ gives

$$B_c = \frac{2\hbar}{a_B^2 e} \quad . \qquad (2.25)$$

This equation becomes satisfied when $l_c = \frac{a_B}{\sqrt{2}}$, where l_c is the critical magnetic length i.e., $l_c = \sqrt{\frac{\hbar}{eB_c}}$. It implies that when the magnetic length is $\frac{1}{\sqrt{2}}$ times the zero-field exciton Bohr radius, the high-field regime is reached. By applying the condition of continuity in E at $B = B_c$, we find

$$E_1 = \frac{e^2 a_B^2 B_c^2}{8\mu} - \frac{\hbar e B_c}{2\mu} \quad . \qquad (2.26)$$

Putting equation (2.25) into equation (2.26), we obtain

$$E_1 = \frac{-\hbar}{2\mu a_B^2} \quad . \tag{2.27}$$

So, equations (2.23) and (2.24) can be rewritten by substituting the value of E_1 from equation (2.27):

$$E = E_0 + \frac{e^2 a_B^2 B^2}{8\mu} \qquad for \ \ B \leq B_c \tag{2.28}$$

and

$$E = E_0 - \frac{\hbar}{2\mu a_B^2} + \frac{\hbar e B}{2\mu} \qquad for \ \ B \geq B_c \ . \tag{2.29}$$

The equivalent expressions to the above equations, for fitting the two field limits in a single process (Fig. 2.5), are given by
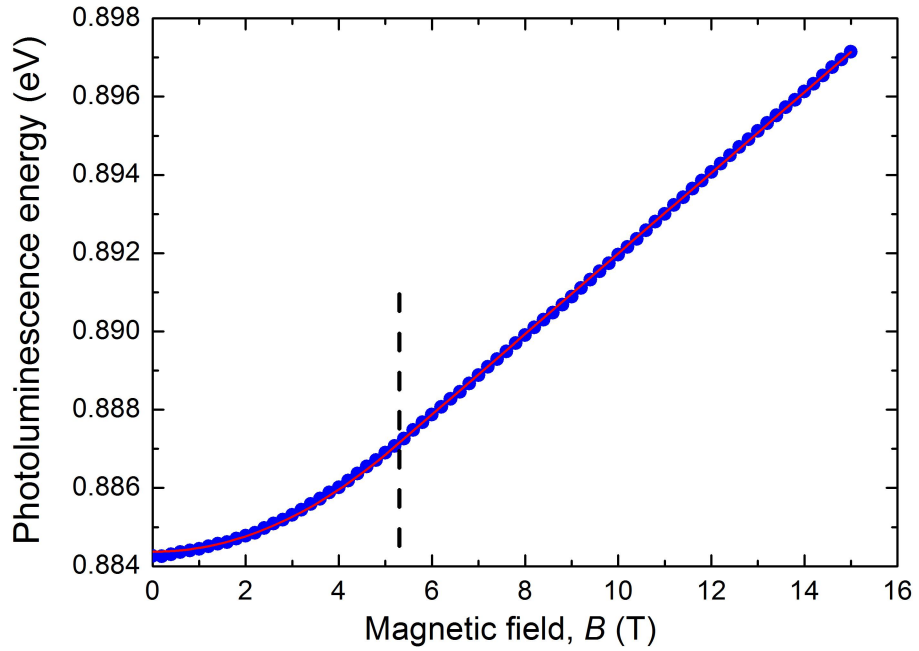
FIGURE 2.5: Dependence of photoluminescence on magnetic field expected according to Excitonic model. The red line shows a typical fit while the vertical dashed line represents the transition occurring from the low-field regime to the high-field.

$$E = a + bB^2 \qquad for \ \ B \leq B_c \tag{2.30}$$

and

$$E = a - bc^2 + 2bcB \qquad for \ B \geq B_c \ , \qquad (2.31)$$

where $a = E_0$ and $b = \frac{e^2 a_B^2}{8\mu}$ and $c = B_c$. All three approaches (the Fock-Darwin model, equation equation (2.18) and excitonic approach) result in the same number of parameters e.g., a, b and c in the case of excitonic model, when only the ground state recombination is considered.

Chapter 3

Literature Review

3.1 Nanostructures for telecom wavelengths

3.1.1 InAs quantum dots

InAs nanostructures have been intensively studied over the last decades, with the aim of obtaining telecom wavelength (1.3 - 1.6 μm) [21, 47, 48]. Many approaches have been adopted to extend the wavelength to telecom window (1.3 - 1.6 μm) [49–52]. For instance, the wavelength of emission from InAs QDs can be increased to 1.56 μm by deposition of GaSb on InAs/GaAs self-assembled QDs [50]. InAs/InP nanostructures can also extend the wavelength to 1.55 μm by tuning the growth rate of the capping [53]. Similarly, for extending the wavelength to 1.3 μm, different methods have been practiced. For example, increasing the growth rate of InAs and QD size results in redshift [54, 55]. An alternative approach to extend the wavelength to 1.3 μm is the growth of InAs QDs on GaAs substrate and covered with a GaAsSb strained reducing layer , where Sb composition is set as 14 % [56]. The wavelength could be extended further to 1.6 μm at RT in such structure by increasing the Sb composition to 26% [57].

3.1.1.1   InAs/GaAs QDs

InAs/GaAs QDs have been grown with GaAs barriers emitting at 1.4 μm and at 1.48 μm with InGaAs barriers, with small full width at half maximum (FWHM), i.e. 14 meV [58]. Temperature and excitation density dependence of photoluminescence in annealed InAs/GaAs QDs was reported which was explained as independent escape and capture of electrons and holes in the dots [59]. The RT optical properties of single InAs/GaAs QD layers and InAs/GaAs QD bilayers have been experimentally and theoretically investigated achieving ground state optical emission at wavelengths in excess of 1300 nm by using QD bilayers [60]. Under appropriate growth conditions and optimized strain interaction between two closed stacked InAs/GaAs QD layers, the emission wavelength of the QD was extended to 1400 nm with GaAs capped QDs, and to 1515 nm when an InGaAs cap is applied to the upper QD layer, while the inhomogeneous broadening is very low [61]. PL studies performed on GaAs capped InAs/GaAs QD samples show that the emission wavelength increases with decreasing InAs deposition rate, reaching a maximum around 1.3 μm, with the linewidth decreasing from 44 to 27 meV [62]. Reference [62] also shows that the number density, total QD volume and size fluctuation all decrease significantly as the growth rate is reduced, revealed by studies on uncapped dots using scanning tunnelling microscopy (STM). InAs/GaAs quantum dots have been grown (at very low growth rates) with scanning probe microscopy using continuous InAs depositions of up to five monolayers (ML) without QD coalescence, resulting in relatively large coherent QDs that exhibit strong room temperature photoluminescence at a wavelength of 1.3 μm when capped with GaAs [63]. 1.3 μm room temperature electroluminscence from InAs/GaAs self-assembled quantum dots has been shown by Murray et al [64].

3.1.1.2   InAs/InGaAs/GaAs QDs

One of the ways of controlling the emission wavelength is embedding the InAs QDs in InGaAs quantum wells (DWELL). These have been studied on different substrates and have become favoured for the fabrication of long wavelength devices, resulting in the formation of QD lasers with a low threshold current density and high characteristic temperature [65–68]. Such DWELL structures have also demonstrated high dot density (important for effective gain thus good for lasing) and good carrier capture ability [69]. The optical efficiency in InAs/InGaAs/GaAs has been enhanced by increasing the growth rate of GaAs and InGaAs layers, and by increasing the InAs coverage [69]. The QD density and emission wavelength strongly depend upon the In composition of thes InGaAs quantum well (QW), with 15% In composition in the well have been found as optimum for 1.3 μm emission. 1.32 μm emission has been reported from such structures at room temperature [69].

There are other approaches adopted to achieve the redshift of the QD emission, important for extension of device operation to 1.55 μm [70], for instance, (i) changing the band discontinuity between QDs and confining layers (CLs), (ii) the reduction of the energy gap of the QD material, and (iii) the increase of the QD dimensions. The first approach has been the most exploited, as the emission wavelength can be tailored to 1.31 μm at room temperature by insertion of InGaAs confining layers below and/or above the QDs [71–75]. InGaAs CLs cause a reduction of the QD strain due to their reduced lattice mismatch to InAs QDs that therefore contribute to the redshift of the QD light emission. Furthermore, when InAs QDs are embedded with InGaAs layers, the QD dimension increases due to strain-driven In migration from the upper InGaAs confining layers to the QDs, resulting in redshift of InAs QD emission energy [71,76]. The second approach is more useful for achieving the QD emission at 1.55 μm by growing InAs QDs either directly on InP (see section 3.1.1.3) [77] or on metamorphic buffers on GaAs [78–80], thus reducing the QD strain and decreasing the QD energy

gap. In the third approach, the QD dimensions have been increased by using other MBE techniques like atomic layer molecular beam epitaxy (ALMBE) [81] and by reducing the InAs growth rate [82, 83].

InAs/InGaAs/GaAs QD structures, where InAs QDs are embedded in InGaAs metamorphic confining layers (CLs) based on GaAs substrates, can be a source of redshifted emission by increasing the indium composition in the InGaAs CLs and by decreasing the QD strain [78]. The strain can be reduced by controlling the QD-CL mismatch, a function of lattice parameter a_{LCL} of the lower confining layer (LCL) of any given composition. Photoluminescence and photoreflectance give the experimental evidence of the redshift [78, 84], while the dependence of the extent of strain relaxation of the LCLs on their thickness is confirmed only by photoreflectance measurements [85]. A few optical properties of QD nanostructures can be tailored by using QD strain as a parameter, which changes the energy gap of the QD material, and can be controlled not only by the CL composition, as already considered, but also by exploiting the LCL thickness-dependent strain relaxation that affects their lattice parameter. Thus, the indium composition that changes band offsets (which in turn confine the carriers into the dot volume) and strain/QD-CL mismatch, and the LCL thickness which affects only the mismatch, can be used as two independent parameters to tune the emission energy. Therefore, such InAs/InGaAs/GaAs structures are named as strain-engineered and have been proven as a useful system for redshifting emission [70]. The emission wavelength has been extended to 1.52 μm by applying a 4 nm InGaAs strained reducing layer (SRL) to InAs bilayer QDs grown on GaAs substrates, where QD size and density and the composition of the SRLs are controlled [86].

3.1.1.3   InAs/InP QDs

InAs/InP structures (mismatch = 3.2 %) have been probed for exploitation as laser sources at 1.55 μm [87, 88]. High quality (lower threshold currents and reduced temperature dependent) InAs/InP self assembled quantum dots emitting at $1.5 - 1.6 \mu m$ have been fabricated. The growth conditions [89, 90], substrate orientation [91, 92] and the nature of surrounding materials (alloying effects) [93, 94] are the critical factors for the morphological and thus optical properties of the islands. The emission wavelength of InAs dots based on InP can be tuned through the combination of the use of a sublayer of GaP and a two-step capping procedure, in which a narrow size distribution and high density of dots can be maintained [95]. The size uniformity and density of the InAs dots grown on high index (3 1 1)B InP substrates is improved compared to those grown on low index (1 0 0) [96]. InAs QDs grown on InP (3 1 1)B substrates have demonstrated lasing at 1.5 μm approximately at room temperature with low threshold current densities, promising for applications in telecommunications [97].

3.1.1.4   InAs/Si QDs

Due to the indirect band gap, Si is not suitable for light emission applications. Therefore, it has been proposed to insert direct band gap InAs in a Si matrix to improve the luminescence efficiency [98]. Despite the large lattice mismatch (approximately 10.6%) between InAs and Si systems, InAs QDs in Si(1 0 0) matrix [99] and capped with Si [98] have been fabricated under optimized growth conditions emitting at 1.3μm near room temperature. Their lateral sizes vary from 5 nm to 80 nm (for uncapped islands) and 2 to 5 nm (for Si capped), critically depending upon the growth conditions and island heights, respectively [98]. The large mismatch problem is overcome by small coherent islands of InAs. The critical thickness, at which three dimensional islands appear, was found to be 0.3 - 0.7 monolayers. By using

InAlAs/GaAs strained-layer superlattice serving as dislocation filter layers (DFLs), a high-performance 1.3 μm InAs/GaAs quantum-dot laser directly grown on Si substrates has also been achieved [100].

3.1.2 Other systems

In order to achieve long wavelengths, for applications in telecommunications, systems other than the InAs QDs, that have been discussed in the previous sections, have also been investigated. For instance, isolated InAs/InP quantum wires (QWrs) have been grown using conventional epitaxial techniques where an optimal InAs thickness is adjusted, and highly asymmetric nanostructures, with average length exceeding more than ten times their width, has been shown by atomic force microscopy (AFM) [101]. From such structures, strong photoluminescence from individual quantum wires at 1.5 μm has been revealed by high resolution optical investigation of as-grown samples [101]. As the optical properties of self-assembled nanostructures are a function of their sizes, different ways, therefore, have been studied to modify the height of InAs/InP quantum wires in order to change the photoluminescence emission wavelength: varying the amount of InAs deposited; control of As/P exchange process during growth of InAs on InP for QWr formation or of InP on InAs for QWr capping [102]. A fine tuning of QWr emission wavelength between 1.2 and 1.9 μm at room temperature has been provided by combination of these three approaches [102].

Stacked layers of high-density GaSb/GaAs quantum rings have been grown using molecular-beam epitaxial growth [103]. An excellent structural quality of structures, with no threading dislocations or defective rings, has been revealed by X-ray diffraction and transmission electron microscopy and due to a low level of unintentional p-doping in the GaAs cap layer, a long-wavelength photoluminescence peak at 1.3 μm is observed [103].

GaInNAs can be grown pseudomorphically on a GaAs substrate, while having a band gap energy suitable for long-wavelength laser diodes (1.3 - 1.55 μm and longer wavelengths), resulting in fabrication of a deep quantum well [104]. The properties of GaAsSb/InGaAs type-II bilayer quantum-well structures grown by molecular-beam epitaxy for use in long-wavelength lasers on GaAs substrates have been investigated [105]. Room-temperature photoluminescence at wavelengths as long as 1.43 μm has been exhibited by such structures with layer strains and thicknesses designed to be thermodynamically stable against dislocation formation [105]. Lasers with threshold current densities of 120 A/cm^2 at 1.17 μm, and 2.1 kA/cm^2 at 1.21 μm have been obtained [105].

High-performance InGaAs and InGaAsN QWs lasers have been grown by metal organic chemical vapor phase deposition (MOCVD) using AsH as the As-precursor, which has shown the emission wavelengths ranging from 1170 to 1315 nm [106]. 1300-nm InGaAsN single-QW lasers showed low threshold current density and high temperature operation [106].

InGaAsN/GaAs quantum wells (QWs) have been grown by molecular beam epitaxy and lasers based on such structures have been demonstrated to emit at wavelengths from 1.28 - 1.3 μm with a low-threshold current density [107]. Metal organic chemical vapor deposition (MOCVD) grown InGaAsN-GaAsSb type-II quantum wells on GaAs substrates have shown low temperature (30 K) long wavelength photoluminescence emission (1400 - 1600 nm) [108]. It has been shown by room temperature photoluminescence data that such type-II QW design is a promising candidate for realizing long wavelength GaAs-based diode lasers beyond 1500 nm [108]. Spontaneous emission spectra from multiple quantum well lasers grown by molecular beam epitaxy with 25-Å-wide GaAs wells have been recorded by opening a window in the top contact stripe [109].

3.2   Confinement of exciton in QDs

Confinement of excitons in quantum dots appears when the dot size is in the order of the Bohr radius of the bulk exciton, which results in a blue-shift in exciton energy. The properties of an exciton are subject to the confinement of the particles, i.e. electron and hole, that depends on the size and shape of the semiconductor nanostructure. The confinement can be tuned through a selection of barrier materials and structure to obtain various band offsets. Besides, important information about the carrier confinement can be obtained by application of an external magnetic field. Confining potential and electrostatic interactions between the carriers are the two main factors which affect the energy structure of carrier complexes confined to QDs. Significant attempts have been made to relate the morphological properties to the properties of excitons confined in QDs [110]. Various techniques, used for probing the exciton confinement in nano-structures, are presented below.

3.2.1   Morphological properties

If all morphological properties of QDs are known, then confined states can be calculated. The $GaAs/Al_xGa_{1-x}As$ structure is an easy case, due to being strain free, to probe the exciton confinement. Low-temperature photoluminescence of $GaAs/Al_xGa_{1-x}As$ quantum dots has been carried out where the energies of the confined states in the system has been determined by recombination between confined electrons and holes bound to carbon acceptors in the dots [111]. The excitonic properties in unstrained $GaAs/Al_xGa_{1-x}As$ QDs have been investigated in the presence of a magnetic field, where the magnetic field dependence of the electron-hole Coulomb interaction energy has been revealed [112]. GaAs/AlGaAs QDs have been analyzed with scanning tunneling microscopy and structural details and a quantitative chemical analysis of QDs of different sizes have been obtained where most QDs were found to be pure GaAs [113].

3.2.2   Single dot spectroscopy

Single dot spectroscopy (or μ-PL spectroscopy) techniques have been used to study InP self-assembled QDs embedded in $Ga_{0.5}In_{0.5}P$ layers with a thickness of 180 nm, where the activation energy of each dot has been revealed to be different, ranging from 5 meV to 40 meV [114]. Many individual single InAs QDs have been probed using high-resolution low-temperature spectroscopy showing a statistical distribution of homogeneous line-widths with a peak value of ~ 120 μeV [115]. The technique has been used also to study the carrier transport characteristics for the luminous efficiency of self-organized InAs/GaAs quantum-dots [116]. Similarly, the emission properties of single CdTe/ZnTe QDs grown on Si(001) substrates have been studied where exciton, biexciton, and two oppositely charged excitons in the emission spectra of single QDs were identified by power-dependent and temperature-dependent micro-photoluminescence spectroscopy measurements [117].

3.2.3   Deep level transient spectroscopy (DLTS)

Due to resemblance between QDs and defects, deep level transient spectroscopy (DLTS), with QDs placed in a depletion region of a Schottky contact (metal-semiconductor contact) or a p-n junction (contact between p-doped and n-doped semiconductors) has been used to probe the electronic energy levels of QDs [118]. A capacitance depends on the width of the depletion region, which, in turn, depends on the applied bias and doping concentration. Capacitance-voltage measurements $(C - V)$, therefore, can be used to measure the depth profiles of the doping concentration in semiconductor devices. The measured capacitance is a function of charge population in deep levels (or QDs situated inside the depletion region). $C - V$ and DLTS have been used to study GaSb/GaAs QDs where the mean activation and localization energy of the QD ensemble have been found to be 115 ($\pm$5) meV and 335

(± 15) meV, respectively [119]. DLTS has been used for the study of InP dots embedded in GaInP where an activation energy of 220 meV for one electron ground state of the dots has been found [120]. The electronic properties of high purity self-assembled GaSb/GaAs quantum dots have been studied by DLTS and the localization energy of the hole (electron is not confined due to being in type-II QDs) was found as 609 meV with an apparent capture cross section of $1 \times 10^{-12} \ cm^2$ [121].

3.2.4 Wave-function imaging

3.2.4.1 Scanning tunnelling microscopy (STM)

Imaging of the electron's wave interference and quantum confinement have been achieved by direct scanning tunneling microscopy (STM) [122]. The technique has been used to probe the electronic wave-function in InAs/ZnSe core/shell nanocrystals where images taken at a bias corresponding to the s conduction band state revealed that it is localized in the central core region, while those taken at higher bias probing the p state showed that it extends to the shell [123]. The electronic structure of the conduction band states in InAs quantum boxes embedded in GaAs have been investigated using cross-sectional STM and the direct observation of standing wave patterns in the boxes at room temperature has been reported [124]. Substitutional donor Si at Ga sites (Si_{Ga},) has been identified and characterized in GaAs by STM [125].

3.2.4.2 Magneto-tunneling spectroscopy

In order to probe the electron's confinement in QDs, buried hundred of nanometers below the surface, magneto-tunneling spectroscopy has been used where a two dimensional image of its wave-function is produced [126]. Here the effect of the classical Lorentz force on the motion of a tunneling electron has been exploited, which can be

regarded as the momentum (k) space analog of scanning tunneling microscopy imaging, revealing the elliptical symmetry of the ground state and characteristic lobe of the higher energy states. A correlation between the spatial symmetry of the electron wave function and the morphological properties of quantum dots grown on differently oriented GaAs substrates has been drawn [127].

3.2.5   Magneto-photoluminescence

The study of photoluminescence in magnetic fields (Magneto-photoluminescence) has been shown as an effective tool to probe the exciton wave-function inside the quantum dot [31]. When the length of the magnetic field becomes less than the exciton Bohr radius, the magnetic confinement comes into play, in addition to spatial confinement, and the magnetic field does more than just perturbing the wave-unction, which is indicated by a transition from parabolic dependence of PL energy to the linear dependence with increasing magnetic field. The point of cross-over of PL energy from parabolic to linear gives the wave-function of exciton. By using the excitonic model (discussed in the previous chapter), the properties of the exciton, diamagnetic shift coefficient, Bohr radius and effective mass are determined, by which the confinement of exciton can be probed. The technique has been used to investigate the exciton confinement in self-assembled InAs/GaAs QDs where the temperature dependence of the magnetic field dependence of the PL has been studied [128]. Exciton confinement in InAs/InP quantum wires and quantum wells has been studied in the presence of a magnetic field where a substantial penetration of both electron and hole into the InP barrier has been recorded [129]. Magneto-photoluminescence has been used to determine the influence of substrate orientation and growth interruption on the electronic properties of InAs/GaAs QDs where it has been found that electronic confinement for the (100) substrate is already strong without growth interruption and the interruption does not affect the confinement, while for the (3 1 1)B substrate, the strong

confinement of the charges only occurs after a growth interruption is introduced as longer interruptions result in higher dots [130].

Chapter 4

Epitaxy

The deposition of atomic or molecular layers on each other to form a coherent crystalline structure, is typically termed as epitaxy and means "arrangement on" [131]. In 1928, Royer formulated a rule of epitaxy as "epitaxy occurs only when it involves the parallelism of two lattice planes that have networks of identical or quasi-identical form and of closely similar spacings". Later on, experiments proved that epitaxy takes place if the lattice mismatch, defined as $100(\frac{a_0 - a_s}{a_s})$, where a_s and a_0 are the corresponding lattice constants in the substrate and growing film, respectively, is not larger than 15% [131]. In the lattice-mismatched heteroepitaxial layers, misfit dislocations (MDs) usually occur at the interface area. Geometrically, the misfit is accommodated between "epitaxy" and "substrate" crystals by the MDs as demonstrated in (Fig. 4.1). Accordingly, there are unpaired atomic planes which terminate at the interface from above and which constitute the MDs.

To understand the concept of a dislocation, strain localization is needed in a small region around the dislocation, which requires the bonding across the interface to be strong enough.
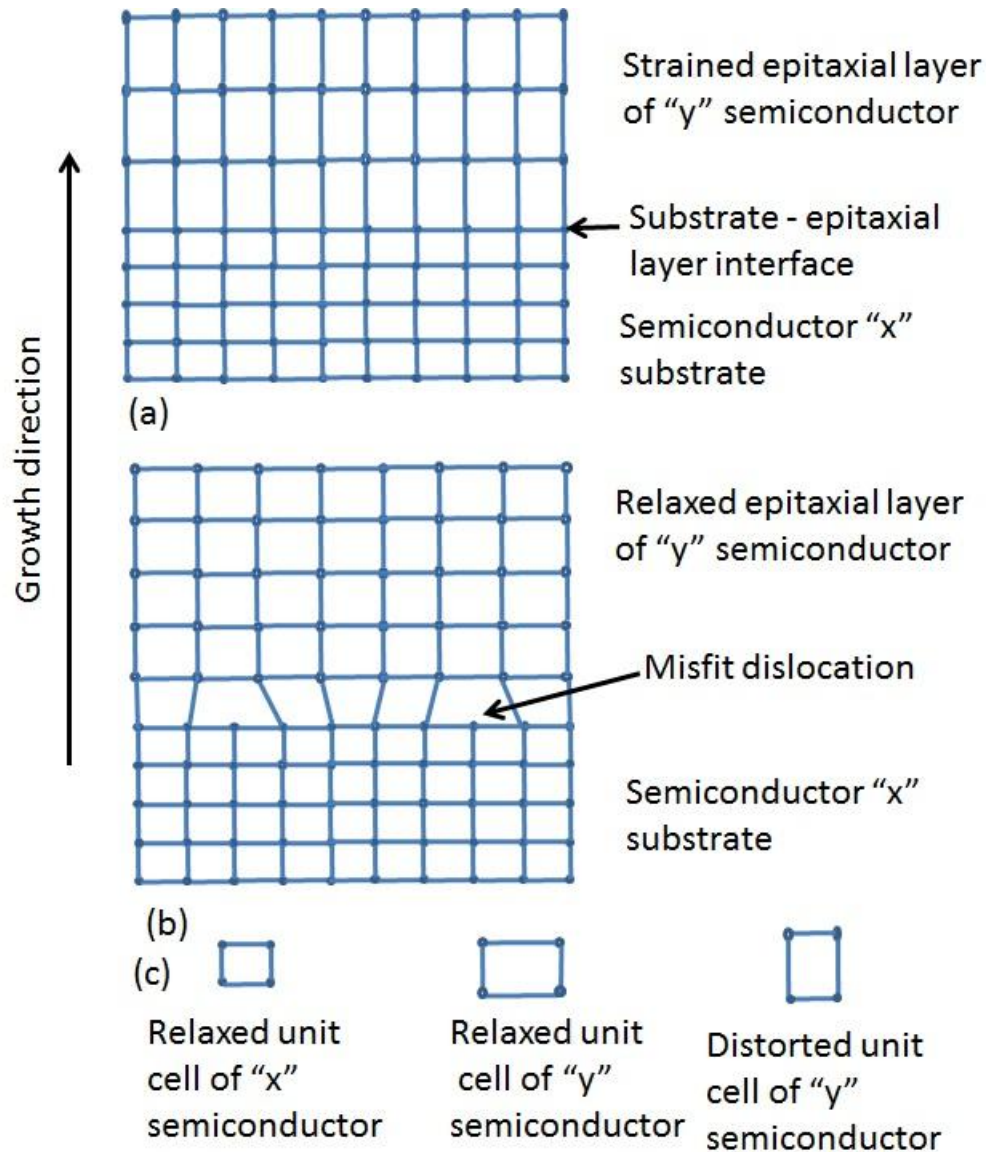
FIGURE 4.1: Schematic representation of (a) strained and (b) relaxed epitaxial layers of a lattice mismatched heterostructure, as well as (c) strained and relaxed unit cells.

The epitaxial growth is termed as heteroepitaxial, if chemical composition and sometimes structural parameters of a growing epilayer are different from those of the substrate. The growth process in heteroepitaxy is a strong function of coherence and incoherence of the epilayer with the substrate, i.e. whether the interface between the epitaxial overgrowth and the substrate is crystallographically perfect or not. If there is incoherence of the overgrowth with the substrate, then the epilayer is free to

adopt any in-plane lattice constant that minimizes its free energy. If the overgrowth is coherent with the substrate, then energy minimization is achieved by adopting the in-plane lattice constant of the substrate (Fig. 4.2). Its overall free energy is significantly increased by the resulting elastic strain energy.
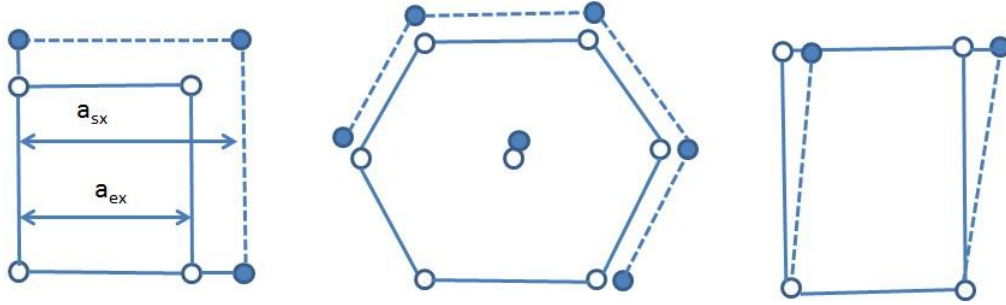
FIGURE 4.2: A top view of atomic arrangements at interfaces of the epilayer and substrate, "*e*" / "*s*", systems of different crystallographic symmetry. Empty circles represent the substrate atoms while black dots stand for overgrowth atoms

The disregistry of the equilibrium interfacial atomic arrangements of the substrate and the unstrained epilayer is usually termed as "misfit". This disregistry results from differences in atomic spacings of lattice symmetries, which are characteristic of each of the two crystals in the absence of interfacial interaction between them.

It is understood that if there is sufficiently small misfit between a substrate and a growing layer, the first atomic monolayers which are deposited will be strained to match the substrate and a perfectly matched (coherent) epilayer will be formed. As the layer thickness increases, the homogeneous strain energy becomes so large that a thickness is reached when it is energetically favourable for misfit dislocations to be introduced (see Fig. 4.1). The thickness of such growing layer for the strain relaxation was termed as a critical thickness, t_c, in the theoretical study by Frank and van der Merwe [132] and, later on, confirmed by various experimental observations. Finch and Quarrell [46] introduced the term "pseudomorphism" for such a state of the epilayer and substrate "*e*"/"*s*" system, where the thickness of the epilayer is

smaller than the critical thickness and was named as "pseudomorphic regime" in the literature.

In the system consisting of thickness in excess of the critical thickness (t_c) for plastic relaxation, MDs are formed, and the layers are termed as metamorphic buffers (MBs), which behave as a virtual substrate whose lattice parameter can be designed in order to control the mismatch between the buffer and upper part of the structure. The lattice parameter of the MB depends on its composition and thickness through the mechanism of strain relaxation, by which, for MB thickness larger than "t_c", partial relaxation of the elastic strain occurs and a network of MDs is formed.

4.1 Molecular beam epitaxy (MBE)

One of the most exploited techniques for growing thin layers in a controlled way is molecular beam epitaxy (MBE) [131], invented by J. R. Arthur and Alfred Y. Cho at Bell Telephone Laboratories United States in the late 1960s. Fig. 4.3 is a schematic diagram of an MBE, which consists of: effusion cells (or Knudsen cells) where the solid elements are heated and evaporated, liquid nitrogen to cool the chamber, an electron gun to provide electrons for reflection high energy diffraction (RHEED), which is explained below, a substrate heater/manipulator to provide heating of the samples and continuous rotation of the sample during the growth, which provides the lateral uniformity of the grown layers, a beam flow gauge to monitor the flow of atoms/molecules, a sample holder, a mass spectrometer (MS) to measure the masses and relative concentration of atoms or molecules, and a fluorescent screen for the pattern of RHEED. The MBE technique takes place in ultra-high vacuum (UHV), i.e. 10^{-8} Pa, in contrast to other epitaxial growth techniques, metalorganic vapour phase epitaxy (MOVPE) for instance, taking place in thermodynamic equilibrium. Exploiting its substantially more precise control of beam fluxes and growth conditions, the highest achievable purity of grown films is obtained due to the ultra-high

vacuum environment. Solid elements are heated in separate Knudsen cells. These have a small opening used as evaporation sources and for controlling the flux of evaporating content by its temperature, until they begin to slowly sublime. Vapour particles travel towards the target (substrate) without interacting, due to the long mean free paths under UHV growth conditions (hence molecular beam) until they reach the wafer, where they may react with each other and condense back to a solid state.
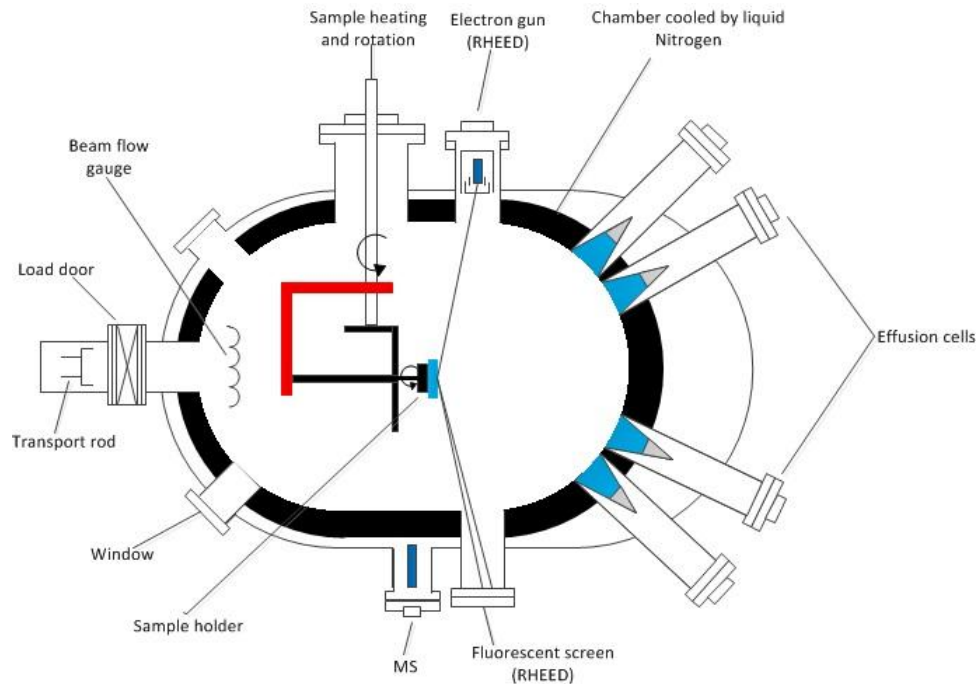
FIGURE 4.3: Schematic representation of an MBE chamber. Each effusion cell, also called a Knudsen cell, is a source of one element in the film which contains the elemental form in very high purity (greater than 99.99999% for Ga and As). The cell is heated to induce evaporation. In case of GaAs growth, the cell temperature is typically controlled for a vapour pressure of 10^{-2} to 10^{-3} Torr inside the effusion cell, which results in a transport of about 10^{15} molecules/cm^2 to the substrate when the cell's shutter is opened. To distribute the particles evenly on the substrate, the shape and size of the opening in the cell is optimized. They typically do not interact with other molecules in the beam due to the relatively low concentration of molecules, during the 5 - 30 cm journey to the substrate. To further even the distribution, the substrate is usually rotated at a few rpm.

On reaching the surface, the adatoms move by surface diffusion until they reach a thermodynamically favourable location to bond to the substrate. Molecules will dissociate to atomic form during diffusion or at a favourable site. Because the atoms require time for surface diffusion, the quality of the film will be better with slower growth, but on the other hand there is more chance to incorporate impurities even in UHV. Therefore, an optimum growth rate is adjusted. The quality of the film depends on temperature of the substrate too.

Typically, growth rates of about 1 monolayer (ML) per second provide sufficiently high quality. The substrate is rotated and its angular velocity is controlled for composition uniformity. Similarly the temperature of the substrate is tuned for optimizing the growth. A computer operates the shutters in front of each cell, controlling layer thicknesses precisely, down to a single layer of atoms. In this way, complex structures of layers of different materials may be fabricated.
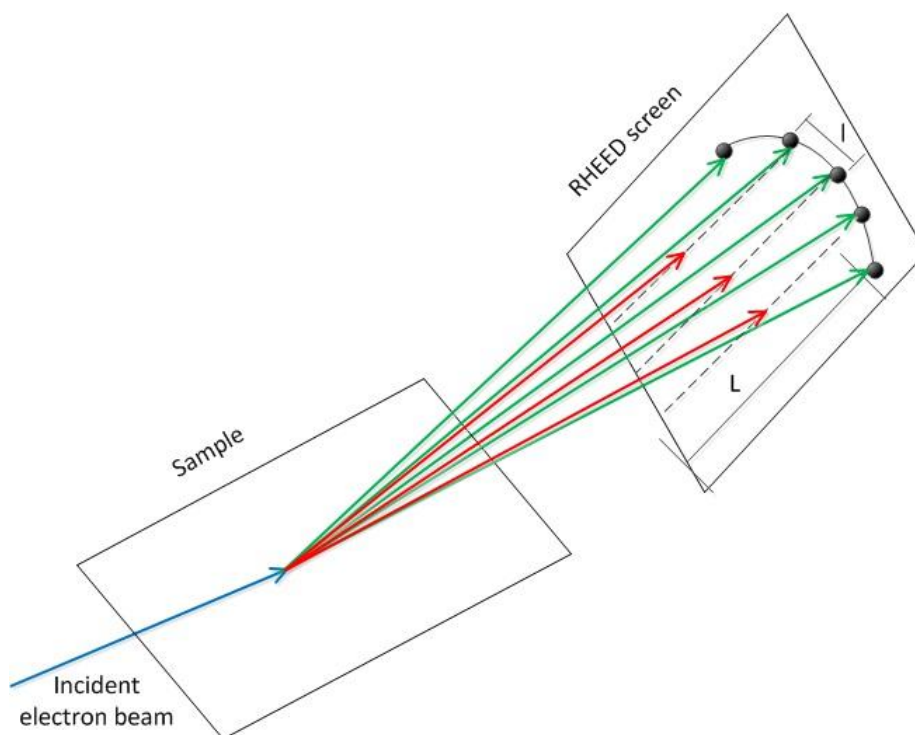
FIGURE 4.4: Schematic diagram showing the formation of a RHEED pattern, where L is the distance from the plane of the substrate to the diffraction pattern and l is the distance between streaks in the RHEED pattern.

Reflection high-energy electron diffraction (RHEED) is used for monitoring the growth process by gathering information only from the surface layer of the sample (Fig. 4.4), allowing orientations of the growth of 1 monolayer (ML) at a time. In a RHEED system, the electron gun produces a beam of high-energy electrons which hits the sample at a very small incident angle relative to the sample surface. Incident electrons diffract from atoms at the surface of the sample, and a few of the diffracted electrons interfere constructively at specific angles and form regular patterns on a fluorescent screen. The electrons interfere according to the position of atoms on the sample surface, so the diffraction pattern at the screen is a measure of the sample morphology.

4.2   Atomic layer MBE (ALMBE)

Atomic layer molecular beam epitaxy (ALMBE) is a modified version of MBE [133] where the molecular growth is perturbed periodically at atomic layer level by alternating or interrupting the molecular beams. Due to the periodic perturbation of the growth, which results in cyclic variations of surface stoichiometry, layer nucleation is enhanced which, in turn, induces 2D growth. One specific group of molecular beams (e.g. group V elements) are evaporated from a uniquely constructed effusion cell operating in pulsed mode. ALMBE has improved growth qualities under difficult growth conditions that would be impossible otherwise (e.g. by conventional MBE). ALMBE has the capability of growing at low substrate temperatures e.g., 350 °C, growing highly-mismatched hetrostructured systems with high-quality morphology. Pseudo-ternary hetrostructures, for instance GaAs/GaP/GaAs, containing two different elements of the same group (e.g., P and As both of group V), is not achievable by MBE due to mutual competition of elements for incorporation, resulting in difficult compositional control.

4.3 Growth modes

There are three different kinds of growth modes (Fig. 4.5) as determined by interface energy (which is function of strain resulting from lattice mismatch and strength of chemical reactions between film and substrate at interface) and surface free energies for the substrate and film materials [134].
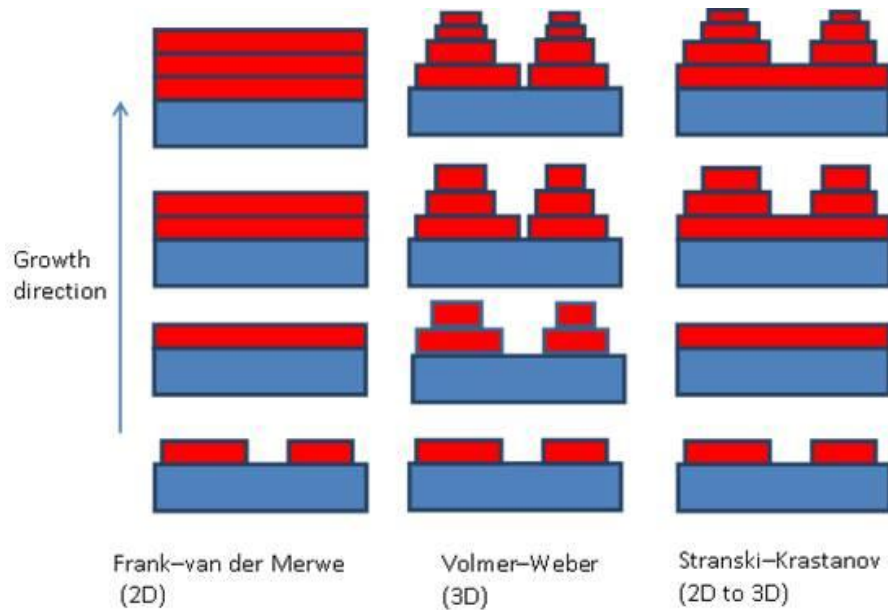
FIGURE 4.5: Schematic representation of different growth modes.

Frank-Van der Merwe (FM) growth: In Frank-Van der Merwe (FM) growth mode, also called layer-by-layer or two-dimensional growth mode, the atoms of the growing film are more bound to atoms on which the film is grown, than they are to each other.

Volmer-Weber (VW) growth: Opposite to FM growth, in the Volmer-Weber (VW) growth mode (also called island or 3D growth), the interatomic bonds between the different atomic species within the film material are much stronger than those between the atoms of the growing film and the substrate atoms.

Stranski-Krastanov (SK) growth mode: The more commonly investigated growth mode for QD formation is the Stranski-Krastanov (SK) growth mode, also known as layer plus island growth mode. SK growth takes place when two-dimensional (2D) layers, grown on a substrate with lattice mismatch of a few percent, transform spontaneously to three-dimensional (3D) islands (QDs) above a certain critical thickness, typically ~ 1.5 monolayers (MLs), to lessen the mismatch strain [135]. That is to say, the formation of 3D islands is driven by elastic strain relaxation. The overgrowing material can relax elastically expanding in vacuum, which gives rise to a significant energy advantage, i.e. the elastic energy is relaxed. On the other hand, the formation of islands causes an increase in the total surface area and surface energy of the system [136]. The formed islands, therefore, will ripen, initially, in order to reduce the total surface area covered by QDs. As all this mechanism occurs due to high lattice mismatch between the overgrowing material and underlying substrate, hence a minimum (but optimized) lattice mismatch is needed.

Chapter 5

Experimental Techniques and Analysis

5.1 The samples

The samples studied in this work were strain-engineered metamorphic InAs/In$_x$Ga$_{1-x}$As/GaAs QDs. They were grown [70] by MBE on semi-insulating (100) GaAs substrates. An In$_x$Ga$_{1-x}$As metamorphic lower confining layer (LCL) with In composition x and thickness d was deposited at 490 °C on top of a 100-nm thick GaAs buffer layer. The InAs QDs were grown with a 3.0 ML (monolayer) coverage by ALMBE at 460 °C after a growth interruption of 210 s to lower the substrate temperature, and capped with a 20-nm thick In$_x$Ga$_{1-x}$As upper confining layer (UCL) with the same composition as the LCL, also deposited by ALMBE at 360 °C (Fig. 1.2).

We have studied 46 such samples and 28 out of them, given in table 5.1, were found useful in terms of bright spectra for these samples; hence they were detected and analysed; the dat for rest of the samples were noisy and not analysable. Samples sizes were typically 2×2 mm^2 or 3×3 mm^2. The indium composition in these

Sample	x	d ($\mathring{A}$)	Γ (μeVT^{-2})	μ (m_0)	a_B (nm)
A	0.09	10000	13.75	-	-
B	0.12	1650	12.11	-	-
C	0.15	200	9.68	-	-
D	0.15	600	12.30	-	-
E	0.15	600	11.57	-	-
F	0.15	600	10.14	-	-
G	0.15	1200	11.99	-	-
H	0.15	2200	13.80	-	-
I	0.15	3600	13.64	-	-
J	0.18	310	14.04	-	-
K	0.20	5470	34.55	-	-
L	0.24	700	17.45	-	-
M	0.24	1450	38.23	-	-
N	0.28	280	11.46	-	-
O	0.28	370	21.40	-	-
P	0.28	600	14.69	-	-
Q	0.28	2200	69.76	0.08	16.83
R	0.28	2200	57.13	0.08	15.12
S	0.28	5000	72.22	0.10	18.42
T	0.31	600	29.15	0.09	11.25
U	0.31	2200	112.85	0.07	20.05
V	0.31	5000	158.76	0.07	22.64
W	0.31	10000	113.02	0.04	17.7
X	0.35	500	47.32	0.06	11.49
Y	0.35	600	44.13	0.06	11.27
Z	0.35	800	42.98	0.06	11.23
AB	0.35	2200	101.45	0.02	10.43
AC	0.35	5000	113.75	0.02	10.7

TABLE 5.1: List of analysed samples with respective input parameters: indium content in confining layers, x, and LCL thickness, d; and output parameters: diamagnetic shift coefficient, Γ, exciton reduced mass μ and Bohr radius of exciton, a_B.

samples varied from 0.09 to 0.35, while the LCL thickness varied from 100 $\mathring{A}$ to 10000 $\mathring{A}$.

The shape of the capped QDs has been assumed to be truncated cones according to a number of papers in the literature, as there are no experimental data on these QDs. The sizes of the QDs have been measured [70] by atomic force microscopy (AFM) (Fig. 5.1) on uncapped structures; their size are independent of LCL thicknesses and

LCL composition for $x < 0.35$, while their lateral sizes do depend on x for $x \geq 0.35$: they are 22 nm for ≤ 0.33 nm and 31 nm for $x = 0.35$
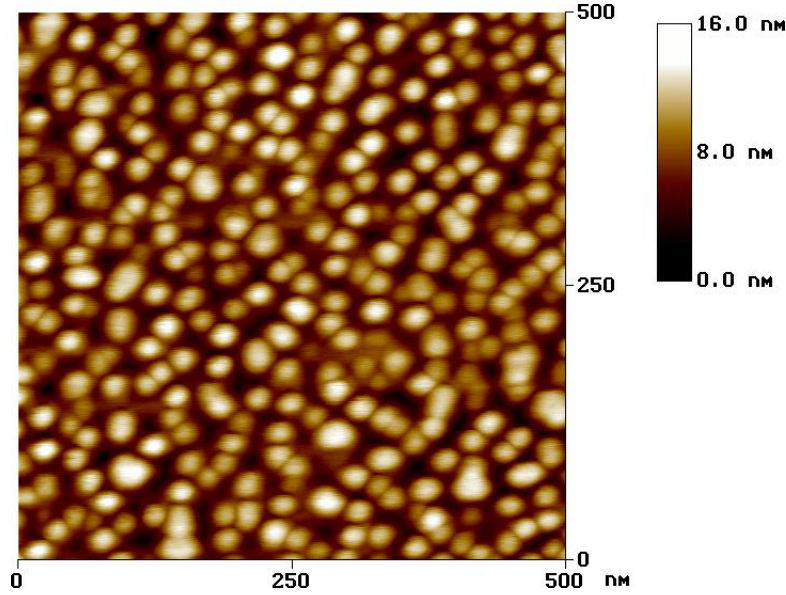
FIGURE 5.1: An AFM image of nominally 3.0 ML InAs QDs grown on 220-nm thick $In_xGa_{1-x}As$ MBs with $x = 0.15$. The image has been provided directly by Luca Seravalli, from Parma, Italy.

The nominal composition of the QDs is InAs: It is understood that the capping process may influence the dot morphology and composition, however it is expected that such effects would be substantially reduced in these structures due to the capping growth procedure (atomic layer MBE at relatively low temperature). Furthermore, Luca Seravalli (Parma, Italy), who provided the samples and took the AFM measurements, confirmed that the dot sizes measured by transmission electron microscopy (TEM) on capped structures are quite similar to those measured by AFM on uncapped ones.

The QD-LCL mismatch, which is a function of the In molar fraction x and thickness d of the InGaAs LCL, was calculated by following the model of Maree et al [137],

$$f = \frac{(a_{InAs} - a_{LCL})}{a_{LCL}} \ ,$$
(5.1)

where a_{LCL} and a_{InAs} are the lattice parameters of the partially relaxed $In_xGa_{1-x}As$ LCL and of the freestanding unstrained InAs, respectively. The parameter a_{LCL} is related to the in-plane residual strain as

$$\varepsilon = \frac{(a_{InGaAs} - a_{LCL})}{a_{LCL}} \quad , \tag{5.2}$$

which can be approximated by

$$\varepsilon = \varepsilon_0 \sqrt{\frac{d_c}{d}} \quad , \tag{5.3}$$

where

$$\varepsilon_0 = \frac{(a_{InGaAs} - a_{GaAs})}{a_{GaAs}} \quad , \tag{5.4}$$

is the strain of a pseudomorphic layer of $In_xGa_{1-x}As$ grown on (100) GaAs, applicable to thickness $d < d_c$, the critical thickness for which the pseudomorphic growth ($a_{InGaAs} = a_{GaAs}$) transforms to metamorphic (LCL strain starts relaxing as $d^{-1/2}$). a_{InGaAs} and a_{GaAs} are the unstrained $In_xGa_{1-x}As$ and GaAs lattice parameters, respectively.

5.2   Laboratory set-up

5.2.1   The Cryostat

The cryostat, manufactured by Oxford Instruments, was developed for experiments in a magnetic field of up to 17 T and at temperatures ranging from approximately 2 K to 400 K. A simplified representation is shown in Fig. 5.2. There is an outer vacuum space, surrounding a jacket of liquid nitrogen, cooled to 77 K, and an inner helium bath, where the superconducting solenoid magnet is located. The magnet is also from Oxford Instruments and is made of niobium-tin (Nb_3Sn), and produces magnetic fields up to 15 T at 4.2 K, but can be increased up to 17 T by cooling down to 2.2 K by reducing its surrounding liquid-helium temperature.
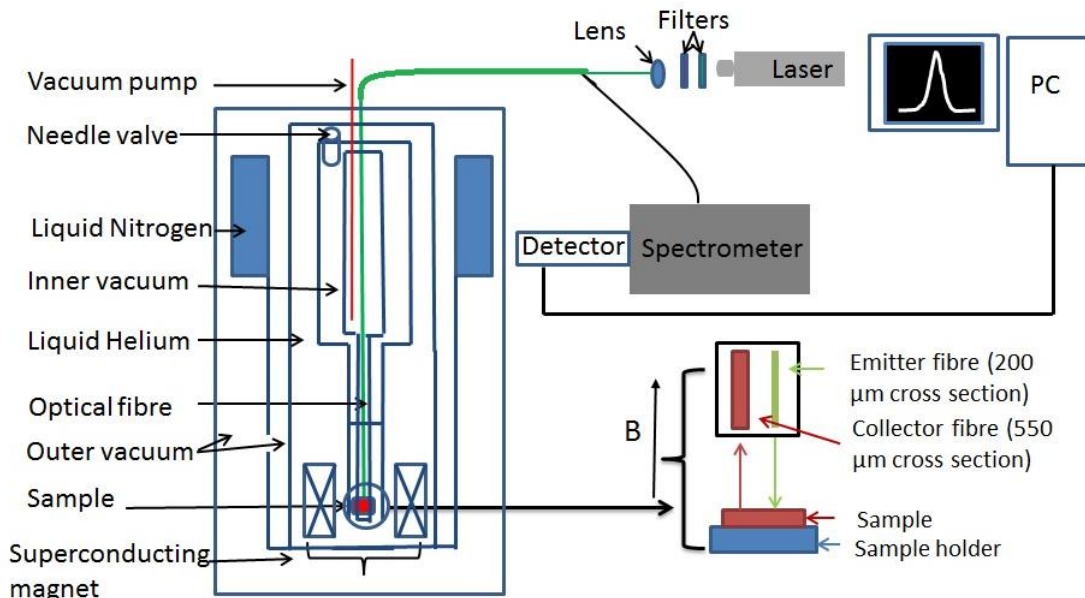
FIGURE 5.2: Schematics diagram of the laboratory set up showing the cryostat and optics connection.

A variable temperature insert (VTI) is inserted into the liquid helium in the cryostat that cools the superconducting magnet and controls the temperature of the sample. The inner vacuum space lies between the He bath and the sample. It allows large temperature differences between the two, in the most extreme case 2 K - 400 K. The VTI operates by drawing liquid helium through a needle valve. The liquid He passes through a heat exchanger into the sample space and is then pumped away by a room temperature vacuum pump. An integral heater and sensor on the heat exchanger allows the temperature to be set to any value. An additional thermometer on the sample stick is used to measure the sample temperature.

The temperature, the superconducting magnet and levels of nitrogen and helium, are all monitored by specific control units which are in turn connected to a computer for complete external control.

5.2.2 The Optics

The samples are glued on to a brass sample mount using Electrodag which is inserted into the sample space of the VTI, in the centre of the super-conducting magnet so that the magnetic field is parallel to the growth direction. Light is transmitted to and from the sample via an optical fibre bundle (Fig. 5.2), where each fibre is kept optically isolated from each other and from outside light by using heat-shrink sleeving. Light emission occurs from a frequency-doubled neodymium-doped yttrium aluminium garnet (Nd:YAG) solid state laser emitting at 532 nm. This light first passes through a 532-nm laser interface filter, then through one or none of four neutral-density filters which helps to control the excitation power upon the sample, and finally, through a lens for focussing into the optical fibre. The laser light emitting from silica core multimode optical fibre (Thorlabs BFL22-200) forms a spot on the sample with $\approx 2~mm$ diameter. Another silica core multimode optical fibre (Thorlabs BFL22-550) having a $\approx 0.5~mm$ diameter is used to collect the PL emission and to send it to a spectrometer.
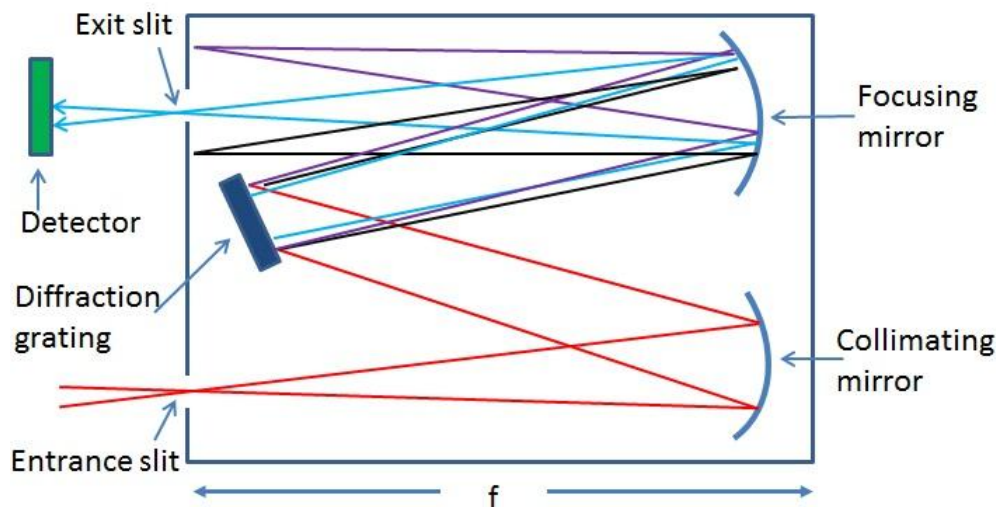
FIGURE 5.3: A schematic diagram of a spectrometer showing diffraction and detecting mechanism. The focal length is shown by f which is 30 cm.

A long pass filter at the spectrometer's entry slit filters out any 532 nm laser light,

reflected into the collection fibre. The spectrometer contains three different gratings; 150, 300 and 600 lines/mm, to give different wavelength resolutions when taking measurements. The spectrometer is of 30 cm focal length; combined with an Andor Technology Peltier-cooled 512 pixel InGaAs diode array with an operating wavelength of 600 to 1700 nm, to analyse the PL emission by digitizing it as a function of wavelength; and the results are received by the same computer that is used to control the temperature and magnetic field. The detector is cooled to -60 °C to reduce noise in the PL spectra.

The light is directed through a fiber optic cable into the spectrometer (Fig. 5.3) through an entrance slit, a narrow aperture. A concave mirror collimates the divergent light and directs it onto a grating. Then the spectral components of the light are dispersed at slightly varying angles by the grating, which is then focused by a second concave mirror and imaged onto the detector. There are options to set the spacing of the diffraction grating and to alter the wavelength it is centred upon. To avoid saturation and to get enough signal, an integration time can also be set in the computer.

Furthermore, taking the laser power density as $\sim 3 \times 10^3 \ mW/cm^2$, carrier's lifetime as ~ 1 ns, the dot density as $3 \times 10^{10} \ cm^2$, the average number of carriers per QD is calculated as 10^{-4}, i.e. $<< 1$.
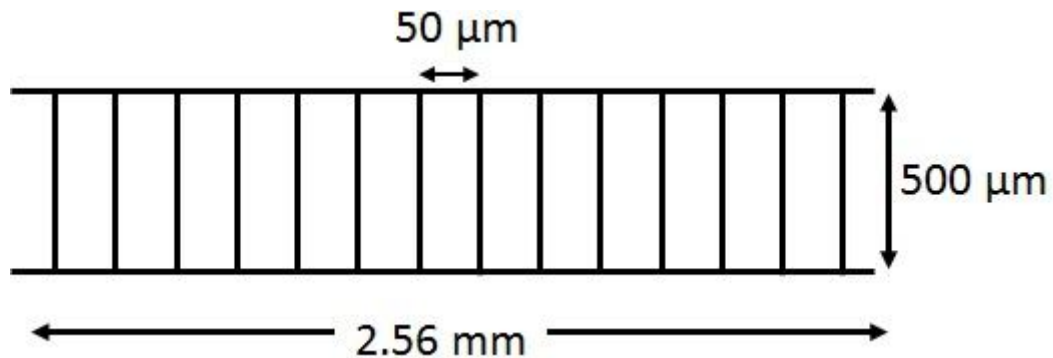
FIGURE 5.4: Schematic diagram of a multichannel InGaAs linear array detector where each element acts like a slit. It has 512 pixels and 600 to 1700 nm wavelength range.

In this work we used a multichannel InGaAs linear array (Fig. 5.4), so there is no exit slit on the spectrometer, but each element on the detector array acts like a slit. There are different gratings: 150, 300 and 600 grooves/μm used in conjunction with a slit width of 150 μm (0.15 mm). The dispersion is given by 1.35 nm/mm, therefore the resolution of the PL system can be calculated as $0.15 \times 1.35 = 0.202$ nm. The width and the height of the array are given by 2.56 mm and 500 μm, respectively.

For controlling the cryostat, recording and analysing data, a number of specially designed LabView (Laboratory Virtual Instrument Engineering Workbench) interfaces are used, which is commonly used for data acquisition, instrument control and industrial automation.

5.3 Data analysis methodology

For analysing the data, two software programs (MassFit and Origin 8) were used. The files, containing the data-points saved by LabView, were opened in MassFit representing the intensity of the PL versus wavelength (Fig. 5.5).
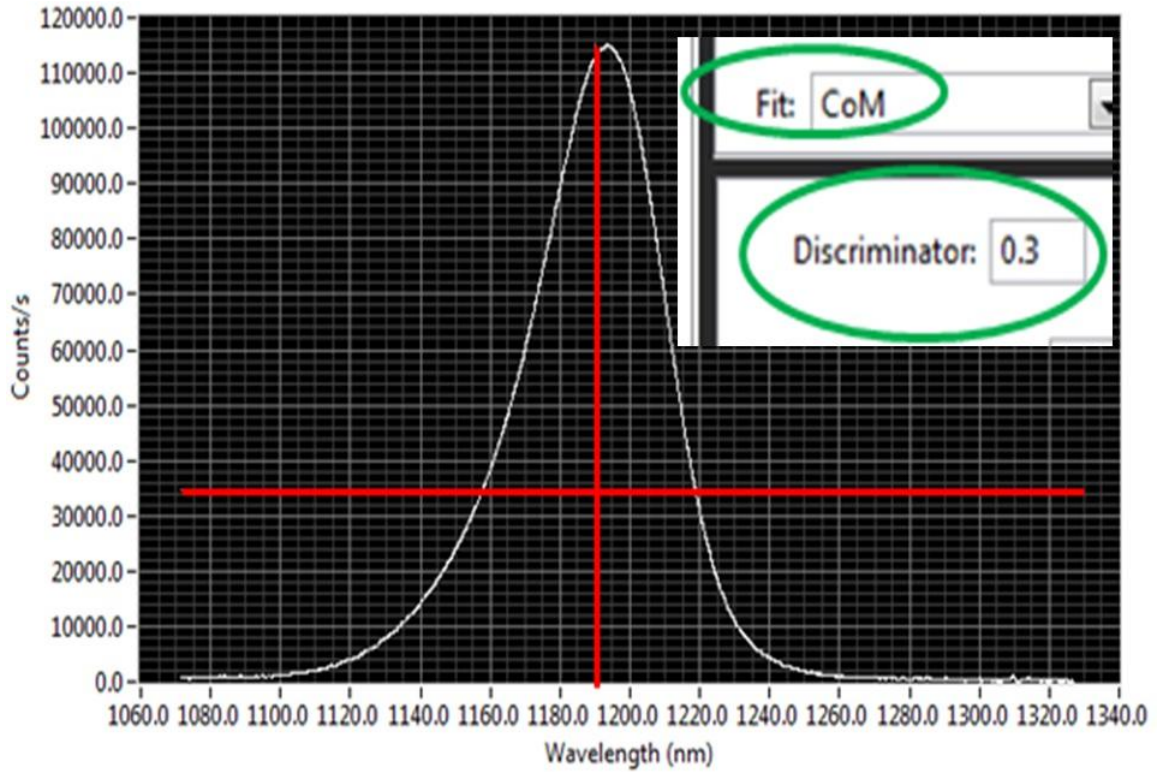
FIGURE 5.5: The PL spectra, at 4.2 K, representing the intensity vs wavelength. The red vertical and horizontal lines show the centre of mass (CoM) fit and discriminator, respectively. The two green circles have been shown to highlight the CoM and discriminator which can be changed by the user to take the average of various discriminators for accuracy of analysis.

The spectra were then fitted by selecting the centre of mass (CoM), given by $\frac{1}{M}\Sigma m_i r_i$ where $i = 1, 2....n$ and M, m_i, r_i are the sum of the intensities (integration) of all pixels, the intensity and position vector of the ith pixel, respectively (Fig. 5.6), to fit the spectra. A discriminator ranging from 10 % to 30 % was set up in order to cut-off the background.
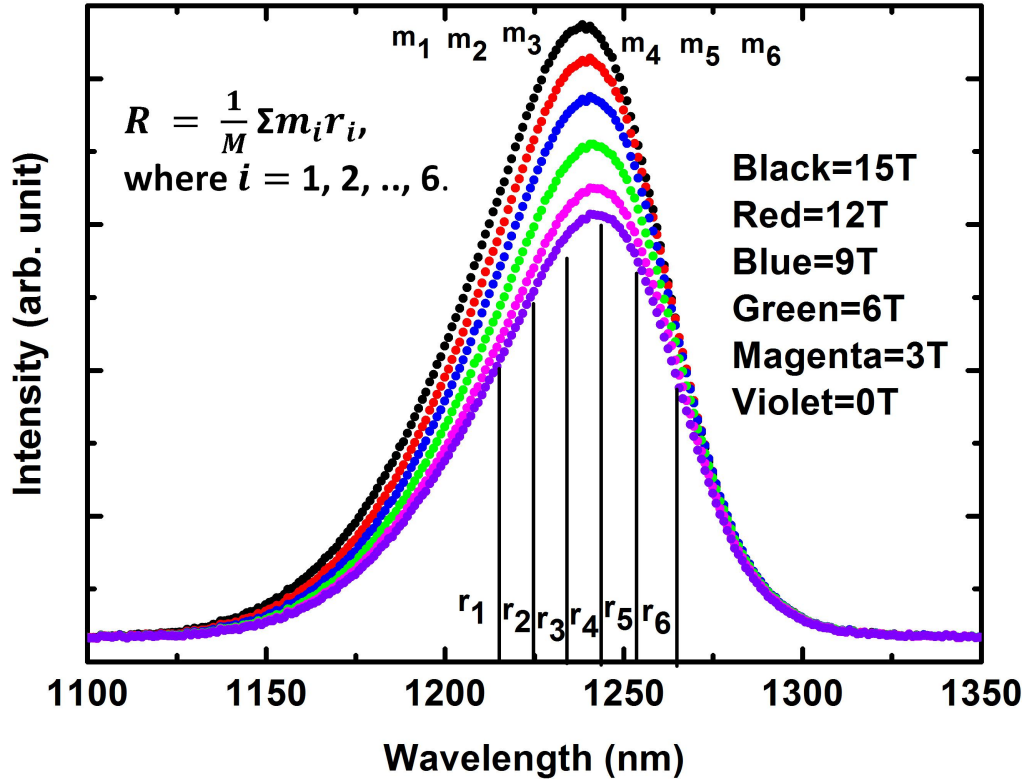
FIGURE 5.6: The calculation of centre of mass of the PL peak. There are different peaks, at 4.2 K, represented by different colours which correspond to different magnetic fields: black, red, blue, green, magenta and violet colours represent 15 T, 12 T, 9 T, 6 T, 3 T and 0 T magnetic fields, respectively.

The plot of E (eV) versus B (T) was plotted (Fig. 5.7) in MassFit. The plot file was opened in Origin 8 and the excitonic model (equations 2.30 and 2.31) was used for fitting to extract the parameters required for the determination of the exciton properties i.e., Bohr radius and exciton effective mass (Fig. 5.8).
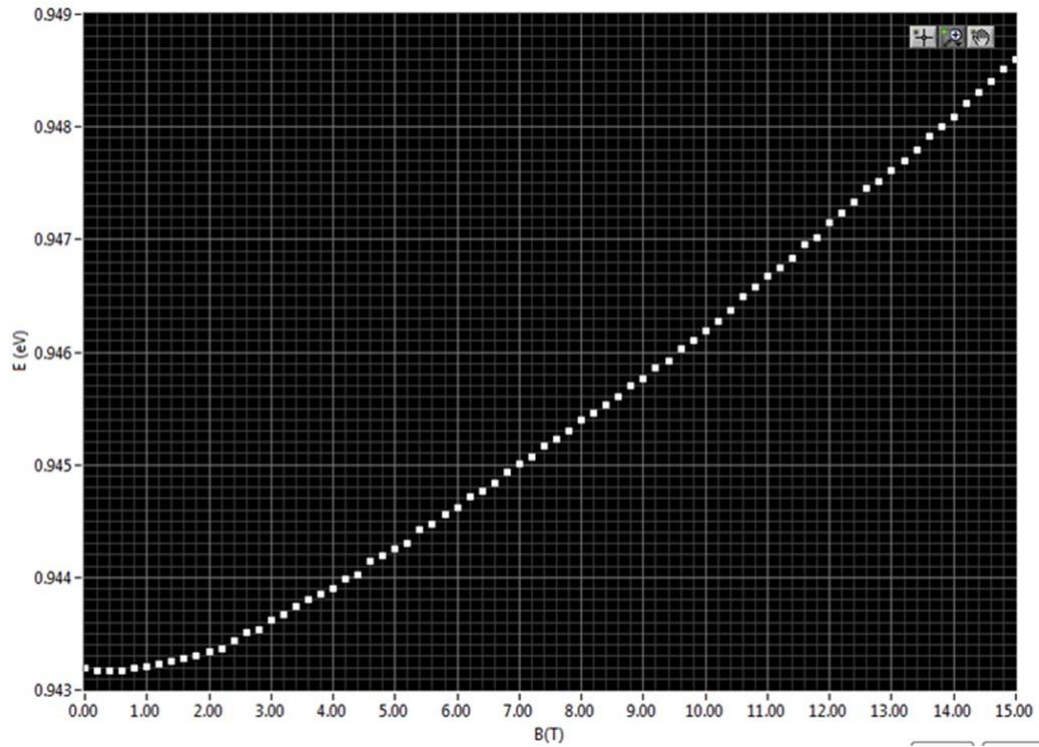
FIGURE 5.7: The plot of PL energy E (eV) versus magnetic field B (T), at 4.2 K, in MassFit.

We have measured each sample in both directions of magnet field sweeping, i.e. sweep-up, (0 - 15)T, and sweep-down, (15 - 0)T. To subtract the background, we used a discriminator describing the cut-off percentage, but it was noted that the centre of mass varies when changing the discriminator's value due to subtraction of different parts of the back-ground that causes the change in the values of the extracted parameters (Fig. 5.9).
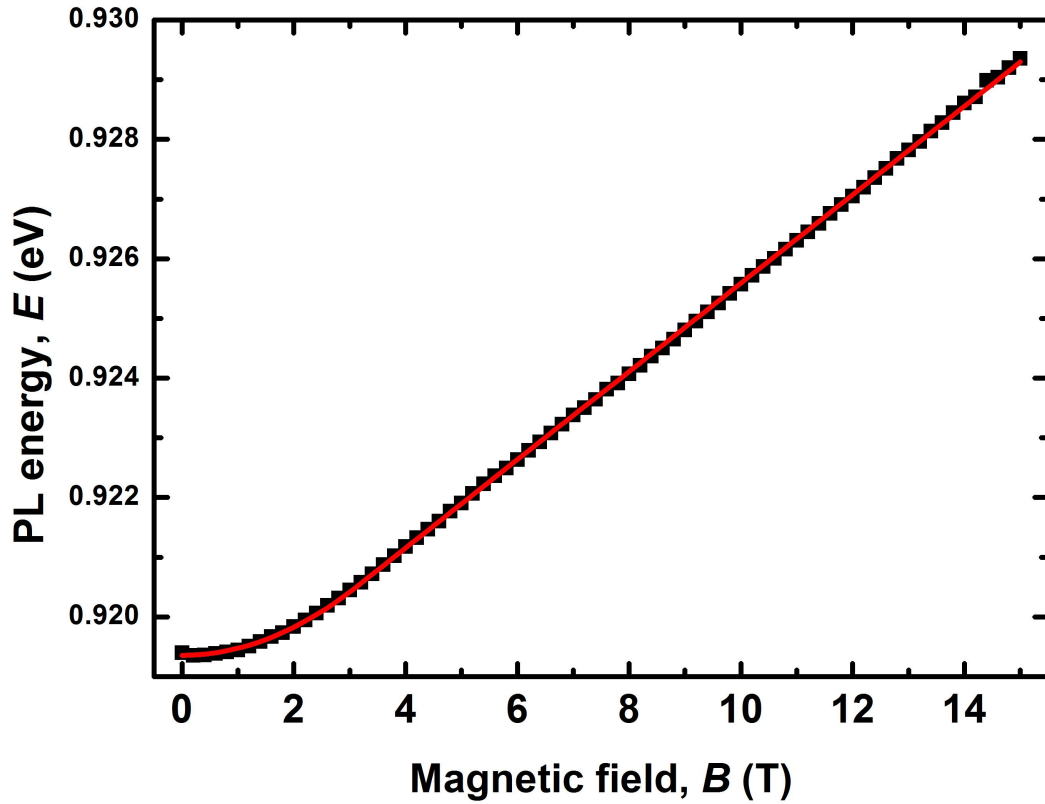
FIGURE 5.8: A plot of PL energy, E, versus magnetic field, B, at 4.2 K (in Origin 8), where the red line shows the user fitting.

To deal with this issue, a range of discriminators, i.e. (10%, 15%, 20%, 25%, 30%), were set and the average of the parameters, extracted from their corresponding discriminator-dependent spectra, was taken as shown in Table. 5.2, for instance, for the sample with indium composition = 0.28 and LCL thickness = 2200 $\mathring{A}$. This method was applied consistently to all samples.

Discriminator	Sweep up		Sweep down		Total average of $c(T)$	Total average of $b(\mu eVT^{-2})$
	c	b	c	b		
10% cut-off	6.22	53.5	6.1	54.07		
15% cut-off	6.2	54	6.14	54.19		
20% cut-off	5.97	56.2	5.95	56.07	**5.75±0.46**	**57.13±3.62**
25% cut-off	5.05	63.44	5.08	62.68		
30% cut-off	5.47	58.22	5.36	58.91		
Average	5.78	57.07	5.72	57.18		

TABLE 5.2: The table shows how output parameter values vary with changing the discriminator and magnetic field sweep direction. c and b are the critical magnetic field and diamagnetic shift coefficient, respectively.
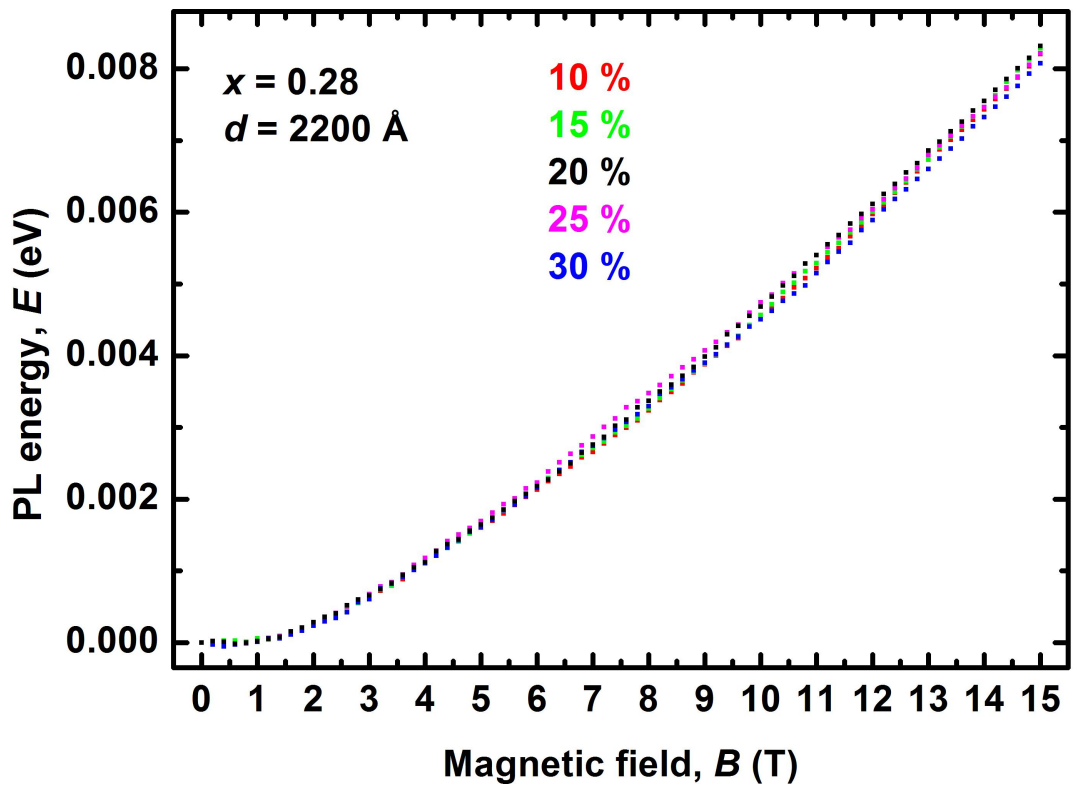
FIGURE 5.9: The PL energy, at 4.2 K, versus magnetic field for various discriminators showing the effect of discriminators on energy shifts. The red, green, black, magenta, and blue colours represent 10%, 15%, 20%, 25% and 30% cut-off, respectively.

Chapter 6

Results and Discussion: Zero Magnetic Field

In our samples, $InAs/In_xGa_{1-x}As/GaAs$ QDs, there are two input parameters: indium content in confining layers, x, and LCL thickness, d, that can be controlled independently. Any change in x changes the band offset between QD and confining layers and the QD-CL mismatch (or QD strain), while variation of d changes the mismatch only [138]. Fig. 6.1, reprinted from Ref. [82], shows the dependence of PL emission energy, at 10 K, calculated by effective-mass model, with parameters used from Ref. [78], on the QD-CL mismatch, f, and indium content in the confining layers, x. The dashed lines represent the pairs of (x, f) that cause room temperature emission wavelengths at 1.3, 1.4 and 1.5 μm. The figure shows that the PL emission energy decreases with decreasing mismatch and increasing indium content in the confining layers. Furthermore, the abrupt decrease in PL emission energy for $x > 0.33$, is related to the increase in the QD diameters, from 22 nm to 31 nm, which results in the deepening of the quantum-confined levels in the quantum potential well, hence reducing the PL energy.
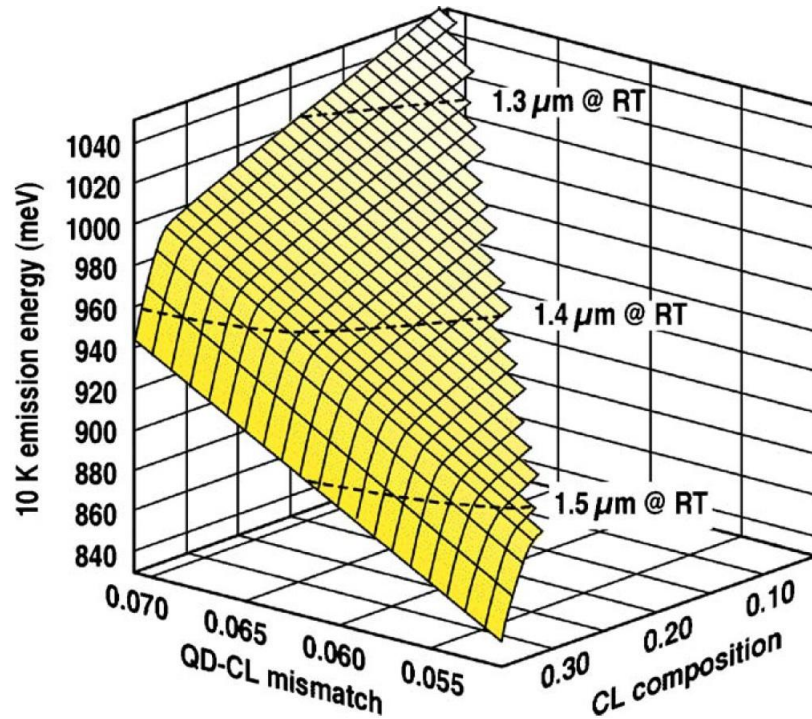
FIGURE 6.1: Reprinted with permission from Seravalli et al, APPLIED PHYSICS LETTERS 87, 063101 (2005) [138]. Copyright 2015, AIP publishing LLC. PL emission energy, calculated at 10 K, as a function of the QD-CL mismatch, f, and the indium content in the confining layers, x. The dashed lines represent the (x, f) pairs that result in RT emission wavelengths at 1.3, 1.4 and 1.5 μm.

In Fig. 6.2, the effect of changing indium content in the confining layers, x, on the band offset, E_{bo}, the energy difference between the conduction bands of InAs and $In_xGa_{1-x}As$, is schematically shown. (a) in the figure represents the case where the x is low, i.e, 0.15, which results in a large band offset, while the band offset in (b) is small due to high indium content in the confining layers (0.35).

In order to see the effect of each parameter, separately, on the zero-field energy (and wavelength), in our results, we are going to select a set of samples consisting of the same indium composition in the confining layers and varying LCL thickness, and another set of samples with the same LCL thickness and varying indium composition.
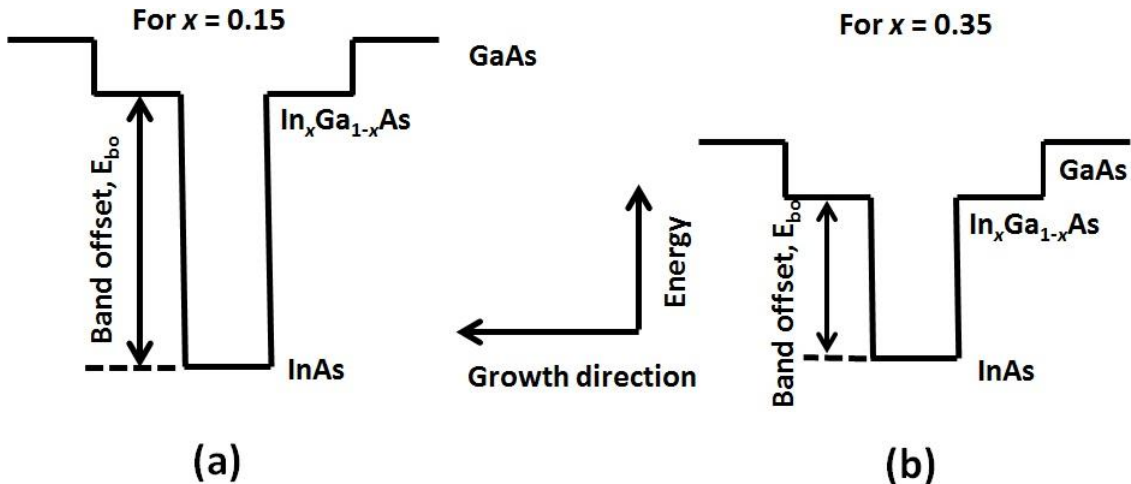
FIGURE 6.2: A typical conduction band diagram showing energy versus growth direction for two samples with different indium content in the confining layers. In case (a), the indium content, x, is low, 0.15, which results in a larger band offset, E_{bo}, than that for the case (b) where the indium content in confining layers, x, is high, i.e., 0.35.

We start by presenting our results obtained in zero magnetic field, at low temperature, 4.2 K: PL spectra showing the dependence of zero-field energy (wavelength), intensity and line-width on indium content in confining layers, x, and LCL thickness, d.

6.1 Dependence of zero-field PL spectra on indium content in the confining layers, x

The PL spectra presented in Fig. 6.3 show normalised spectra for a constant d [(a) 100 Å, (b) 600 Å, (c) 2200 Å and (d) 5000 Å], and different values of x. In Fig. 6.4(a), the corresponding zero-field PL emission energy versus x has been plotted for the same values of d. It can be seen in Figs. 6.3(b), (c) and (d) that the wavelength increases with increasing x for a constant d, but the increase in (a) is not significant. Similarly, the corresponding energies decrease with increasing x for a constant d, differentiated by different colors, as shown in Fig. 6.4(a), but for $d = 100$ Å, the

decrease is not prominent. This can be explained by looking into Fig. 6.4(b), where QD-CL mismatch, f, (detailed in the next chapter) has been plotted as a function of x for the mentioned values of d.
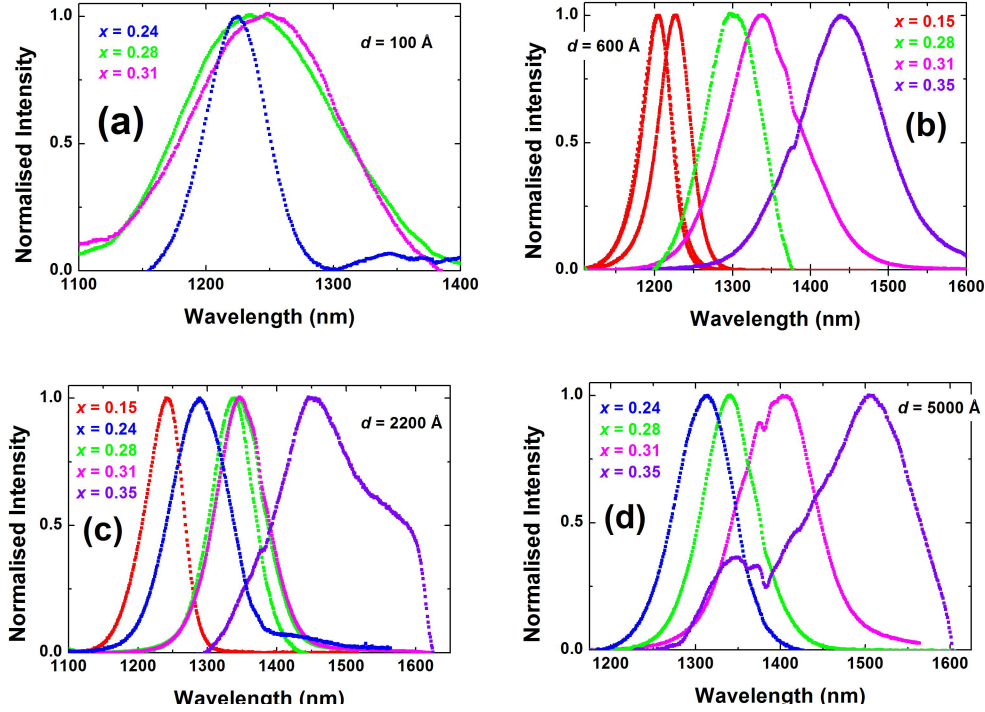
FIGURE 6.3: (a), (b), (c) and (d) show PL spectra, at 4.2 K, with changing x, differentiated by different colours, but constant d, 100 Å, 600 Å, 2200 Å and 5000 Å, respectively. It is clear that the wavelength increases with increasing x for a particular d.

It can be seen that QD-CL mismatch, hence the strain within the QD, decreases with increasing x. Thus, the increase in emission wavelength and the corresponding reduction in energy with increasing x are due to the reduction in strain. Furthermore, for $d = 100$ Å, in Fig. 6.3(a) and Fig. 6.4(a) the slight increase in wavelength and reduction in energy, respectively, are due to the fact that the QD-CL mismatch is also a function of d, in addition to x: the QD-CL mismatch and hence QD strain increases with decreasing thickness. This is discussed in more detail in the next section. For very lower thickness (100 Å), there is insufficient metamorphic growth

to significantly reduce the QD-CL mismatch with increasing x, and consequently the change in energy and wavelength is moderate.
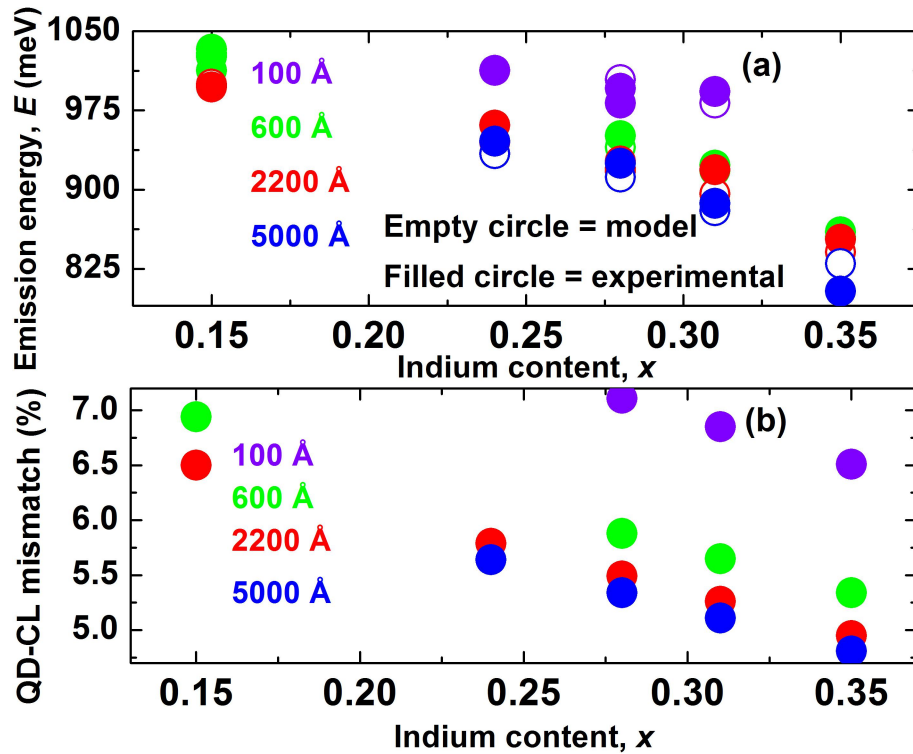
FIGURE 6.4: (a) Zero-field PL emission energy, at 4.2 K, as a function of indium content, x, for various LCL thickness, d, differentiated by different colours. The empty circles represent model data (provided by Seravalli from Parma, Italy), at 10 K, while the filled circles show the experimental values, at 4.2 K. (b) QD-CL mismatch, calculated by equation (5.1), versus x for the same values of d. Violet, green, red and blue colours show data for $x = 100$ Å, 600 Å, 2200 Å and 5000 Å respectively.

It should be noted that AFM measurements have shown [70] that for $x = 0.35$, the QD diameter becomes bigger (~ 31 nm), resulting in a lowering of the confinement levels of the carriers, therefore the PL energy reduces more than for other values of x. In Fig. 6.3(a), the spectra are broadened for $x = 0.28$ (green) and $x = 0.31$ (pink), possibly due to the contribution to the PL by broader distribution of dot sizes. Two samples (red) with same indium content in confining layers, $x = 0.15$, in Fig. 6.3(b) have slightly different wavelengths. There is a slight difference between the spectra

for the sample with $x = 0.28$ (green) and with $x = 0.31$ (pink) in Fig. 6.3(c). These difference may be due to small variations in growth conditions or non-uniformity across the wafer.

6.2 Dependence of zero-field PL spectra on LCL thickness, d

Fig. 6.5 shows PL spectra for various values of d, differentiated by different colours, and constant x [(a) 0.15, (b) 0.24, (c) 0.28, (d) 0.31 and (e) 0.35], while Fig. 6.6(a) shows zero-field PL emission energy as a function of LCL thickness, d, for the same values of x. The calculated energies [70], represented by squares, are at 10 K while the experimental ones, indicated by circles, are at 4.2 K. It can be seen in Fig. 6.5 that the wavelength increases with increasing d for a particular x, ranging from 0.15 to 0.31, but for $x = 0.35$ in (e), the change is not significant. Similarly Fig. 6.6(a) shows that for indium content ranging from 0.15 to 0.31, the energy decreases faster with increasing d at lower values, i.e. $\sim (200 - 700)\mathring{A}$, but at larger thickness ($>$ 700 $\mathring{A}$), the decrease reduces. For $x = 0.35$, there is no significant reduction in the energy with increasing d. This can be explained by looking into Fig. 6.6(b) where the reduction in QD-CL mismatch (hence QD strain) is faster for lower values of d, $\sim (200 - 700)\mathring{A}$, but afterwards, it slows down. The increase in wavelength emission, shown in (a), (b), (c) and (d) of Fig. 6.5 and the consequent reduction in the energy with increasing d for a particular x, ranging from 0.15 to 0.31, in Fig. 6.6(a) are due to the reduction in QD-CL mismatch (QD strain) from metamorphic growth, while the QD size remains constant due to invariance in x. For $x = 0.35$, the QD-CL mismatch changes by just 0.53 % (from 5.34 % to 4.81 %) with increasing d while going from 600 $\mathring{A}$ to 5000 $\mathring{A}$. The wavelength (Fig. 6.5(e)) and the corresponding energy (Fig. 6.6(a)), therefore, does not change significantly with increasing d (600 $\mathring{A}$ to 2200 $\mathring{A}$).
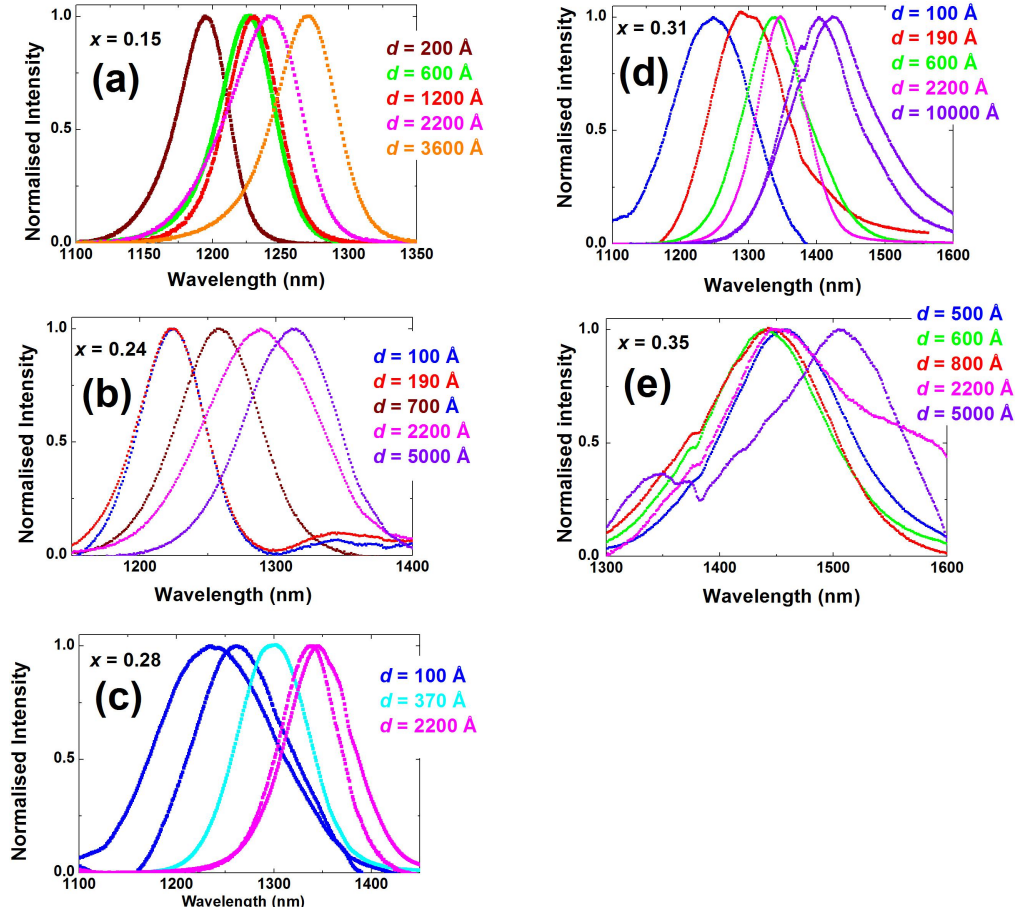
FIGURE 6.5: (a), (b), (c), (d) and (e) show the PL spectra, at 4.2 K, for various d, differentiated by different colours, and constant x, 0.15, 0.24, 0.28, 0.31 and 0.35 respectively. For any particular x, an increase in wavelength with increasing d is seen.

However, for $d = 5000$ Å in Fig. 6.5(e), the increase in wavelength is noticeable, unlike for the other lower values of d. This can be attributed to the maximum relaxation of the LCL, when d is at its largest value (5000 Å). A similar trend has been evidenced by Seravalli and his co-workers [78], where they concluded that d could be another effective parameter, in addition to x, that can be used to redshift the emission wavelength.
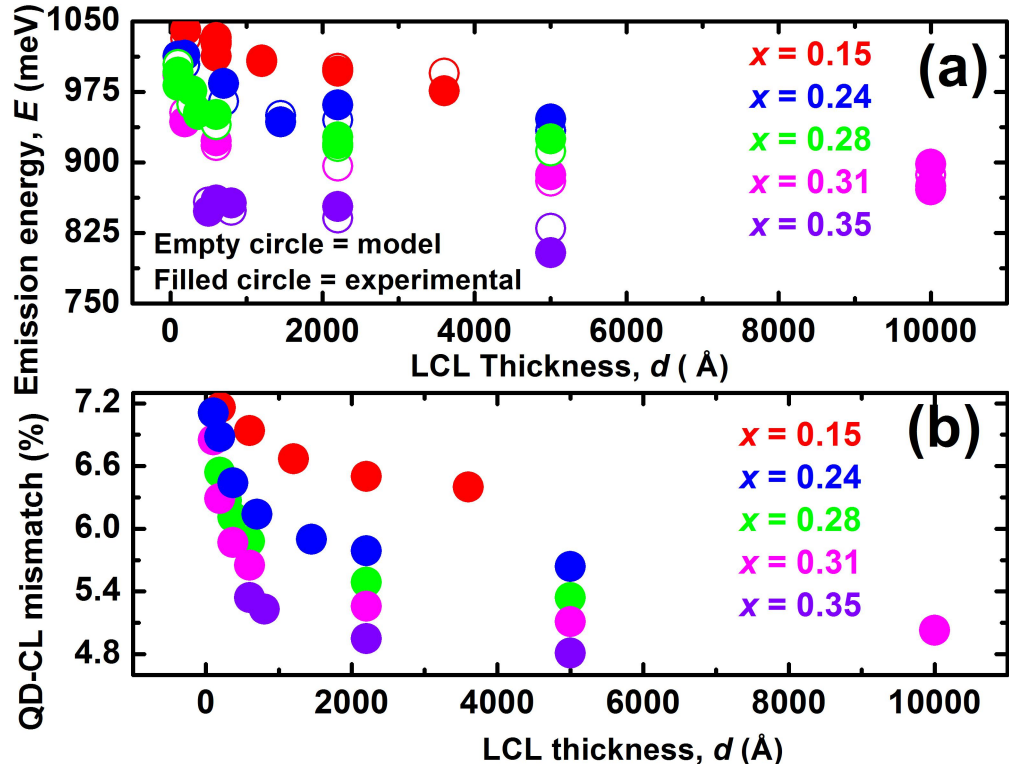
FIGURE 6.6: (a) Zero-field PL emission energy as a function of LCL thickness, d; the empty circles and filled circles represent the model, at 10 K, and experimental, at 4.2 K, data respectively. The data from the model calculation were provided by Seravalli from Parma, Italy. (b) QD-CL mismatch, calculated by equation (5.1), for various indium contents in the confining layers, x, as a function of LCL thickness, d. Red, blue, green, magenta and violet colours, in (a) and (b), represent data for $x = 0.15, 0.24, 0.28, 0.31$ and 0.35, respectively.

The spectra for $d = 600\text{Å}$ (green) and $d = 1200\text{Å}$ (red) in (a) and for $d = 100\text{Å}$ (blue) and $d = 190\text{Å}$ (red) in (b) of Fig. 6.5 overlap, almost, which indicates a very slight shift in wavelength with increasing LCL thickness from 600 Å to 1200 Å in (a) and from 100 Å to 190 Å in (b). Furthermore, samples with similar LCL thickness, two with $d = 2200\text{Å}$ (magenta) in (c) and two with $d = 10000\text{Å}$ (violet) in (d), have spectra with different wavelengths. As commented above, these variations can be due to small variations in growth conditions or non-uniformity across the wafer.

6.3 Dependence of PL intensity and line-width on indium content in the confining layers, x, and LCL thickness, d

Fig. 6.7 shows PL spectra for varying x, differentiated by different colours, and constant d, i.e. (a) 100 Å, (b) 600 Å, (c) 2200 Å and (d) 5000 Å. In the same way, PL spectra for varying d and constant x, 0.15, 0.24, 0.28 and 0.35, are shown in Fig. 6.8(a), (b), (c) and (d), respectively.
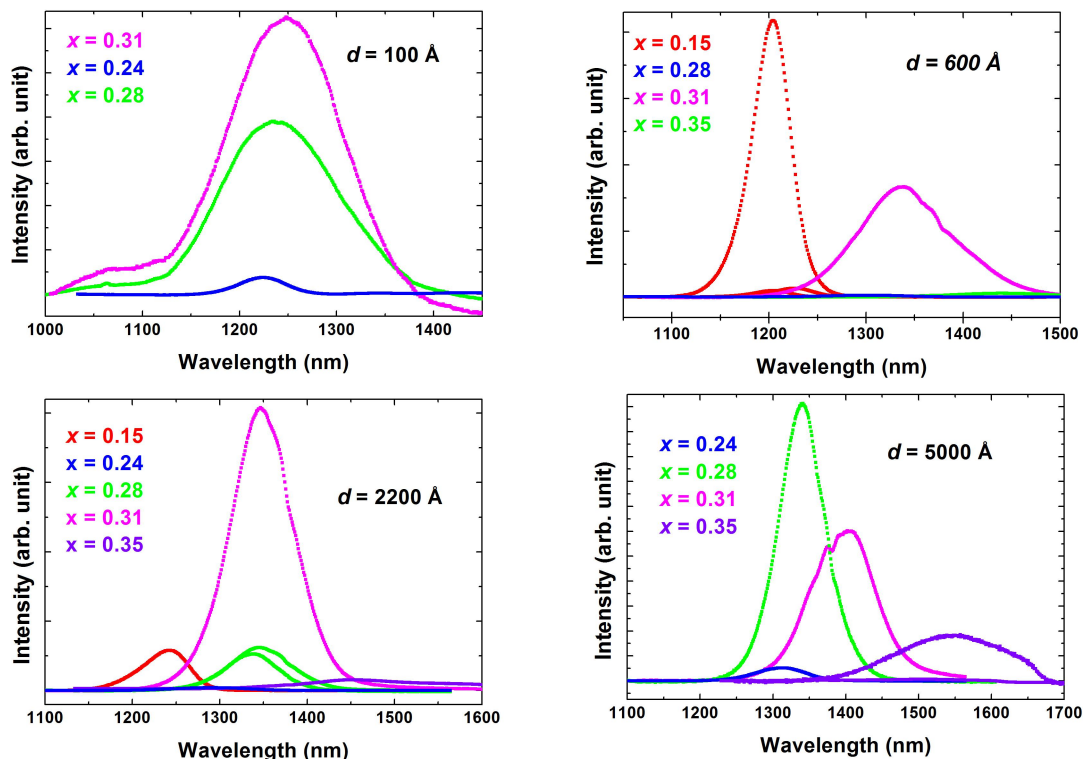
FIGURE 6.7: PL intensities, at 4.2 K, for various indium content in confining layers, x, differentiated by different colours, and constant LCL thickness, d, (a) 100 Å, (b) 600 Å, (c) 2200 Å and (d) 5000 Å.

There seems no correlation between intensity and x or d in Fig. 6.7 and Fig. 6.8, respectively. This can be understood by considering the various contributory factors such as experimental conditions and quality of the samples. The distance between

the fibre, containing the incident laser beam, and the sample position, its alignment and laser power likely varied across the samples. Furthermore, the experiments were carried out over a large span of time. Similarly, the quality of sample may be changing: sample with more dislocations, e.g. from the metamorphic growth, for instance, will give lower intensity than those with less dislocations.
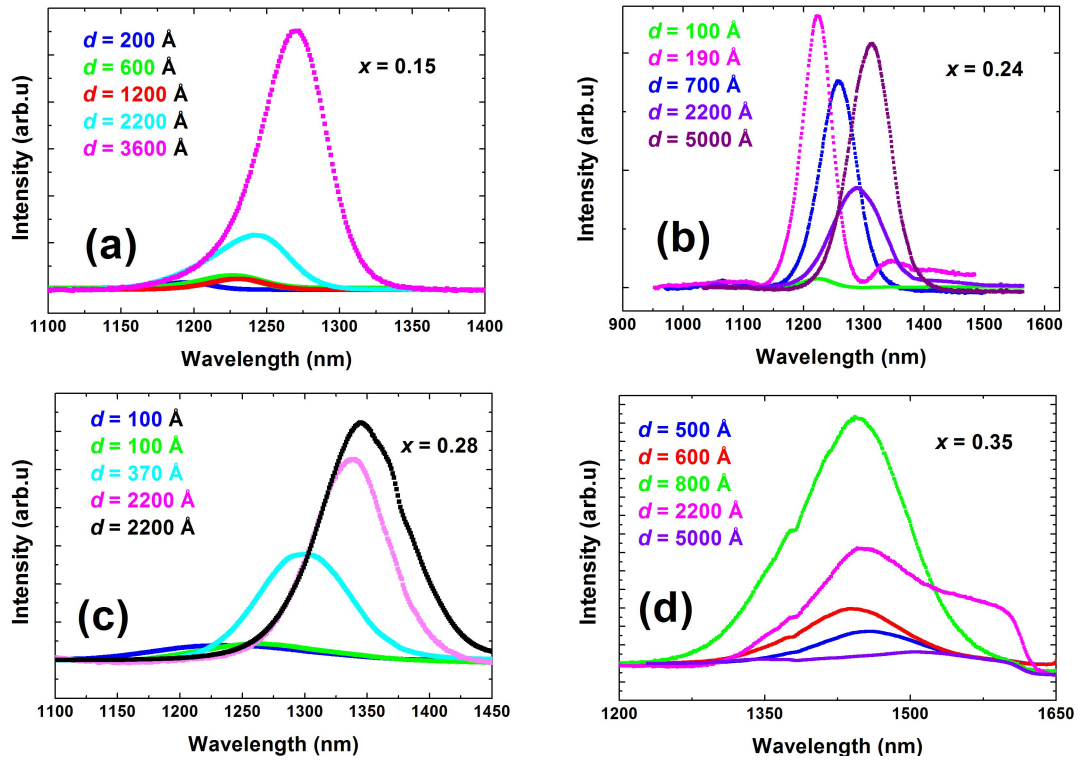
FIGURE 6.8: PL intensities, at 4.2 K, for various LCL thickness, d, differentiated by different colours, and constant indium content in the confining layers, (a) 0.15, (b) 0.24, (c) 0.28 and (d) 0.35.

Fig. 6.9 describes the line-width or full width at half-maximum (FWHM) as a function of indium content in the confining layers, x, and LCL thickness, d. The sizes of bubbles represent the values of line-width in nm. For a sample with $x = 0.24$ and $d = 100$ Å, the line-width $= 53.76$ nm: the values for other samples are proportionally larger or smaller relative to the bubble diameter. The FWHM gives an idea of the size distribution of the particles: a narrower quantum dot nano-crystal size distribution corresponds to a smaller FWHM. In the figure, it can be seen that

the line-width changes across the samples but no monotonic trend is observed. This implies that there is no correlation between the line-width and the parameters: indium content in the confining layers, x, and LCL thickness, d, although the samples with high LCL indium content, and hence LCL-substrate mismatch tend to have the largest line-widths.
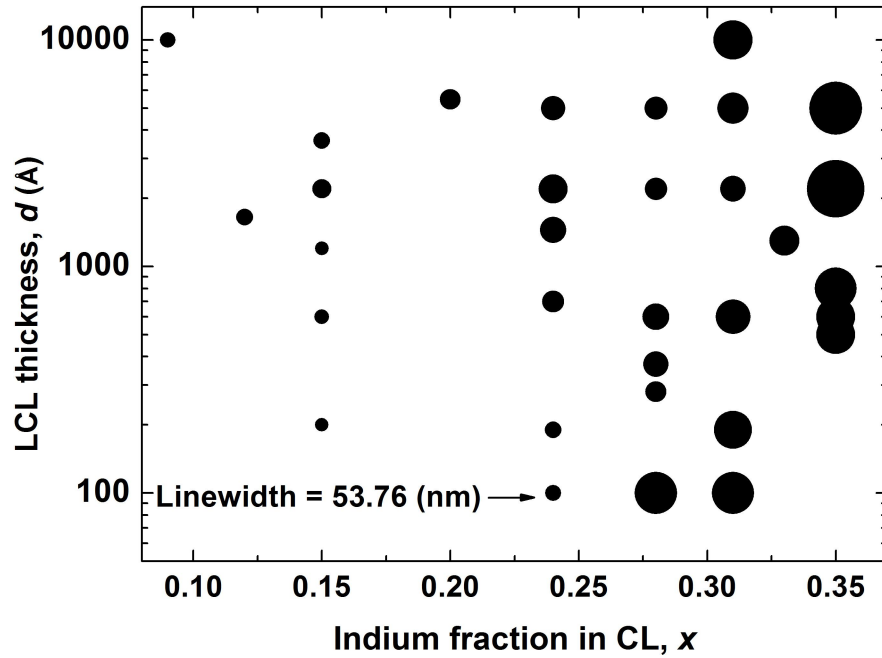
FIGURE 6.9: PL line width, at 4.2 K, represented by sizes of bubbles, as a function of indium content in the confining layers, x, and LCL thickness, d. For the sample with $x = 0.24$ and $d = 100$ Å, the line-width $= 53.76$ nm: the values for other samples are proportionally larger or smaller relative to the bubble diameter.

6.4 Conclusion

In conclusion, the dependence of PL spectra (wavelength) and energy, PL intensity and line-width on input parameters, indium content in confining layers, x, and LCL thickness, d, in zero-magnetic field at low temperature, 4.2 K, was studied. It was evidenced that the wavelength (PL energy) increases (decreases) with increasing x, for a particular value of d, and with increasing d, for a particular value of x. This

was attributed to the strain relaxation due to both increasing x and d. A correlation, however, between intensity and x or d was not found which was explained by taking into account a number of reasons: variance in quality (dislocations) of samples, distance between fibre and sample position plus its alignment, and change in laser power. Similarly, the line-width was observed to be changing across the samples but there was no monotonic trend, implying that there is no correlation between line-width and the parameters, x or d.

Chapter 7

Results and Discussion: Magneto-photoluminescence

Having discussed the dependence of the zero-field energy and wavelength on x and d, and the relation between intensity or line-width and x or d, we are now going to discuss our results based on the experiments carried out in magnetic field (0 - 15)T at low temperature, 4.2 K. It may be noted that the available magnetic fields, (0 - 15)T, in our laboratory is somewhat arbitrary: they are enough for some samples to reach the high-field regime, while for others they are not. For samples where the high-field regime is not reached, the critical magnetic field, B_c, at which the the PL energy shifts from parabolic to linear, is not determined. We, therefore, are not able to determine, for these samples, the exciton reduced mass, μ, and exciton Bohr radius, a_B. We select two samples in Fig. 7.1 to show how the PL spectra in magnetic fields (0 - 15)T at low temperature, 4.2 K, look and how the PL energy shifts with increasing magnetic field, for both cases: the case where the high-field regime is reached and the case where it is not. (a) and (b) in Fig. 7.1 show typical spectra for two samples, U and D with parameters $x = 0.31$ and $d = 2200\mathring{A}$; $x = 0.15$ and $d = 600\mathring{A}$, respectively. The different colours correspond to different magnetic

fields: black, red, blue, green, magenta and violet colours represent 15 T, 12 T, 9 T, 6 T, 3 T and 0 T magnetic fields, respectively.
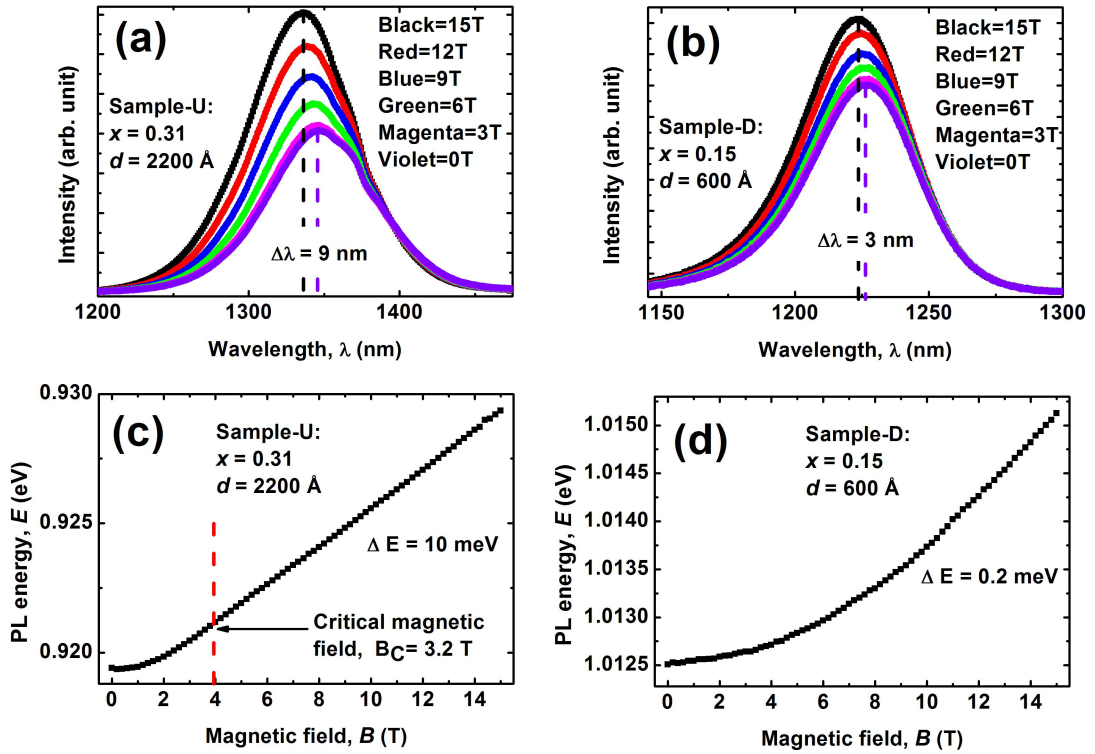
FIGURE 7.1: (a) and (b) describe the PL spectra in magnetic fields (0 - 15)T, at low temperature 4.2 K for two samples, U with parameters $x = 0.31$ and $d = 2200\mathring{A}$; and D with parameters $x = 0.15$ and $d = 600\mathring{A}$, respectively. The different colours correspond to different magnetic fields: black, red, blue, green, magenta and violet colours represent 15 T, 12 T, 9 T, 6 T, 3 T and 0 T magnetic fields, respectively. The separation between violet and black vertical dashed lines show the shift in wavelength, $\Delta\lambda$, due to sweeping of magnetic field from 0 to 15 T. (c) and (d) describe the PL energy as a function of magnetic field, at 4.2 K, for the samples U and D, respectively. For sample U (c), the critical magnetic field, B_c, the field at which the PL energy shifts from parabolic to linear, represented by red vertical dashed line, is 3.2 T and thus the high-field regime is reached, while for sample D (d), the PL energy remains parabolic: high-field regime is not reached.

(c) and (d) in the figure shows PL energy, E, as a function of magnetic field, B, for samples U and D, respectively. (c) describes the case where the high-field regime

is reached: the PL energy shifts from parabolic to linear at critical magnetic field, $B_c = 3.2$ T while (d) represents the case where the high-field regime is not reached. It can be seen for sample U in (a) that the change in wavelength with magnetic field sweeping from 0 to 15 T is 9 nm, larger than that for the sample D in (b), which is 3 nm. Similarly, it can be noted that for the sample U the energy shift, ΔE, with increasing magnetic field from 0 to 15 T (c) is 10 meV, larger than that for D in (d), which is just 0.2 meV. This shows that for the sample U, the magnetic length becomes smaller than the exiton Bohr radius and magnetic confinement dominates the spatial one and the high-field regime is reached, while for sample D, the magnetic length is larger than the exciton Bohr radius and the magnetic field does nothing more than just perturbing the exciton wave-function and the high-field regime is not reached.

We start with a brief discussion of reduced mass and Bohr radius of the exciton for a subset of samples for which the high-field regime is reached.

7.1   Reduced mass and Bohr radius

Fig. 7.2(a) shows the exciton reduced mass, μ, in units of m_0 (free electron mass) as a function of QD-CL mismatch for the samples whose energy shift reaches the high-field regime. The samples labelled as W, V, U, S, Q and R, whose parameters are given in table-(7.1), are of particular interest and will be labelled throughout the chapter. It is clear from the figure that the reduced mass increases approximately linearly at a rate of 0.10 ($\pm$ 0.02) m_0 per % change in mismatch for mismatches ranging from 4.8 % to 5.7 %. This is a very interesting result. A dependence of the effective mass on the QD strain (mismatch) is consistent with the theory reported in the literature [139, 140], although it is rarely commented upon and it is not clear that the dependence should be linear. We hope that this result will stimulate further theoretical investigation.

Sample	x	d (Å)	μ (m_0)	a_B (nm)
Q	0.28	2200	16.85	0.08
R	0.28	2200	15.11	0.08
S	0.28	5000	18.45	0.06
U	0.31	2200	20.05	0.07
V	0.31	5000	22.63	0.07
W	0.31	10000	17.72	0.04

TABLE 7.1: Input parameters, x and d, as well as output parameters: exciton reduced mass, μ, and its Bohr radius, a_B, for the samples of particular interest, i.e., Q, R, S, U, V and W.
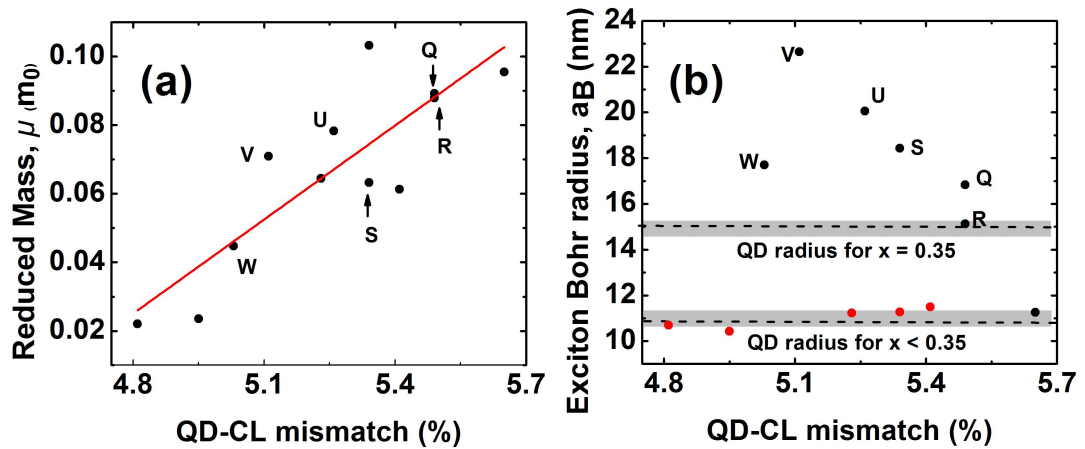
FIGURE 7.2: (a) Reduced mass, μ, of the exciton versus QD-CL mismatch, at 4.2 K, shows a linear relationship. The red line is a linear fit for all mismatches for which μ could be determined. In contrast, the exciton Bohr radius, at 4.2 K, (b) shows no correlation with mismatch. The upper dashed horizontal line shows the Bohr radius for samples with $x = 0.35$ while the Bohr radius for samples with $x < 0.35$ is represented by lower horizontal dashed line. We were able to find the reduced mass of exciton and its Bohr radius only for the samples for which the energy shift reaches the high-field limit. The six samples with $a_B > 14$ nm given labels W, V, U, S, Q and R are of particular interest, and will be labelled throughout the chapter. The red samples are for $x = 0.35$

Fig. 7.3 shows that the exciton reduced mass, μ, increases, more or less, with increasing QD PL energy, E_{PL}. This is expected from the variation of the mass with band gap energy, E_g, for bulk semiconductors: a smaller lattice constant results in a larger mass. Similarly, the smaller lattice constant of quantum dot, which in turn is due to strain (mismatch) in the quantum dot, causes the reduced mass of the exciton to be larger.
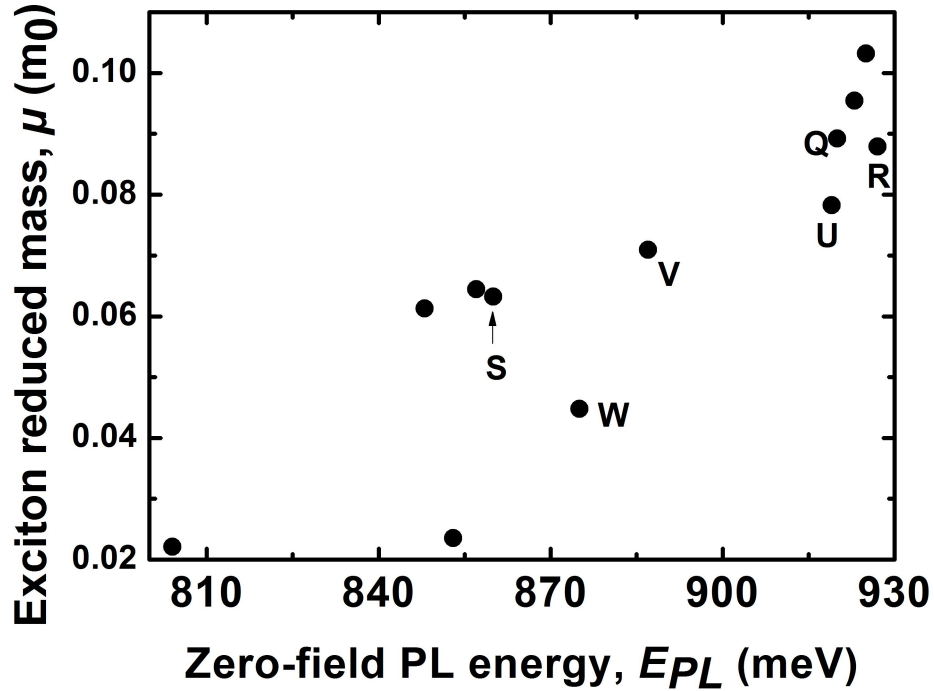
FIGURE 7.3: Exciton reduced mass, μ, at 4.2 K, as a function of QD zero-field PL energy, E_{PL}.

In order to look into the dependence of μ on residual strain in the LCL (partially relaxed), we establish a correlation between QD-CL mismatch (or QD-strain), f, calculated by equation (5.1), and residual strain in the LCL, ε. By substituting the value of a_{LCL} from Eqn-4.2 into Eqn-4.1 and rearranging, we get

$$f = \frac{a_{InAs}(\varepsilon + 1) - a_{InGaAs}}{a_{InGaAs}} \quad . \tag{7.1}$$

This shows that for a constant indium composition in the confining layers, the QD-CL mismatch, f, is directly proportional to the residual strain in the LCL, ε. This

can also be seen in Fig. 7.4, where ε, calculated according to Eqns-4.2 to 4.4, has been plotted versus f, calculated by Eqn-4.1. It shows that ε increases linearly with increasing f for a constant indium content in the confining layers, i.e., 0.35, 0.31 and 0.28 indicated by blue, red and black colours, respectively.
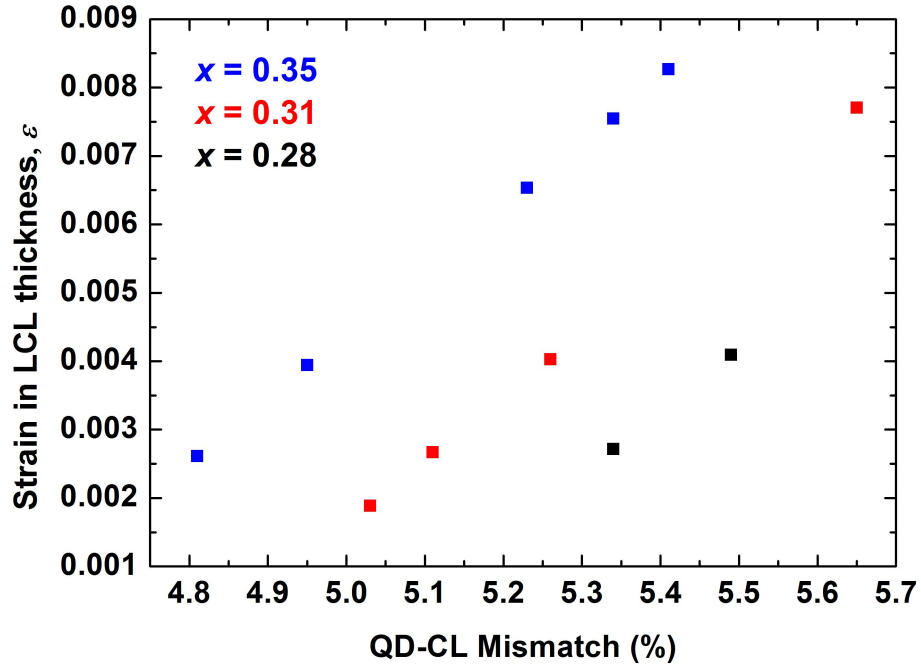
FIGURE 7.4: Residual strain in the LCL (partially relaxed), ε, as a function of QD-CL mismatch, f, for different but the constant indium composition in confining layers, i.e., 0.35, 0.31 and 0.28 indicated by blue, red and black colours respectively. The QD-CL mismatch and the residual strain in the LCL were calculated according to equations (5.1) and (5.2), respectively. The strain in the LCL increases linearly with increasing QD-CL mismatch.

The linear proportionality between f and ε implies that μ should also depend linearly on ε, as we have found it does on f (Fig. 7.2(a)). We therefore plot μ versus ε in Fig. 7.5. The data look scattered and no clear trend is seen, apparently, but we notice that there are various indium composition in the confining layers and the data has not been differentiated accordingly. Another and similar graph, therefore, is needed where the data is marked for different but constant indium composition in the confining layers.
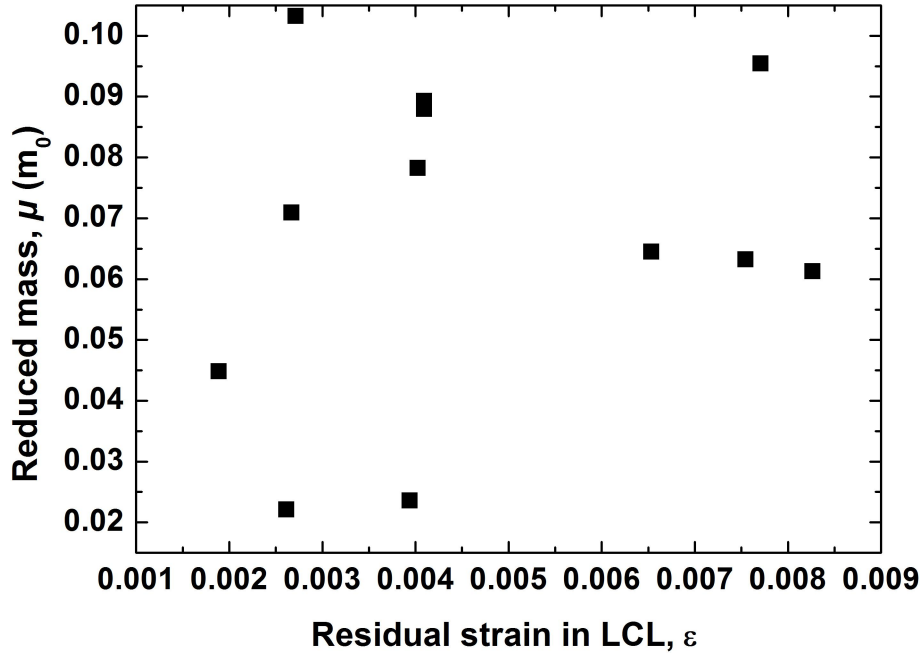
FIGURE 7.5: (a) Exciton reduced mass, μ, at 4.2 K, versus residual strain in the LCL, ε. No clear trend is seen, apparently.

Thus in Fig. 7.6, μ has been plotted versus ε for various but constant indium compositions, 0.35, 0.31 and 0.28, indicated by blue, red and black colours respectively. It can be seen that, as expected, μ also increases, overall, with increasing ε for a particular indium composition.

As commented above, although it is not unexpected that μ should increase with increasing strain, which is known to distort the band structure, the apparently linear relationship between μ and QD-CL mismatch (or even LCL strain) is quite remarkable, and would benefit from further theoretical investigation, which is well beyond the scope of this work.

In contrast, there is no correlation between QD-CL mismatch and exciton Bohr radius for QD-CL mismatch, 4.8 % $<f<$ 5.7 % as is evident from 7.2(b). At high mismatch (for $f >$ 5.7 %), we are unable to reach the high-field regime, meaning that the Bohr radius is less than 10 nm. Furthermore, since the minimum Bohr radius is somewhat arbitrary, i.e. depends on the magnetic field available in the experiment, and the

diamagnetic shift tends to decrease with increasing strain at higher mismatches (see next section), one might speculate that the behaviour observed in Fig. 7.2 continues at higher values of QD-CL mismatch. When the mismatch is high ($> 5.7\,\%$), then μ is large, possibly reducing a_B below the dot size ($a_B^2 \propto \frac{1}{\mu}$), but we can not demonstrate this.
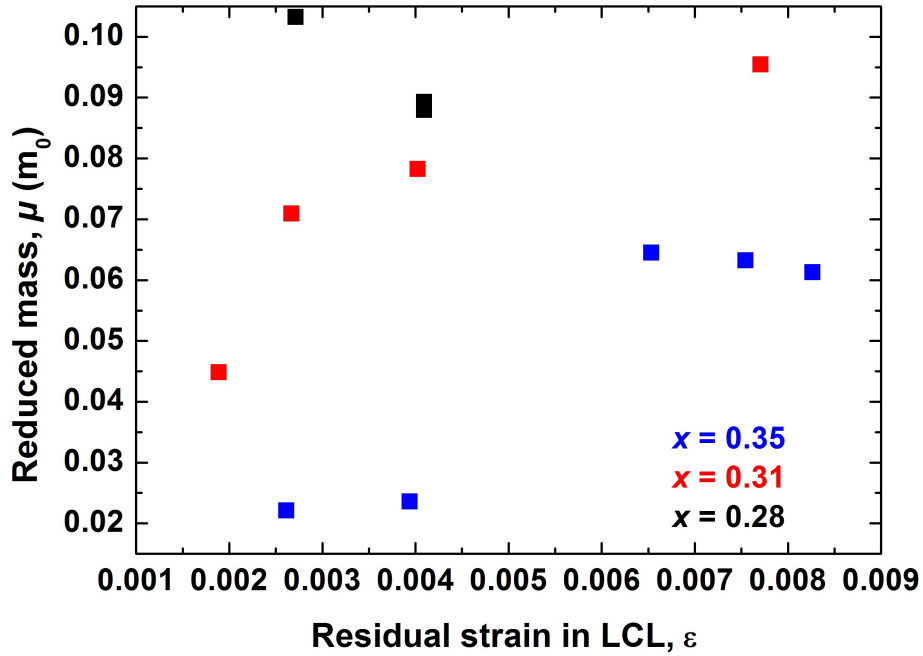
FIGURE 7.6: (a) Exciton reduced mass, μ, at 4.2 K, versus residual strain in the LCL, ε, for various but constant indium compositions, .i.e, 0.35, 0.31 and 0.28 indicated by blue, red and black colours, respectively.

When the mismatch is low ($< 5.7\,\%$), then μ is smaller and a_B is limited by the dot size (the cluster of points below $a_B = 12$ nm), or the confinement is weak and there is significant wave-function leakage out of the dot and a_B is large. In order to follow the 'progress' of the six samples which seems to show significant wave function leakage ($a_B > 14$ nm) we have labelled them A to F in 7.2(b) and in the following figures. It is also interesting to note in 7.2(b) that there seems to be an empty regime between samples where $a_B \sim$ dot radius and those with $a_B > 14$ nm. We will return to the measurement of the Bohr radius (as a function of x and d) later on, but first

we discuss Γ (as a function of x and d), introducing bubble plots for representing our results.

7.2   Diamagnetic shift coefficient 'bubble plot'

Now we look at the diamagnetic shift data, the results of which are summarized in Fig. 7.7, and will explain the parts of the figure. As the QD-CL mismatch changes with both x and d, it is instructive to plot lines of constant mismatch in Fig. 7.7. These have been calculated according to Eqn-4.1. Hence, by following these lines, only the QD-CL band offset (E_{bo}) changes while the QD-CL mismatch remains constant.

Going horizontally from left to right along the graph (increasing indium content in CLs), both the band offsets between the QDs and CLs, and the lattice-mismatch between the QDs and CLs (thus QD strain) reduce. The mismatch also decreases while going up vertically (along increasing LCL thickness), whilst here the band offsets are constant. We note that the strain does have an effect on the band offsets, but this is neglected.

The bubbles represent the relative values of the diamagnetic shift coefficient, Γ, by their diameters, which is a function of x and d. The samples are categorized into two groups, indicated by blue and red bubbles, according to the behaviour of the PL energy shift in the magnetic field (the green bubble is simply used to indicate two samples with the same x and d parameters). The sizes of the blue bubbles represent the value of Γ for the samples where the carriers' wave-function extent is larger than the magnetic length at ~ 10 T. In other words, the energy shift reaches the high-field regime, where ΔE becomes linear in high-field, revealing that spatial confinement is dominated by magnetic confinement.
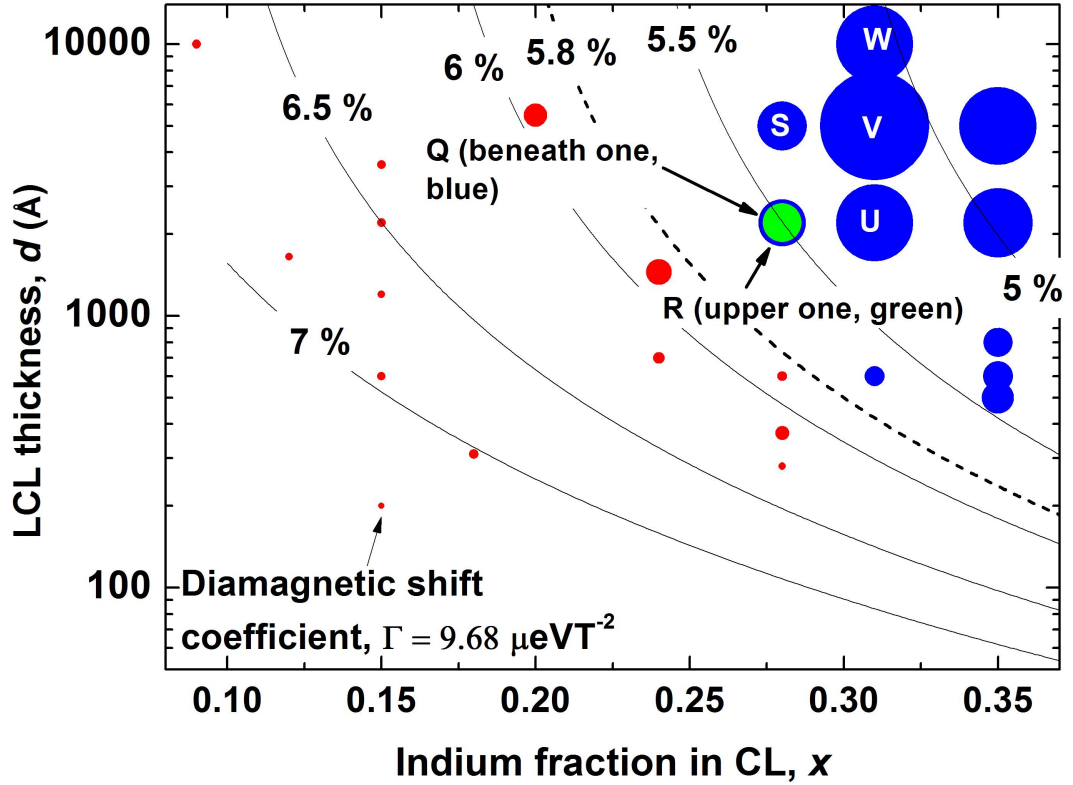
FIGURE 7.7: Bubble plot showing the relative values of the diamagnetic shift coefficient, Γ, at 4.2 K. The solid lines show constant QD-CL mismatch; by following them, only the band offsets are changing. For the sample with $x = 0.15$ and $d = 200$ Å, $\Gamma = 9.68$ μeVT^{-2}: the values for other samples are proportionally larger relative to this bubble diameter. The blue/green and red colours show the energy shift for samples reaching and not reaching the high-field regime, respectively (green is used to distinguish different samples with the same values of x and d). The bubbles labelled with W, V, U, S, Q and R are for the samples with $a_B > 14$ nm. The dashed line, representing the 5.8 % mismatch, differentiate the red and blue/green samples, i.e, samples with > 5.8 % are red while those with < 5.8 % are blue/green.

For these samples, the magnetic field is sufficient to allow us to determine the exciton Bohr radius, a_B, and reduced mass, μ (see Fig. 7.2). The red bubbles represent the values of Γ for the samples where carriers wave-function extent is smaller than the

magnetic length at high field, and the energy shift remains parabolic [141]. For these samples, we are unable to determine the exciton Bohr radius and reduced mass.

An immediately obvious and intriguing trend in the figure is the twelvefold increase in the diamagnetic shift coefficient while going from mismatch ~ 7 % to ~ 5 %. Large values of Γ are attributed to spill over of the carriers' wave-functions [142] which results from the small barrier formed by the large indium content in the confining layers, and to a low reduced mass of carriers which, in turn, is due to low QD-CL mismatch. The decrease in the reduced mass of the exciton with decreasing QD-CL mismatch is also evident from Fig. 7.2(a), while the wave-function spill-over is evidenced in Fig. 7.2(b), and Fig. 7.7

Furthermore, it can be seen in the figure that samples with QD-CL mismatch > 5.8 %, indicated by red, do not reach the high-field regime. The high QD-CL mismatch (QD strain), which is due to the low indium content in the confining layers, results in a high reduced mass, reduced separation of confined states and compact wave function. For these samples, the Bohr radius remains smaller than the magnetic length to the highest available fields. Conversely, for the samples with mismatch $<$ 5.8 %, indicated by blue, the high-field limit is reached. For these samples d is large, which reduces the QD-CL mismatch, and the In content in the CLs is high which reduces the band offset as well as QD-CL mismatch. This makes the reduced mass of the carriers low, hence the wave-function is enlarged. Taken together Figs. 7.2 and 7.7, imply that the effective mass plays a key role in the strength of the confinement, and possibly that strong confinement as defined in chapter-1, i.e., E_q and $E_l >> kT$, which may be alternatively expressed as $a_B \simeq$ dot radius $<<$ unconfined exciton radius (for given reduced mass and dielectric constant), has best been achieved for a sample with $x = 0.31$ and $d = 600$ Å.

Furthermore, whilst the available magnetic field in the experiment is somewhat arbitrary (for some samples it is enough to reach the high-field regime while for some it

is not), the fact that the samples which reach the high-field limit can be delineated by a line of constant QD-CL mismatch of 5.8 % is noteworthy, especially given the results in Figs. 7.2, 7.5 and 7.6.

7.3   Bohr radius 'bubble plot'

Having introduced and explained the bubble plot, we can now discuss the Bohr radius data in the same manner, which reveals some unexpected behaviour. Fig. 7.8 shows that a_B decreases with increasing barrier height (decreasing x) and mismatch, while going horizontally from $x = 0.31$ to 0.28 for any particular LCL thickness. This is understandable, because increasing the barrier results in an increase of the localization energy which, in turn, improves confinement and hence the reduces Bohr radius. Similarly, Fig. 7.2(a) shows that for these samples, increasing mismatch increases the effective mass, and the exciton Bohr radius is inversely proportional to effective mass [31]. However, going from $x = 0.35$ to $x = 0.31$, the opposite behaviour is observed. Furthermore, AFM measurements [70] show that at $x = 0.35$, the QD diameter is bigger (31 nm) than at $x = 0.31$ (22 nm), therefore, from the general trend in Fig. 7.8 and the decrease in the dot diameter, going from $x = 0.35$ to $x = 0.31$, we expect a reduction in Bohr radius, which is not the case, apparently. There are a number of possible reasons for this anomalous behaviour, two of which we now go on to discuss in detail.

Initially we explained this behaviour by considering an analogy taken between the wave-function and a balloon, where it has been suggested that the exciton wave-function can be thought as a balloon [112]. This means that by 'pushing down' on the wave-function (balloon), it expands laterally; squashing it laterally results in its vertical spill over. In this case, a higher barrier height (increased localization energy) at $x = 0.31$ than 0.35 causes the wave-function to be squashed vertically and, consequently, expanded laterally.
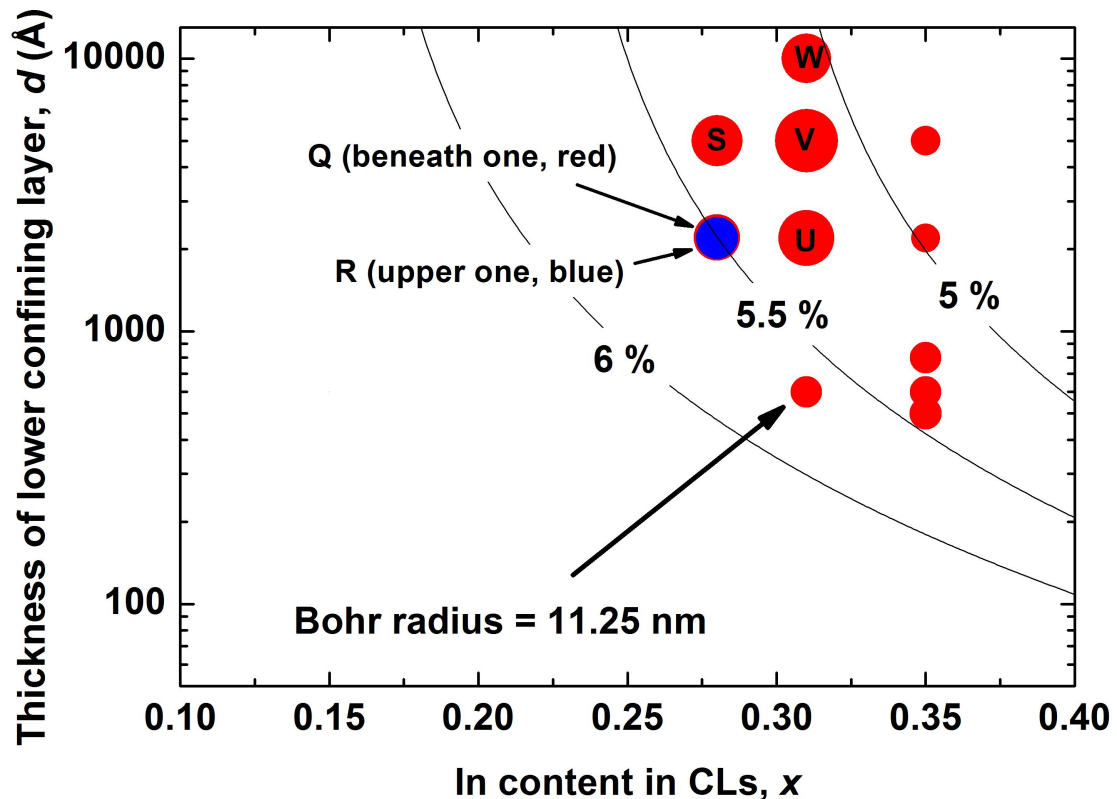
FIGURE 7.8: The size of bubbles represents the value of the exciton Bohr radius, at 4.2 K, as a function of indium content, x, in CLs and LCL thickness, d (blue is used to distinguish different samples with the same values of x and d). The lines show constant QD-CL mismatch. The bubbles show the Bohr radii of excitons only for the samples for which the high-field regime is reached. The arrow indicates the value of the exciton Bohr radius for the sample with $x = 0.31$ and $d = 600 \mathring{A}$; the values for other samples are proportionally larger relative to the bubble diameter.

In order to gain further insight into the confinement of the carriers inside the dots and to test this balloon analogy explanation, we calculated electronic energy states for our samples using COMSOL Multiphysics 4.4 software. The 1-band Schrodinger equation,

$$- \hbar^2 \nabla . (\frac{1}{m_e(\vec{x})} \nabla \psi(\vec{x})) + V_e(\vec{x})\psi(\vec{x}) = E\psi(\vec{x}) \ , \qquad (7.2)$$

was solved for the conduction band in the single-particle effective-mass approximation for experimentally observed pyramidal quantum dots structure. Here $\hbar$, $m_e(\vec{x})$,

$V_e(\vec{x})$, E, and $\psi(\vec{x})$ are Planck's constant divided by 2π, the position-dependent electron effective mass, the position-dependent band-edge potential energy, the electron energy, and the electron envelope function, respectively. The structure has been approximated as conical in order to simplify computational treatment by reducing the model to two dimensions using cylindrical coordinates [143]. The band gap energies of InAs and GaAs are 0.35 eV and 1.42 eV respectively, while the band gap energy of $In_xGa_{1-x}As$ varies, depending upon the indium content present in the CLs, by a relation,

$$E_g(In_xGa_{1-x}As) = (1-x)E_g(GaAs) + xE_g(InAs) - x(1-x)0.477 \ , \qquad (7.3)$$

where $E_g(In_xGa_{1-x}As)$, $E_g(GaAs)$ and $E_g(InAs)$ are the band gap energies of $In_xGa_{1-x}As$, GaAs and InAs, respectively, while x is the indium content present in the CLs. The electron band offset of InAs, GaAs and $In_xGa_{1-x}As$ are calculated by taking 60 % [144] of their corresponding band gap energies, i.e. $0.35 \times 0.6 = 0.21$ eV for InAs, $1.42 \times 0.6 = 0.852$ eV for GaAs and $E_g(In_xGa_{1-x}As) \times 0.6$ eV for $In_xGa_{1-x}As$. However, for simplification, the band offset of InAs is considered to be zero as a reference and, consequently, its value (0.21 eV) is subtracted from the band offset of GaAs and $In_xGa_{1-x}As$, i.e. $0.852 - 0.21 = 0.642$ eV and (band offset of $In_xGa_{1-x}As$) $- 0.21$ eV. By assuming the barrier potential to be circularly symmetric, the wave-function extent in lateral direction can be written as,

$$< r >= \int_{-\infty}^{\infty} dz \int_0^{2\pi} r d\theta \int_0^{\infty} dr \ \psi^*(r,z,\theta) \ r \ \psi(r,z,\theta) \ , \qquad (7.4)$$

where ψ is the wave-function; r, θ and z are the cylindrical coordinates.

The conduction band for the structure is shown in the right-top inset of Fig. 7.9. The simulated results are shown in Fig. 7.9, which depict the dependence of the electron's lateral wave-function extent on the band offset of the quantum dot. It is obvious from the figure that the lateral exciton wave-function extent monotonically increases with

decreasing E_{bo} and is thus bigger at $x = 0.35$ than $x = 0.31$, which is contrary to the experimental results shown in the Fig. 7.8. Thus, the modelling results do not support the 'balloon' explanation of wave-function spill over, and furthermore imply that an experimental reason for this behaviour must be found.
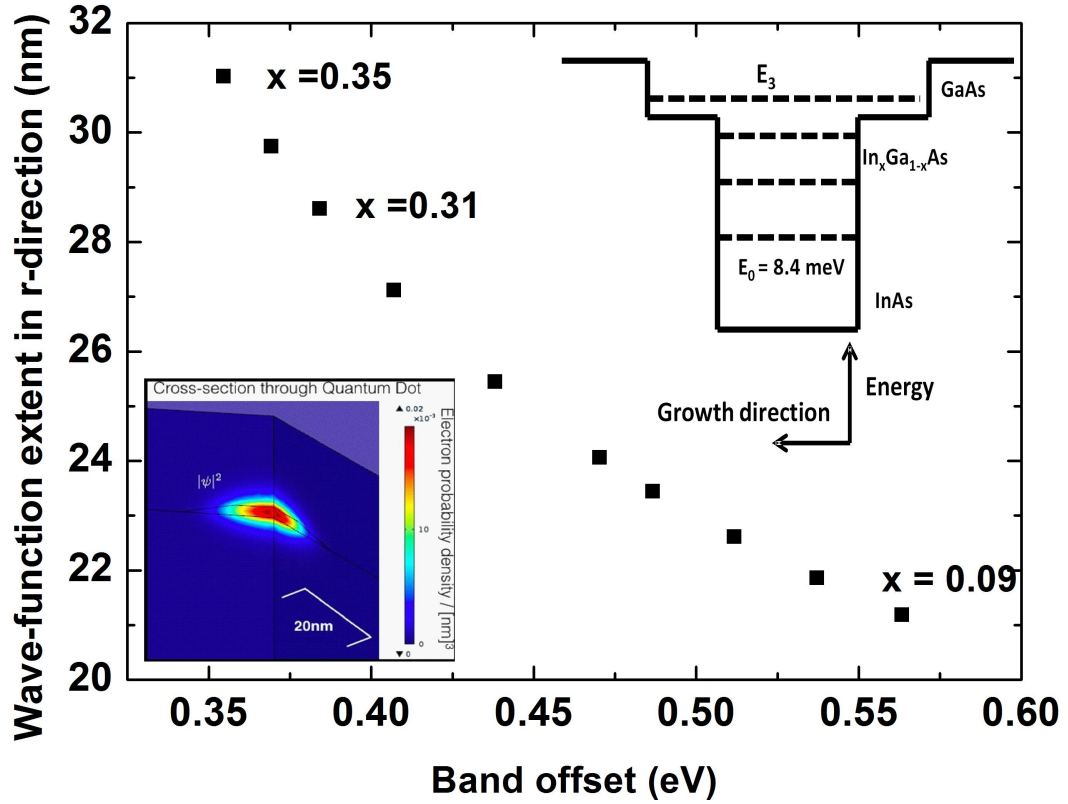
FIGURE 7.9: Calculated exciton wave-function extent in the lateral direction (sample plane), defined as $< r >= \int \psi r \psi$, as a function of band offset which is determined by the indium content, x in the barrier. The left-bottom inset shows a colour probability plot of a typical simulated wave-function for $E_{bo} = 0.38$ eV, $x = 0.31$. The right-top inset shows the conduction band structure for the same sample. The horizontal solid lines show the conduction bands for InAs, In$_x$Ga$_{1-x}$As and GaAs while the dotted lines represent the first four energy levels, E_0, E_1, E_2 and E_3, of the electron in the dot. The first energy level state, E_0, was calculated as 8.4 meV.

The contradiction between experimental and theoretical results can be resolved with reference to the work of T. Nuytten et al [128]. They showed that dots with different

sizes exist in InAs/GaAs structures and that a thermal escape of carriers from higher-energy (smaller) dots to lower-energy (bigger) dots occurs via the wetting layer, which is indicated by an anomalous behaviour of the PL energy with increasing temperature relative to that predicted by the Varshni law [30].

T. Nuytten and his co-workers also studied [128] the temperature dependence of the PL energy in magnetic field and concluded that for dots where such a redistribution of carriers occurs, in the presence of magnetic field, the contribution of the smaller dots (high-energy dots) to the PL energy is greater relative to the bigger (low-energy dots) as the temperature increases. Thus, with increasing temperature, the PL energy shift in magnetic field is smaller. The application of a magnetic field increases the energy gap between the states in the QDs and the states of the surrounding bulk material. This increase originates from the fact that the magnetic field raises the energy levels of the surrounding materials and of the QDs substantially and moderately, respectively as shown in Fig. 7.10.

The effect of magnetic field on the energy levels depends upon the confinement potentials of the excitons present in the dots. The field has a stronger effect on the energy levels with weaker confinement, such as in bigger dots; on the contrary, carriers in smaller dots (strong confinement) are less affected, i.e. confined energy levels are lifted much less in smaller dots than bigger ones. The band offset of QD is enhanced equally in both type of dots, as a result of the magnetic field, but the localization energy of carriers for smaller dots goes up more than for bigger dots, due to the differences in the field dependence of the confined states. This results in an energy difference between the QD levels and surrounding material that is higher for the smaller dots than the bigger ones. In other words, on application of a magnetic field the confinement potential is deepened much more in smaller dots than bigger one. The net result is that in a magnetic field we tend to probe smaller dots, and the effect is enhanced with increasing temperature, as this allows carriers to move between the dots.
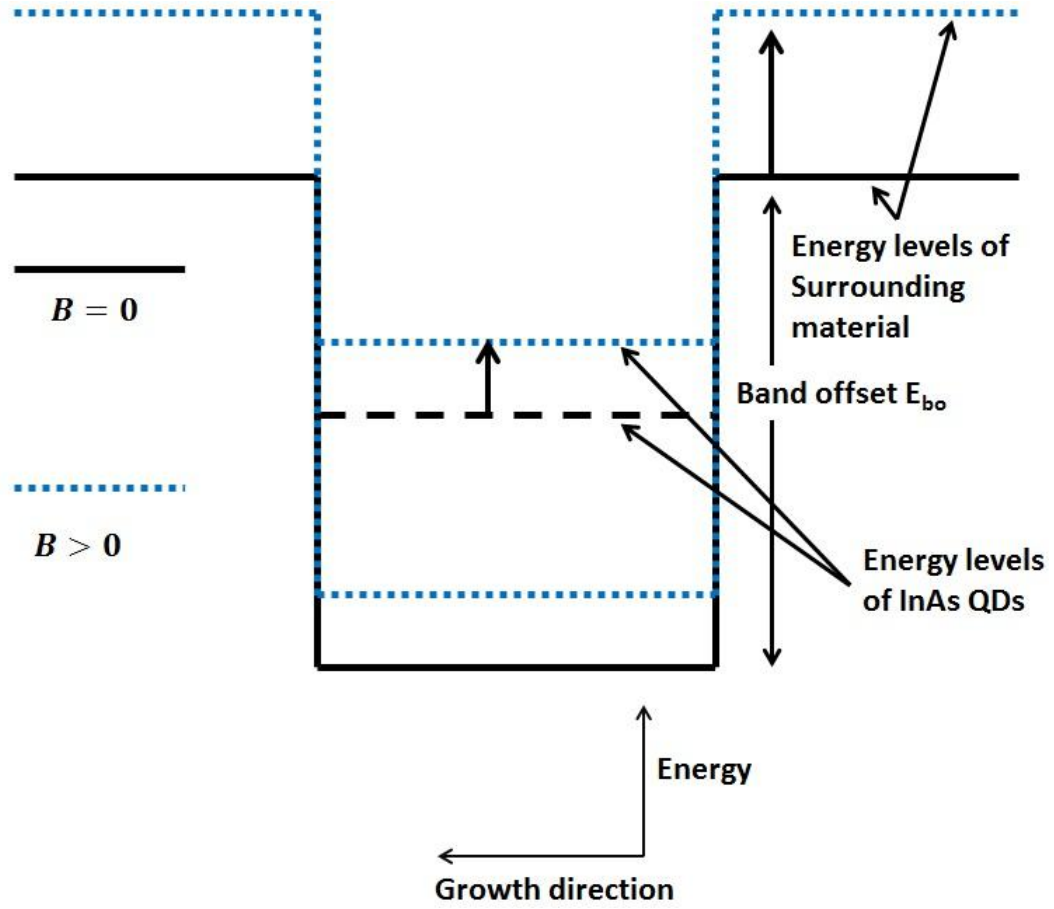
FIGURE 7.10: Schematic representation of the electron energy levels of the InAs QDs and the surrounding material as they are lifted by the magnetic field. The solid black lines represent the case when the field is zero while the blue dotted lines represent the case when the field is applied and raises the energy levels.

We thought that a similar phenomenon occurs in our samples with $x = 0.35$. Therefore, in order to investigate the possibility of the presence of dots with different sizes and the potential migration of carriers among them, mentioned above, in the samples with $x = 0.35$, we studied the dependence of their PL energies on temperature in zero field as well as in fielda ranging from 0 - 15 T, and compared them with another sample containing a low indium content in the CLs, i.e. $x = 0.15$. The behaviour of the zero-field PL energies with increasing temperature is shown in Fig. 7.11 for both types of samples, i.e., with $x = 0.15$ and 0.35. The fits (dashed lines) are drawn by

selecting free parameters, α and β, while using the equation (2.14) which describes the Varshni law showing the temperature, T, dependence of energy, $E_g(T)$.
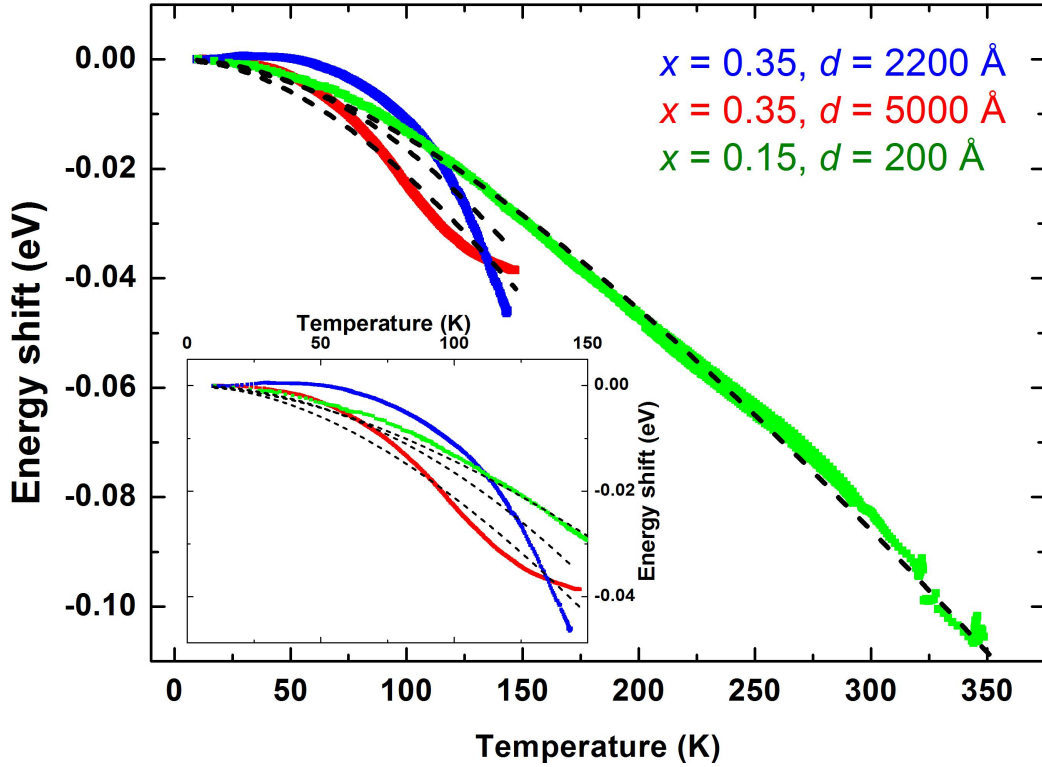
FIGURE 7.11: PL energy shift versus temperature in zero field for samples with $x = 0.35$ and $d = 2000$ Å (blue), $x = 0.35$ and $d = 5000$ Å (red) and $x = 0.15$ and $d = 2000$ Å (green). For $x = 0.35$ samples, confinement is weak and the PL is quenched above $\sim$145K. Dashed lines are Varshni fits. The PL energy of the sample with $x = 0.15$ and $d = 200$ Å decreases, more or less, according to the Varshni law, whereas for samples with $x = 0.35$ the energies decrease faster than predicted. The inset shows a zoomed-in part of the figure to see the fits clearly.

It can be seen in the figure that the blue and red energy shifts, for samples with $x = 0.35$, decrease faster with increasing temperature than predicted by the Varshni law, whereas for the sample with $x = 0.15$ (green), the energy decreases, more or less, according to the predictions of the Varshni law. We interpret the peculiar dependence of the PL energy on temperature, in the samples with $x = 0.35$, to the presence of dots with different sizes. Due to higher CL indium content, the potential barrier

of the quantum dot (and hence localization energy) is lower, therefore by increasing the temperature, carriers escape from smaller dots to bigger ones. The quantization energy, E_q, is lower in the bigger dots than the smaller dots, thus the PL emission energy emitting from the bigger dot is lower than the smaller ones. Fig. 7.12 shows line-width as a function of temperature, T, for samples with different parameters: blue, red and black represent the samples with $x = 0.35$ and $d = 2200$ $\overset{\circ}{A}$; $x = 0.35$ and $d = 5000$ $\overset{\circ}{A}$; and $x = 0.15$ and $d = 200$ $\overset{\circ}{A}$, respectively.
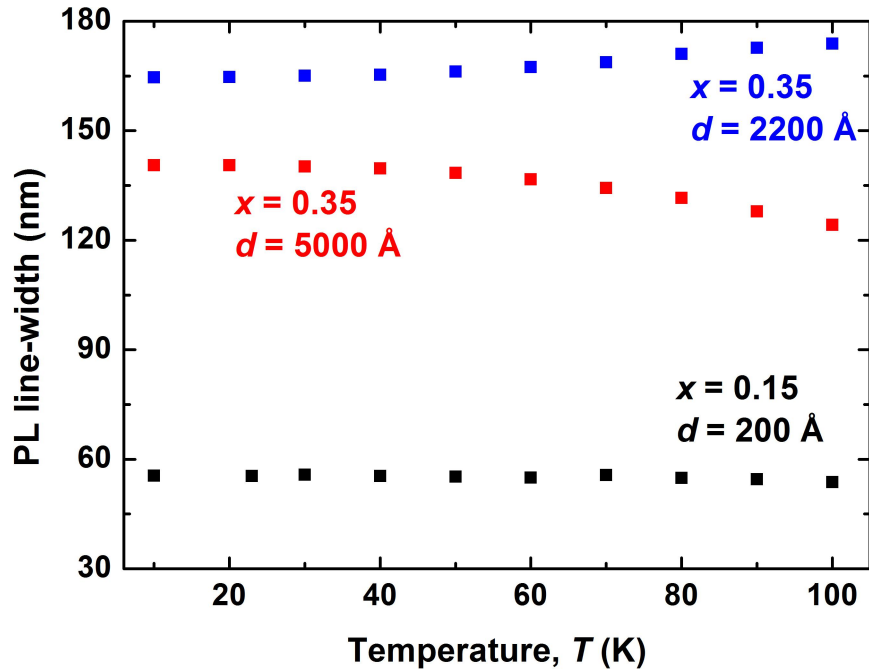
FIGURE 7.12: PL line-width as a function of temperature, T, for two samples with $x = 0.35$ (blue and red) and for one sample with $x = 0.15$ (black). For sample with low indium content, $x = 0.15$, there is no change in line-width with increasing temperature from 10 K to 100 K, while for samples with $x = 0.35$ and $d = 2200$ $\overset{\circ}{A}$; $x = 0.35$ and $d = 5000$ $\overset{\circ}{A}$, the line-width increases and decreases, respectively, with increasing temperature.

It can be seen that for sample with low indium content in the confining layers, $x = 0.15$ (black), there is no change in PL line-width with increasing temperature from 10 K to 100 K, while for samples with high indium content in the confining layers, $x = 0.35$ and $d = 2200$ $\overset{\circ}{A}$ (blue); $x = 0.35$ and $d = 5000$ $\overset{\circ}{A}$ (red), the

line-width increases and decreases, respectively. The invariance in line-width (black) with increasing temperature can be explained as: the PL emission is contributed by average of all dots and with increasing temperature, it does not change as there is no thermal redistribution (charge migration) of carriers between dots. The decrease in the line-width (red) can be attributed to the presence of QDs with different sizes, with carriers migrating from smaller dots to the bigger ones, thus a subset (of only bigger dots) contributes to the PL emission decreasing the line-width [145, 146]. The slight increase with temperature for $x = 0.35$, $d = 2200 \mathring{A}$ is unusual, possibly implying that with increasing temperature a broader distribution of dot sizes contributes to the PL as a result of thermal migration.

This explanation is reinforced by Fig. 7.13, which shows the energy shift for the sample with $x = 0.35$ and $d = 2200$ $\mathring{A}$: it decreases by a factor of ~ 2 with increasing temperature from 2 K to 100 K in the presence of magnetic field (0 - 15) T, which is very similar to the behaviour observed in Fig. 1 of the work presented by T. Nuytten et al [128]. The energy levels of surrounding material, $In_{0.35}Ga_{0.65}As$ in this case, are lifted by

$$\Delta E = \frac{1}{2}\hbar\omega_c \ , \tag{7.5}$$

where ω_c is the cyclotron frequency and given by

$$\omega_c = \frac{eB}{m_e} \ . \tag{7.6}$$

Here, e, B and m_e are the charge of electron, magnetic field and mass of electron, respectively. The mass of electron for the surrounding material, $In_{0.35}Ga_{0.65}As$, is given by,

$$m_e = 0.023 + 0.037(1 - x) + 0.003(1 - x)^2(m_0) \ , \tag{7.7}$$

where x is the indium content in confining layers and m_0 is the free electron mass. Putting $x = 0.35$ in equation-7.7, the mass of electron, $m_e = 0.048$. Putting this in

equation-7.6, we get

$$\omega_c = 5 \times 10^{-17} \left(\frac{1}{s}\right) \ . \tag{7.8}$$
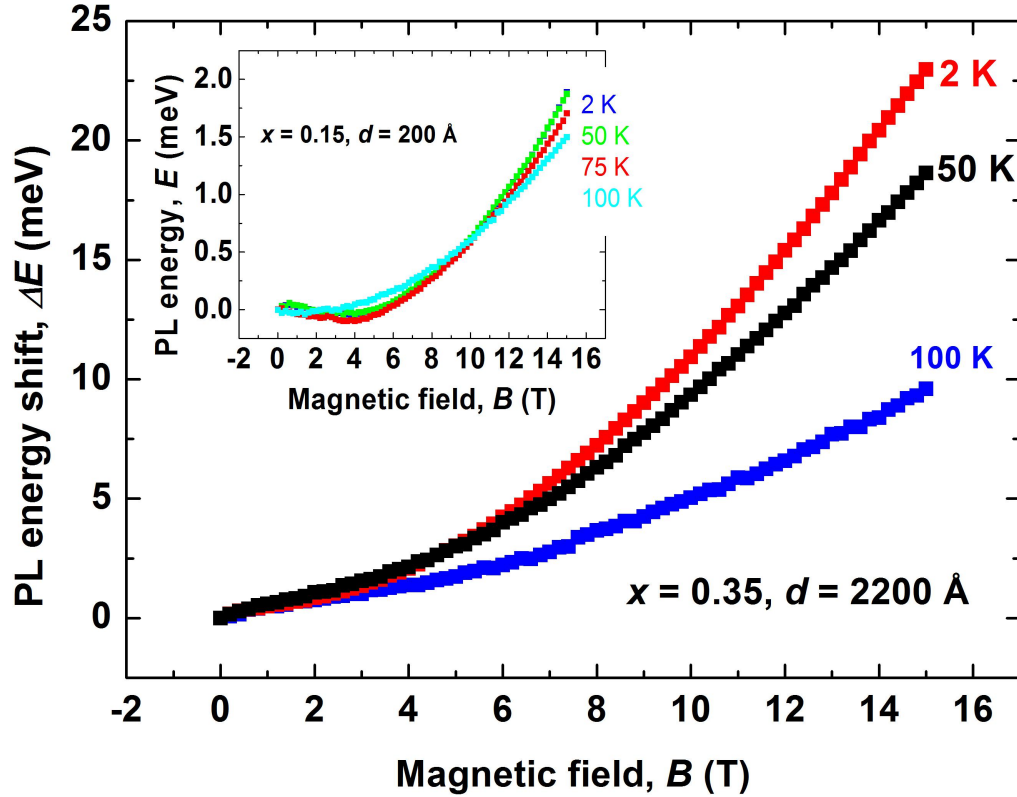
FIGURE 7.13: PL energy shift, ΔE vs. magnetic field, B at various temperatures, i.e. 2 K (red), 50 K (black) and 100 K (blue) for the sample with $x = 0.35$ and $d = 2200\mathring{A}$. The figure shows that the energy shift decreases by a factor of ~ 2 with increasing temperature, from 2 K to 100 K. The inset shows the behaviour of PL energy at various temperatures in the presence of magnetic field for the sample with $x = 0.15$ and $d = 200\mathring{A}$; the energy shift does not decrease significantly with increasing temperature from 2 K to 100 K.

Thus equation-7.5 implies that $\Delta E = 18$ meV: the energy level of $In_{0.35}Ga_{0.65}As$ is lifted by 18 meV while applying 15 T magnetic field. In other words, the energy shift in energy level is 1.20 meV/T.

If we equate the 2K PL shift to bigger dots (actually it should be average), then the QD level shifts by 23 meV at 15 T (Fig. 7.13). This is very similar to the shift at the

bulk states, i.e. little or no field-enhanced confinement effect. We suggest that the much smaller shift at 100 K is dominated by small dots, and is 10 meV (Fig. 7.13). This is about half of the shift at the bulk states, adding 8 meV to the localization energy at 15 T. Due to the large indium content in the barriers ($x = 0.35$), the zero-field localization energy is calculated to be only 20 meV (for an average dot). Hence for smaller dots the field increases the localization energy by 40 % at 15 T (and has no effect for large dots). This implies that, at higher temperature, the contribution of the smaller dots to the PL becomes more prominent. In contrast, it is clear from the inset that the energy shift for the sample with $x = 0.15$ and $d = 200$ Å does not decrease significantly as temperature increases from 2 K to 100 K. In such samples, all dots contribute to PL energy: it is an average of all, rather than being biased towards smaller dots (as temperature increases). Thus, the reason for the smaller radii at $x = 0.35$ than $x = 0.31$ in Fig. 7.8 is the large contribution of the smaller dots to the PL energy which results in smaller radii.

Chapter 8

Summary and Further Work

In this work, we have probed the confinement of excitons in InAs QDs, embedded in strain-engineered metamorphic InAs/In$_x$Ga$_{1-x}$As/GaAs confining layers, using magneto-photoluminescence at low temperature, 4.2 K. In total, 46 samples were studied, out of which 28 gave useful results in terms of bright spectra and analysable data while the the data gained from rest of the samples was noisy and unable to analyse. The main results are summarized below.

Results consisting of zero-magnetic-field spectra showed that wavelength (PL energy) increases (decreases) with increasing x, for a constant d, and with d, for a constant x. This was attributed to be due to reduction of QD-strain that is, in turn, a function of x and d. No correlation between wavelength and intensity was observed.

Magneto-photoluminescence results revealed that for a subset of samples, where the high-field regime was reached, the effective mass of the exciton increases approximately linearly with increasing QD-CL mismatch, and hence strain inside the QD. By establishing a correlation between QD-CL mismatch and strain in the LCL, it has been further shown that the effective mass depends on the strain in the LCL as well. No correlation between QD-CL mismatch and the Bohr radius of the exciton was observed. The radius of the exciton for one sample with $x = 0.31$ and $d = 600$ $\mathring{A}$,

11.25 nm, was found to be equal, more or less, to its corresponding dot radius. For high mismatch dots it is inferred that $a_B <$ dot radius, likely due to high strain and large effective mass, implying that lateral confinement in conventional InAs/GaAs QDs may be quite weak.

Results of the diamagnetic shift coefficient showed that for the samples with high QD-CL mismatch (> 5.8 %), the high-field regime is not reached in the available field (15 T), while for samples with low mismatch (< 5.8 %) the high-field regime is reached. Furthermore, the diamagnetic shift coefficient increases 12-fold with decreasing mismatch (from ~ 7.5 % to ~ 4.5 %). This was attributed to a decrease in effective mass and an enlarged wave-function, which, in turn, is due to a decrease in QD-CL mismatch.

By drawing the Bohr radius on a bubble plot, it was noticed that it decreases with decreasing x while going from $x = 0.31$ to 0.28, which was expected: the decreasing x increases the band offset which provides better lateral confinement. For $x = 0.35$, however, counter-intuitively, the observed exciton radius was smaller than at $x = 0.31$. It was, initially, suggested that, due to low barrier, at $x = 0.35$, the exciton wave-function spills over vertically resulting in a small lateral radius. In order to check this explanation, model calculations were carried, but they did not support this explanation of spilling over of exciton wave-function. Alternatively, it was explained by looking into the dependence of the PL energy on temperature and magnetic field, at various temperatures. These experiments showed that there are different dots with different sizes, with thermal escape of carriers with increasing temperature occurring such that smaller dots contribute more to the PL energy than the bigger ones, in magnetic field. Therefore the determined radii, at $x = 0.35$, are those in the smaller dots rather than the average of all the assembly of the dots. This effect was observed at $x = 0.35$ due to the low QD-CL band offset.

Further work can be measuring the samples, for which the high-field regime has not

been reached, in pulsed magnetic field, up to 50 T, to determine their exciton reduced mass and Bohr radius. We have sent these samples to KU-Leuven, Belgium, for this purpose. Until now, two samples with $x = 0.15$, $d = 600$ $\mathring{A}$ and $x = 0.12$, $d = 1650$ $\mathring{A}$ have been measured. The data has not been fully analysed yet but the high-field regime was indeed reached at very high field (~ 30 T), consistent with results presented here. Similarly, our results showing the approximate linear relationship between effective mass and QD-CL mismatch is very important and could stimulate theoretical investigation.

Finally, samples of the same structures but with additional InAlAs barrier, which emit at longer wavelength than our measured samples, are also available and would warrant detailed investigation.

Bibliography

[1] M. Grundmann, D. Bimberg, and N. N. Ledentsov. *Quantum Dot Heterostructures*. Wiley, Chichester, 1999.

[2] N.N. Ledentsov, V.A. Shchukin, T. Kettler, K. Posilovic, D. Bimberg, L.Ya. Karachinsky, A.Yu. Gladyshev, M.V. Maximov, I.I. Novikov, Yu.M. Shernyakov, A.E. Zhukov, V.M. Ustinov, and A.R. Kovsh. MBE-grown metamorphic lasers for applications at telecom wavelengths. *J. Cryst. Growth*, 301/302:914 – 922, 2007.

[3] N. Horiguchi, T. Futatsugi, Y. Nakata, N. Yokoyama, M. Tanaya, and P. M. Petroff. Quantum dot infrared photodetector using modulation doped InAs self-assembled quantum dots. *Jpn. J. Appl. Phys.*, 38:2559, 1999.

[4] J. Tatebayashi, N. Hatori, H. Kakuma, H. Ebe, H. Sudo, A. Kuramata, Y. Nakata, M. Sugawara, and Y. Arakawa. Low threshold current operation of self-assembled InAs/GaAs quantum dot lasers by metal organic chemical vapour deposition. *Electron. Lett.*, 39:1130–1131, 2003.

[5] M. Sugawara, N. Hatori, M. Ishida, H. Ebe, Y. Arakawa, T. Akiyama, K. Otsubo, T. Yamamoto, and Y. Nakata. Recent progress in self-assembled quantum-dot optical devices for optical telecommunication: temperature-insensitive $10Gbs^{-1}$ directly modulated lasers and $40Gbs^{-1}$ signal-regenerative amplifiers. *J. Phys. D Appl. Phys.*, 38:2126, 2005.

[6] A. Marent, T. Nowozin, Geller, and D. Bimberg. The qd-flash: a quantum dot-based memory device. *Semicond. Sci. Tech.*, 26:014026, 2011.

[7] L. Sapienza, M. Davanco, A. Badolato, and K. Srinivasan. Nanoscale optical positioning of single quantum dots for bright and pure single-photon emission. *Nat. Commun.*, 6:7833, 2015.

[8] O. B. Shchekin and D. G. Deppe. 1.3 μm InAs quantum dot laser with $T_0 = 161K$ from 0 to 80 °C. *Appl. Phys. Lett.*, 80:3277–3279, 2002.

[9] M. Sugawara, K. Mukai, and Y. Nakata. Light emission spectra of columnar-shaped self-assembled InGaAs/GaAs quantum-dot lasers: effect of homogeneous broadening of the optical gain on lasing characteristics. *Appl. Phys. Lett.*, 74:1561–1563, 1999.

[10] H.Y. Liu, D.T. Childs, T.J. Badcock, K.M. Groom, I.R. Sellers, M. Hopkinson, R.A. Hogg, D.J. Robbins, D.J. Mowbray, and M.S. Skolnick. High-performance three-layer 1.3-μm InAs/GaAs quantum-dot lasers with very low continuous-wave room-temperature threshold currents. *P. Tech. Lett. IEEE*, pages 1139–1141, 2005.

[11] Z. Mi, P. Bhattacharya, and S. Fathpour. High-speed 1.3 μm tunnel injection quantum-dot lasers. *Appl. Phys. Lett.*, 86:153109, 2005.

[12] M.S. Skolnick and D.J. Mowbray. Self-assembeled semiconductor quantum dots: Fundamanental physics and device application. *Annu. Rev. Mater. Res*, 34:181–218, 2004.

[13] D. Bera, L. Qian, T. Tseng, and P. H. Holloway. Quantum dots and their multimodal applications: a review. *Material*, 3:2260–2345, 2010.

[14] D. Gammon. Semiconductor physics: electrons in artificial atoms. *Nature*, 405:899, 2000.

[15] L. E. Brus. A simple model for the ionization potential, electron affinity, and aqueous redox potentials of small semiconductor crystallites. *J. Chem. Phys.*, 79:5566–5571, 1983.

[16] M. Hayne, J. Maes, Y.M. Manz, O.G. Schmidt, K. Eberl, and V.V. Moshchalkov. Electron and hole confinement in stacked self-sssembled InP dots of different sizes. *Phys. Status. Solidi. B*, 224:31–35, 2001.

[17] M. Hayne, J. Maes, S. Bersier, V. V. Moshchalkov, A. Schliwa, L. Mller-Kirsch, C. Kapteyn, R. Heitz, and D. Bimberg. Electron localization by self-assembled GaSb/GaAs quantum dots. *Appl. Phys. Lett.*, 82:4355, 2003.

[18] T. Nowozin, A. Marent, L. Bonato, A. Schliwa, D. Bimberg, E. P. Smakman, J. K. Garleff, P. M. Koenraad, R. J. Young, and M. Hayne. Linking structural and electronic properties of high-purity self-assembled GaSb/GaAs quantum dots. *Phys. Rev. B*, 86:035305, 2012.

[19] A. Graf, D. Sonnenberg, V. Paulava, A. Schliwa, Ch. Heyn, and W. Hansen. Excitonic states in gaas quantum dots fabricated by local droplet etching. *Phys. Rev. B*, 89:115314, 2014.

[20] Y. Kayanuma. Quantum-size effects of interacting electrons and holes in semiconductor microcrystals with spherical shape. *Phys. Rev. B*, 38:9797–9805, 1988.

[21] S Fafard, K Hinzer, S Raymond, M Dion, J McCaffrey, Y Feng, and S Charbonneau. Red-emitting semiconductor quantum dot lasers. *Science*, 274:1350–1353, 1996.

[22] S. Franchi, G. Trevisi, L. Seravalli, and P. Frigeri. Quantum dot nanostructures and molecular beam epitaxy. *Prog. Cryst. Growth. Ch.*, 47:166 – 195, 2003.

[23] C. Kittel. *Introduction to Solid State Physics, Eight Edition*. Wiley, 2004.

[24] Gillespie, D. T. *A Quantum Mechanics Primer*. TBS The Book Service Ltd, 1970.

[25] D. Gammon. Electrons in artificial atoms. *Nature*, 405:899, 2000.

[26] A. L. Efros and A. L. Efros. Interband absorption of light in a semiconductor sphere. *Sov. Phys. Semicond+.*, 16:772–775, 1982.

[27] Y. Wang and N. Herron. Nanometer-sized semiconductor clusters: materials synthesis, quantum size effects, and photophysical properties. *J. Phys Chem-US.*, 95:525–532, 1991.

[28] C. B. Murray, D. J. Norris, and M. G. Bawendi. Synthesis and characterization of nearly monodisperse CdE (E = sulfur, selenium, tellurium) semiconductor nanocrystallites. *J. Am. Chem. Soc.*, 115:8706–8715, 1993.

[29] C. F. Klingshirn. *Semicondutor Optics*. Springer, 2006.

[30] Y.P. Varshni. Temperature dependence of the energy gap in semiconductors. *Physica*, 34:149 – 154, 1967.

[31] M. Hayne and B. Bansal. High-field magneto-photoluminescence of semiconductor nanostructures. *Luminescence*, 27:179196, 2012.

[32] A. Wojs, J. J. Quinn, and P. Hawrylak. Charged excitons in a dilute two dimensional electron gas in a high magnetic field. *Phys. Rev. B*, 62:46307, 2000.

[33] L. Jacak, P. Hawrylak, and A. Wojs. *Quantum Dots*. NanoScience and Technology Series. Springer, 1998.

[34] P. Hawrylak. Excitonic artificial atoms: engineering optical properties of quantum dots. *Phys. Rev. B*, 60:5597608, 1999.

[35] A. Babinski, M. Potemski, S. Raymond, J. Lapointe, and Z. R. Wasilewski. Fock-Darwin spectrum of a single InAs/GaAs quantum dot. *Phys. Status. Solidi. C*, 3:374851, 2006.

[36] P. Miska, J. Even, C. Platz, B. Salem, T. Benyattou, C. Bru-Chevalier, G. Guillot, G. Bremond, Kh. Moumanis, F. H. Julien, O. Marty, C. Monat, and M. Gendry. Experimental and theoretical investigation of carrier confinement in InAs quantum dashes grown on InP (001). *J. Appl. Phys.*, 95:107480, 2004.

[37] M. Grundmann, O. Stier, and D. Bimberg. InAs/GaAs pyramidal quantum dots: strain distribution, optical phonons, and electronic structure. *Phys. Rev. B*, 52:11969–11981, 1995.

[38] G. Bester and A. Zunger. Cylindrically shaped zinc-blende semiconductor quantum dots do not have cylindrical symmetry: atomistic symmetry, atomic relaxation, and piezoelectric effects. *Phys. Rev. B*, 71:045318, 2005.

[39] S. Raymond, S. Studenikin, A. Sachrajda, Z. Wasilewski, S. J. Cheng, W. Sheng, P. Hawrylak, A. Babinski, M. Potemski, G. Ortner, and M. Bayer. Excitonic energy shell structure of self-assembled InGaAs/GaAs quantum dots. *Phys. Rev. Lett.*, 92:187402, 2004.

[40] P. D. Wang, J. L. Merz, S. Fafard, R. Leon, D. Leonard, G. Medeiros-Ribeiro, M. Oestreich, P. M. Petroff, K. Uchida, N. Miura, H. Akiyama, and H. Sakaki. Magnetoluminescence studies of $In_yAl_{1-y}As$ self-assembled quantum dots in $Al_xGa_{1-x}As$ matrices. *Phys. Rev. B*, 53:1645861, 1996.

[41] R. Rinaldi, P. V. Giugno, R. Cingolani, H. Lipsanen, M. Sopanen, J. Tulkki, and J. Ahopelto. Zeeman effect in parabolic quantum dots. *Phys. Rev. Lett.*, 77:3425, 2006.

[42] S. N. Walck and T. L. Reinecke. Exciton diamagnetic shift in semiconductor nanostructures. *Phys. Rev. B*, 57:908896, 1998.

[43] A.H. Macdonald and D.S. Ritchie. Hydrogen energy levels in two dimensions at arbitrary magnetic fields. *Phys. Rev. B*, 33:883644, 1986.

[44] K. L. Janssens, F. M. Peeters, and V. A. Schweigert. Magnetic-field dependence of the exciton energy in a quantum disk. *Phys. Rev. B*, 63:205311, 2001.

[45] Y.P. Varshni. Temperature dependence of the energy gap in semiconductors. *Physica*, 34:149, 1967.

[46] A.I. Finch and A.G. Quarrell. In *P. Roy. Soc. A-Math. Phy.*, page 148. London 48, 1934.

[47] H.Y. Liu, B. Xu, Y. Q. Wei, D. Ding, J. J. Qian, Q. Han, J. B. Liang, and Z. G. Wang. High-power and long-lifetime InAs/GaAs quantum-dot laser at 1080 nm. *Appl. Phys. Lett.*, 79:2868–2870, 2001.

[48] F. M. Ross, J. Tersoff, and R. M. Tromp. Coarsening of self-assembled Ge quantum dots on si(001). *Phys. Rev. Lett.*, 80:984–987, 1998.

[49] E. U. Rafailov, M. A. Cataluna, and W. Sibbett. Mode-locked quantum-dot lasers. *Nat. Photonics*, 1:395–401, 2007.

[50] Y. Zhou, Z.and Xu, B. Hao, R.and Tang, Z. Ren, and Z. Niu. Long-wavelength light emission from self-assembled heterojunction quantum dots. *J. Appl. Phys.*, 103:094315, 2008.

[51] N. N. Ledentsov. Quantum dot laser. *Semicond. Sci. Tech*, 26:014001, 2011.

[52] C. Y. Liu, M Stubenrauch, and D Bimberg. Quantum dot laser. *Nanotechnology*, 22:235202, 2011.

[53] C. Paranthoen, N. Bertru, O. Dehaese, A. Le Corre, S. Loualiche, B. Lambert, and G. Patriarche. Height dispersion control of InAs/InP quantum dots emitting at 1.55 μm. *Appl. Phys. Lett.*, 78:1751–1753, 2001.

[54] E. C. Le Ru, A. J. Bennett, C. Roberts, and R. Murray. Strain and electronic interactions in InAs/GaAs quantum dot multilayers for 1300 nm emission. *J. Appl. Phys.*, 91:1365–1370, 2002.

[55] L. Bouzaiene, B. Ilahi, L. Sfaxi, F. Hassen, H. Maaref, O. Marty, and J. Dazord. Tuning vertically stacked InAs/GaAs quantum dot properties under spacer thickness effects for 1.3 μm emission. *Appl. Phys. A*, 79:587–591, 2004.

[56] H. Y. Liu, M. J. Steer, T. J. Badcock, D. J. Mowbray, M. S. Skolnick, P. Navaretti, K. M. Groom, M. Hopkinson, and R. A. Hogg. Long-wavelength light emission and lasing from InAs/GaAs quantum dots covered by a GaAsSb strain-reducing layer. *Appl. Phys. Lett.*, 86:143108, 2005.

[57] H. Y. Liu, M. J. Steer, T. J. Badcock, D. J. Mowbray, M. S. Skolnick, F. Suarez, J. S. Ng, M. Hopkinson, and J. P. R. David. Room-temperature 1.6 μm light emission from InAs/GaAs quantum dots with a thin GaAsSb cap layer. *J. Appl. Phys.*, 99:046104, 2006.

[58] E. C. Le Ru, P. Howe, T. S. Jones, and R. Murray. Strain-engineered InAs/-GaAs quantum dots for long-wavelength emission. *Phys. Rev. B*, 67:165303, 2003.

[59] E. C. Le Ru, J. Fack, and R. Murray. Temperature and excitation density dependence of the photoluminescence from annealed InAs/GaAs quantum dots. *Phys. Rev. B*, 67:245318, 2003.

[60] M. Usman, S. Heck, E. Clarke, P. Spencer, H. Ryu, R. Murray, and G. Klimeck. Experimental and theoretical study of polarization-dependent optical transitions in InAs quantum dots at telecommunication-wavelengths (1300-1500 nm). *J. Appl. Phys.*, 109:04510, 2011.

[61] M.A. Majid, D.T.D. Childs, H. Shahid, Siming Chen, K. Kennedy, R.J. Airey, R.A. Hogg, Edmund Clarke, P. Howe, P.D. Spencer, and Ray Murray. Toward

1550-nm GaAs-based lasers using InAs/GaAs quantum dot bilayers. *IEEE J. Sel. Top. Quant.*, 17:1334–1342, 2011.

[62] P.B Joyce, T.J. Krzyzewski, G.R. Bell, T.S. Jones, S. Malik, D. Childs, and R. Murray. Growth rate effects on the size, composition and optical properties of InAs/GaAs quantum dots grown by molecular beam epitaxy. *J. Cryst. Growth*, 227228:1000 – 1004, 2001.

[63] P. B. Joyce, T. J. Krzyzewski, G. R. Bell, T. S. Jones, E. C. Le Ru, and R. Murray. Optimizing the growth of 1.3 μm InAs/GaAs quantum dots. *Phys. Rev. B*, 64:235317, 2001.

[64] R. Murray and P.N. Stavrinou. 1.3 micron room temperature electroluminscence from InAs/GaAs self- assembled quantum dots. *Jpn. J. Appl. Phys. 1*, 38, 1999.

[65] L. Bouzaiene, B. Ilahi, L. Sfaxi, F. Hassen, H. Maaref, O. Marty, and J. Dazord. Tuning vertically stacked InAs/GaAs quantum dot properties under spacer thickness effects for 1.3μm emission. *J. Phys. D*, 38:2142, 2005.

[66] J. S. Kim, P. W. Yu, J. I. Lee, J. S. Kim, S. G. Kim, J. Y. Leem, and M. Jeon. Height-controlled InAs quantum dots by using a thin InGaAs layer. *Appl. Phys. Lett.*, 80:4714–4716, 2002.

[67] V. M. Ustinov, N. A. Maleev, A. E. Zhukov, A. R. Kovsh, A. Yu. Egorov, A. V. Lunev, B. V. Volovik, I. L. Krestnikov, Yu. G. Musikhin, N. A. Bert, P. S. Kopev, Zh. I. Alferov, N. N. Ledentsov, and D. Bimberg. InAs/InGaAs quantum dot structures on GaAs substrates emitting at 1.3 μm. *Appl. Phys. Lett.*, 74:2815–2817, 1999.

[68] A. Stintz, G. T. Liu, A. L. Gray, R. Spillers, S. M. Delgado, and K. J. Malloy. Characterization of InAs quantum dots in strained In$_x$Ga$_{1-x}$As quantum wells. *J. Vac. Sci. Technol. B*, 18:1496, 2000.

[69] H. Y. Liu, M. Hopkinson, C. N. Harrison, M. J. Steer, R. Frith, I. R. Sellers, D. J. Mowbray, and M. S. Skolnick. Optimizing the growth of 1.3 μm InAs/InGaAs dots-in-a-well structure. *J. Appl. Phys.*, 93:2931–2936, 2003.

[70] L. Seravalli, M. Minelli, P. Frigeri and S. Franchi. Quantum dot strain engineering of InAs/InGaAs nanostructures. *J. Appl. Phys.*, 101:024313, 2007.

[71] F. Guffarth, R. Heitz, A. Schliwa, O. Stier, N. N. Ledentsov, A. R. Kovsh, V. M. Ustinov, and D. Bimberg. Strain engineering of self-organized InAs quantum dots. *Phys. Rev. B*, 64:085305, 2001.

[72] K. Nishi, H. Saito, S. Sugou, and J. Lee. A narrow photoluminescence linewidth of 21 meV at 1.35 μm from strain-reduced InAs quantum dots covered by $In_{0.2}Ga_{0.8}As$ grown on GaAs substrates. *Appl. Phys. Lett.*, 74:1111, 1999.

[73] J. X. Chen, A. Markus, A. Fiore, U. Oesterle, R. P. Stanley, J. F. Carlin, R. Houdr, M. Ilegems, L. Lazzarini, L. Nasi, M. T. Todaro, E. Piscopiello, R. Cingolani, M. Catalano, J. Katcki, and J. Ratajczak. Tuning InAs/GaAs quantum dot properties under Stranski-Krastanov growth mode for 1.31 μm applications. *J. Apply. Phys.*, 91:6710, 2002.

[74] H. Y. Liu, I. R. Sellers, M. Hopkinson, C. N. Harrison, D. J. Mowbray, and M. S. Skolnick. Engineering carrier confinement potentials in 1.3-μm InAs/-GaAs quantum dots with InAlAs layers: enhancement of the high-temperature photoluminescence intensity. *Appl. Phys. Lett.*, 83:3716, 2003.

[75] F. Guffarth, R. Heitz, A. Schliwa, O. Stier, N. N. Ledentsov, A. R. Kovsh, V. M. Ustinov, and D. Bimberg. Strain engineering of self-organized InAs quantum dots. *Phys. Rev. B*, 64:085305, 2001.

[76] M. V. Maximov, A. F. Tsatsul'nikov, B. V. Volovik, D. S. Sizov, Yu. M. Shernyakov, I. N. Kaiander, A. E. Zhukov, A. R. Kovsh, S. S. Mikhrin, V. M.

Ustinov, Zh. I. Alferov, R. Heitz, V. A. Shchukin, N. N. Ledentsov, D. Bimberg, Yu. G. Musikhin, and W. Neumann. Tuning quantum dot properties by activated phase separation of an InGa(Al)As alloy grown on InAs stressors. *Phys. Rev. B*, 62:16671, 2000.

[77] K. Nishi, M. Yamada, T. Anan, A. Gomyo, and S. Sugou. Long-wavelength lasing from InAs self-assembled quantum dots on (311) B InP. *Appl. Phys. Lett.*, 73:526, 1998.

[78] L. Seravalli, M. Minelli, P. Frigeri, P. Allegri, V. Avanzini, and S. Franchi. The effect of strain on tuning of light emission energy of InAs/InGaAs quantum-dot nanostructures. *Appl. Phys. Lett.*, 82:2341, 2003.

[79] Y.-C. Xin, L. G. Vaughn, L. R. Dawson, A. Stintz, Y. Lin, L. F. Lester, and D. L. Huffaker. Inas quantum-dot GaAs-based lasers grown on AlGaAsSb metamorphic buffers. *J. Appl. Phys.*, 94:2133, 2003.

[80] L.Ya. Karachinsky, T. Kettler, N.Yu. Gordeev, I.I. Novikov, M.V. Maximov, Yu.M. Shernyakov, N.V. Kryzhanovskaya, A.E. Zhukov, E.S. Semenova, A.P. Vasilev, V.M. Ustinov, N.N. Ledentsov, A.R. Kovsh, V.A. Shchukin, S.S. Mikhrin, A. Lochmann, O. Schulz, L. Reissmann, and D. Bimberg. Continuous-wave lasing of single-mode metamorphic quantum dot lasers for the 1.5-μm spectral region. *Semiconductors+*, 39:1415, 2005.

[81] A. Bosacchi, P. Frigeri, S. Franchi, P. Allegri, and V. Avanzini. InAs/GaAs self-assembled quantum dots grown by ALMBE and MBE. *J. Cryst. Growth*, 175/176:771, 1997.

[82] Y. Nakata, K. Mukai, N. Ohtsuka, M. Sugawara, H. Ishikawa, and N. Yokoyama. Molecular beam epitaxial growth of InAs self-assembled quantum dots with light-emission at 1.3 μm. *J. Cryst. Growth*, 208:93, 2000.

[83] M. J. da Silva, A. A. Quivy, S. Martini, T. E. Lamas, E. C. F. da Silva, and J. R. Leite. InAs/GaAs quantum dots optically active at 1.5 μm. *Appl. Phys. Lett.*, 82:2646, 2003.

[84] M. Cahay. *Nanoscale devices and materials and biological Systems: fundamentals and applications: proceedings of the international symposium.* Porc. (Electrochemical Society). Electrochemical Society, 2005.

[85] M. Geddo, G. Guizzetti, M. Patrini, T. Ciabattoni, L. Seravalli, P. Frigeri, and S. Franchi. Metamorphic buffers and optical measurement of residual strain. *Appl. Phys. Lett.*, 87:263120, 2005.

[86] M.A. Majid, D.T.D. Childs, H. Shahid, R. Airey, K. Kennedy, R.A. Hogg, E. Clarke, P. Spencer, and R. Murray. 1.52 μm electroluminescence from GaAs-based quantum dot bilayers. *Electron. Lett.*, 47(1):44–46, 2011.

[87] B. Lamberty, A. Le. Correz, V. Drouoty, H LHaridonz, and S Loualichey. High photoluminescence efficiency of InAs/InP self-assembled quantum dots emitting at 1.5 - 1.6 μm. *Semicond. Sci. Tech.*, 13:143–145, 1998.

[88] N. Carlsson, T. Junno, L. Montelius, M.-E. Pistol, L. Samuelson, and W. Seifert. Growth of self-assembled InAs and $InAs_xP_{1-x}$ dots on InP by metalorganic vapour phase epitaxy. *J. Cryst. Growth.*, 191:347 – 356, 1998.

[89] L. Gonzlez, J. M. Garca, R. Garca, F. Briones, J. Martnez-Pastor, and C. Ballesteros. Influence of buffer-layer surface morphology on the self-organized growth of InAs on InP(0 0 1) nanostructures. *Appl. Phys. Lett.*, 76:1104–1106, 2000.

[90] Y.F. Li, F. Lin, B. Xu, F.Q. Liu, X.L. Ye, D. Ding, and Z.G. Wang. Influence of growth conditions on self-assembled InAs nanostructures grown on (0 0 1)InP substrate by molecular beam epitaxy. *J. Cryst. Growth.*, 223:518 – 522, 2001.

[91] R. Notzel, J. Temmyo, A. Kozen, T. Tamamura, T. Fukui, and H. Hasegawa. Self-organization of strained GaInAs microstructures on InP (3 1 1) substrates grown by metalorganic vapor-phase epitaxy. *Appl. Phys. Lett.*, 66:2525–2527, 1995.

[92] S. Frchengues, N. Bertru, V. Drouot, B. Lambert, S. Robinet, S. Loualiche, D. Lacombe, and A. Ponchet. Wavelength tuning of InAs quantum dots grown on (3 1 1)B InP. *Appl. Phys. Lett.*, 74:3356–3358, 1999.

[93] V. M. Ustinov, E. R. Weber, S. Ruvimov, Z. Liliental-Weber, A. E. Zhukov, A. Yu. Egorov, A. R. Kovsh, A. F. Tsatsulnikov, and P. S. Kopev. Effect of matrix on InAs self-organized quantum dots on InP substrate. *Appl. Phys. Lett.*, 72:362–364, 1998.

[94] J. Brault, M. Gendry, G. Grenet, G. Hollinger, Y. Desieres, and T. Benyattou. Role of buffer surface morphology and alloying effects on the properties of InAs nanostructures grown on InP(001). *Appl. Phys. Lett.*, 73:2932–2934, 1998.

[95] P.J. Poole, K. Kaminska, P. Barrios, Z. Lu, and J. Liu. Growth of InAs/InP-based quantum dots for 1.55 μm laser applications. *J. Cryst. Growth*, 311:1482–1486, 2009.

[96] S. Frechengues, N. Bertru, V. Drouot, B. Lambert, S. Robinet, and S. Loualiche. Wavelength tuning of InAs quantum dots grown on (3 1 1)b InP. *Appl. Phys. Lett.*, 74:3356, 1999.

[97] E. Homeyer, R. Piron, P. Caroff, C. Paranthoen, O. Dehaese, A. Le Corre, and S. Loualiche. Temperature studies on a single InAs/InP QD layer laser emitting at 1.55 μm. *Phys. Status. Solidi. C*, 74:407410, 2006.

[98] G.E. Cirlin, N.K. Polyakov, V.N. Petrov, V.A. Egorov, D.V. Denisov, B.V. Volovik, V.M. Ustinov, Zh.I. Alferov, N.N. Ledentsov, R. Heitz, D. Bimberg,

N.D. Zakharov, P. Werner, and U. Gsele. Heteroepitaxial growth of InAs on Si: the new type of quantum dots. *Mater. Phys. Mech.*, 1:15–19, 2000.

[99] A.Yu. Egorov, A.R. Kovsh, V.M. Ustinov, A.E. Zhukov, M.V. Maksimov, G.E. Cirlin, N.N. Ledentsov, D. Bimberg, P. Werner, and Zh.I. Alferov. Self-organized InAs quantum dots in a silicon matrix. *J. Cryst. Growth*, 201202:1202 – 1204, 1999.

[100] S.M. Chen, M.C. Tang, J. Wu, Q. Jiang, V.G. Dorogan, M. Benamara, Y.I. Mazur, G.J. Salamo, A.J. Seeds, and H. Liu. 1.3 μm InAs/GaAs quantum-dot laser monolithically grown on Si substrates operating over 100 °C. *Electron. Lett.*, 50:1467–1468, 2014.

[101] B. Alen, D. Fuster, Y. Gonzalez, L. Gonzalez, and J. Martinez-Pastor. InAs/InP single quantum wire formation and emission at 1.5 μm. *Appl. Phys. Lett.*, 89:233126, 2006.

[102] D. Fuster, L. Gonzalez, Y. Gonzalez, M. U. Gonzalez, and J. Martnez-Pastor. Size and emission wavelength control of InAs/InP quantum wires. *J. Appl. Phys.*, 98:033502, 2005.

[103] P. J. Carrington, R. J. Young, P. D. Hodgson, A. M. Sanchez, M. Hayne, and A. Krier. Long-wavelength photoluminescence from stacked layers of high-quality type-II GaSb/GaAs quantum rings. *Cryst. Growth Des.*, 13:1226–1230, 2013.

[104] M. Kondow, K. Uomi, A. Niwa, T. Kitatani, Seiji. Watahiki, and Y. Yazawa. GaInNAs: a novel material for long-wavelength-range laser diodes with excellent high-temperature performance. *Jpn. J. Appl. Phys.*, 35:1273, 1996.

[105] J. F. Klem, O. Blum, S. R. Kurtz, I. J. Fritz, and K. D. Choquette. GaAsSb/In-GaAs type-II quantum wells for long-wavelength lasers on GaAs substrates. *J. Vac. Sci. Technol. B*, 18(3):1605–1608, 2000.

[106] N. Tansu, Y. Jeng-Ya, and L.J. Mawst. High-performance 1200-nm InGaAs and 1300-nm InGaAsN quantum-well lasers by metalorganic chemical vapor deposition. *IEEE J. Sel. Top. Quant.*, 9:1220–1227, 2003.

[107] H. Riechert, A. Y. Egorov, D. Livshits, B. Borchert, and S. Illek. InGaAsN/-GaAs heterostructures for long-wavelength light-emitting devices. *Nanotechnology*, 11:201, 2000.

[108] J.-Y. Yeh, L. J. Mawst, A. A. Khandekar, T. F. Kuech, I. Vurgaftman, J. R. Meyer, and N. Tansu. Long wavelength emission of InGaAsN/GaAsSb type II "W" quantum wells. *Appl. Phys. Lett.*, 88:051115, 2006.

[109] P. Blood, E. D. Fletcher, P. J. Hulyer, and P. M. Smowton. Emission wavelength of AlGaAs-GaAs multiple quantum well lasers. *Appl. Phys. Lett.*, 48(17):1111–1113, 1986.

[110] J. Luo and A. Zunger. Geometry of epitaxial GaAs/(Al,Ga)As quantum dots as seen by excitonic spectroscopy. *Phys. Rev. B*, 84:235317, 2011.

[111] Y. C. Chang, A. J. Robson, S. Harrison, Q. D. Zhuang, and M. Hayne. Phonon bottleneck in GaAs/Al$_x$Ga$_{1-x}$As quantum dots. *AIP Adv.*, 5:067141, 2015.

[112] Y. Sidor, B. Partoens, F. M. Peeters, N. Schildermans, M. Hayne, V. V. Moshchalkov, A. Rastelli, and O. G. Schmidt. High-field magnetoexcitons in unstrained GaAs/Al$_x$Ga$_{1-x}$As quantum dots. *Phys. Rev. B*, 73:155334, 2006.

[113] J. Bocquel, A. D. Giddings, T. Mano, T. J. Prosa, D. J. Larson, and P. M. Koenraad. Composition profiling of GaAs/AlGaAs quantum dots grown by droplet epitaxy. *Appl. Phys. Lett.*, 105:153102, 2014.

[114] S. Mitsuru, R. Hong-Wen, N. Kenichi, and M. Yasuaki. Optical properties of InP self-assembled quantum dots studied by imaging and single dot spectroscopy. *Jpn. J. Appl. Phys.*, 41:958, 2002.

[115] T. Tran, A. Muller, C. K. Shih, P. S. Wong, G. Balakrishnan, N. Nunta-wong, J. Tatebayashi, and D. L. Huffaker. Single dot spectroscopy of site-controlled InAs quantum dots nucleated on GaAs nanopyramids. *Appl. Phys. Lett.*, 91:133104, 2007.

[116] E. S. Moskalenko, M. Larsson, W. V. Schoenfeld, P. M. Petroff, and P. O. Holtz. Carrier transport in self-organized InAs/GaAs quantum-dot structures studied by single-dot spectroscopy. *Phys. Rev. B*, 73:155336, 2006.

[117] H.S. Lee, A. Rastelli, M. Benyoucef, F. Ding, T. W. Kim, H. L. Park, and O. G. Schmidt. Microphotoluminescence spectroscopy of single CdTe/ZnTe quantum dots grown on Si(001) substrates. *Nanotechnology*, 20:075705, 2009.

[118] D. V. Lang. Deep-level transient spectroscopy: a new method to characterize traps in semiconductors. *J. Appl. Phys.*, 45:3023, 1974.

[119] T. Nowozin, A. Wiengarten, L. Bonato, D. Bimberg, W. Lin, S. Lin, M. N. Ajour, K. Daqrouq, and A. S. Balamesh. Electronic properties and density of states of self-assembled GaSb/GaAs quantum dots. *J. Nanotechno.*, 2013:302647, 2013.

[120] S. Anand, N. Carlsson, M-E Pistol, L. Samuelson, and W. Seifert. Deep level transient spectroscopy of InP quantum dots. *Appl. Phys. Lett.*, 67:3016, 1995.

[121] T. Nowozin, A. Marent, L. Bonato, A. Schliwa, D. Bimberg, E. P. Smakman, J. K. Garleff, P. M. Koenraad, R. J. Young, and M. Hayne. Linking structural and electronic properties of high-purity self-assembled GaSb/GaAs quantum dots. *Phys. Rev. B*, 86:035305, 2012.

[122] K. Suzuki and K. Kanisawa. Imaging of quantum confinement and electron wave interference. *NTT Rev.*, 2008.

[123] O. Millo, D. Katz, Y. Cao, and U. Banin. Imaging and spectroscopy of artificial-atom states in core/shell nanocrystal quantum dots. *Phys. Rev. Lett.*, 86:5751–5754.

[124] B. Grandidier, Y. M. Niquet, B. Legrand, J. P. Nys, C. Priester, D. Stievenard, J. M. Gerard, and V. Thierry-Mieg. Imaging the wave-function amplitudes in cleaved semiconductor quantum boxes. *Phys. Rev. Lett.*, 85.

[125] J. F. Zheng, X. Liu, N. Newman, E. R. Weber, D. F. Ogletree, and M. Salmeron. Scanning tunneling microscopy studies of Si donors (Si_{Ga}) in GaAs. *Phys. Rev. Lett.*, 72:1490–1493, 1994.

[126] E. E. Vdovin, A. Levin, A. Patan, L. Eaves, P. C. Main, Yu. N. Khanin, Yu. V. Dubrovskii, M. Henini, and G. Hill. Imaging the electron wave function in self-assembled quantum dots. 290:122–124, 2000.

[127] A. Patane, R. J. A. Hill, L. Eaves, P. C. Main, M. Henini, M. L. Zambrano, A. Levin, N. Mori, C. Hamaguchi, Yu. V. Dubrovskii, E. E. Vdovin, D. G. Austing, S. Tarucha, and G. Hill. Probing the quantum states of self-assembled InAs dots by magneto-tunneling spectroscopy. *Phys. Rev. B*, 65:165308, 2002.

[128] T. Nuytten, M. Hayne, M. Henini, and V. V. Moshchalkov. Temperature dependence of the photoluminescence of self-assembled InAs/GaAs quantum dots in pulsed magnetic fields. *Phys. Rev. B*, 77:115348, 2008.

[129] Y. Sidor, B. Partoens, F. M. Peeters, J. Maes, M. Hayne, D. Fuster, Y. Gonzalez, L. Gonzalez, and V. V. Moshchalkov. Exciton confinement in InAs/InP quantum wires and quantum wells in the presence of a magnetic field. *Phys. Rev. B*, 76:195320, 2007.

[130] S. Godefroo, J. Maes, M. Hayne, V. V. Moshchalkov, M. Henini, F. Pulizzi, A. Patan, and L. Eaves. Magneto-photoluminescence study of the influence of

substrate orientation and growth interruption on the electronic properties of InAs/GaAs quantum dots. *J. Appl. Phys.*, 96:2535–2539, 2004.

[131] M.A. Herman, W. Richter, and H. Sitter. *Epitaxy: Physical Priniciples and Technical Implementation.* Springer Series Mate. 2010.

[132] F.C. Frank and J.H. van der Merwe. One-dimensional dislocations. I. static theory. In *P. Roy. Soc. A-Math. Phy.*, pages 205–216. London 198, 1949.

[133] F. Briones, L. Gonzfilez, and A. Ruiz. Atomic layer molecular beam epitaxy (Almbe) of III-V compounds: growth modes and applications. *Appl. Phys. A-Matter.*, 49:729–737, 1989.

[134] S. A. Chambers. Epitaxial growth and properties of thin film oxides. *Surf. Sci. Rep.*, 39:105–180, 2000.

[135] D.J. Mowbray and M. S. Skolnick. New physics and devices based on self-assembled semiconductor quantum dots. *J. Phys. D Appl. Phys*, 38:2059, 2005.

[136] D. Bimberg. Quantum dots: paradigm changes in semiconductor physics. *Semiconductors+*, 33:951–955, 1999.

[137] P. M. J. Mare, J. C. Barbour, J. F. van der Veen, K. L. Kavanagh, C. W. T. Bulle-Lieuwma, and M. P. A. Viegers. Generation of misfit dislocations in semiconductors. *J. Appl. Phys.*, 62:4413–4420, 1987.

[138] L. Seravalli, P. Frigeri, M. Minelli, P. Allegri, V. Avanzini, and S. Franchi. Quantum dot strain engineering for light emission at 1.3, 1.4 and 1.5 μm. *Appl. Phys. Lett.*, 87:063101, 2005.

[139] M. Yahyaoui, K. Sellami, S. Ben-Radhia, K. Boujdaria, M. Chamarro, B. Eble, C. Testelin, and A. Lematre. Effects of strain on the optoelectronic properties of annealed InGaAs/GaAs self-assembled quantum dots. *Semicond. Sci. Tech.*, 29:075013, 2014.

[140] C. Pryor. Eight-band calculations of strained InAs/GaAs quantum dots com-
pared with one-, four-, and six-band approximations. *Phys. Rev. B*, 57:7190–
7195, 1998.

[141] It should be remembered that the distinction between red and blue samples is
somewhat arbitrary and depends on the magnetic field available in the experi-
ment.

[142] J. Maes, M. Hayne, Y. Sidor, B. Partoens, F. M. Peeters, Y. Gonzalez, L. Gon-
zalez, D. Fuster, J. M. Garca, and V. V. Moshchalkov. Electron wave-function
spillover in self-assembled InAs/InP quantum wires. *Phys. Rev. B*, 70:155311,
2004.

[143] R. V. N. Melnik and M Willatzen. Bandstructures of conical quantum dots
with wetting layers. *Nanotechnology*, 15:075013, 1.

[144] J. H. Davies. *The Physics of Low-dimensional Semiconductors*. Cambridge
University Press, 1970.

[145] W. Ya-Fen. Effect of growth interruption on photoluminescence of self-
assembled InAs/GaAs quantum dot heterostructures. *Indian. J. Pure Ap. Phy.*,
50:922–927, 2012.

[146] Z. Y. Xu, Z. D. Lu, X. P. Yang, Z. L. Yuan, B. Z. Zheng, J. Z. Xu, W. K.
Ge, Y. Wang, J. Wang, and L. L. Chang. Carrier relaxation and thermal acti-
vation of localized excitons in self-organized InAs multilayers grown on GaAs
substrates. *Phys. Rev. B*, 54:11528–11531, 1996.